Effect of synthetic method on the structure of pyrochlore- and zirconolite-type oxides

A Thesis submitted to the

College of Graduate and Postdoctoral Studies

In Partial Fulfillment of the Requirements

For the Degree of Master

In the Department of Chemistry

University of Saskatchewan

Saskatoon

By

Sarah McCaugherty

Permission to Use

In presenting this thesis in partial fulfillment of the requirements for a degree of Master from the University of Saskatchewan, I agree that the Libraries of this University may make it freely available for inspection. I further agree that permission for copying of this thesis in any manner, in whole or in part, for scholarly purposes may be granted by the professor or professors who supervised my thesis work or, in their absence, by the Head of the Department or the Dean of the College in which my thesis work was done. It is understood that any copying or publication or use of this thesis or parts thereof for financial gain shall not be allowed without my written permission. It is also understood that due recognition shall be given to me and to the University of Saskatchewan in any scholarly use which may be made of any material in my thesis/dissertation.

Requests for permission to copy or to make other uses of materials in this thesis/dissertation in whole or part should be addressed to:

Head of the Department of Chemistry
University of Saskatchewan
165 Thorvaldson Building, 110 Science Place
Saskatoon, Saskatchewan S7N 5C9
Canada

OR

Dean
College of Graduate and Postdoctoral Studies
University of Saskatchewan
116 Thorvaldson Building, 110 Science Place
Saskatoon, Saskatchewan S7N 5C9
Canada

Abstract

Ceramic materials such as pyrochlore- and zirconolite-type oxides have been studied for several decades due to their applications in catalysis, ferromagnetism, luminescence, ionic conductivity, and radioactive waste sequestration. The studies presented in this thesis investigated the effects of solution-based synthesis methods (coprecipitation and sol-gel) on the long- and short-range structures of pyrochlore- and zirconolite-type oxides annealed at various temperatures and the structural stability of these materials upon irradiation. Powder X-ray diffraction (XRD) was used to confirm the formation of the desired phases at all temperatures studied (pyrochlore: 700 to 1400 °C; zirconolite: 700 to 1400 °C). Changes in the long-range structure of the materials were evaluated by Rietveld refinement of the diffraction patterns. Scanning electron microscopy (SEM) showed an increase in grain size with annealing temperature. X-ray absorption near edge spectroscopy (XANES) was used to probe the local structure of Ti and Zr within the materials. Examination of the Ti K- and Zr K-edge XANES spectra showed no significant change in the structure of the pyrochlore- and zirconolite-type materials annealed at temperatures as low as 800 and 900 °C, respectively. Pellets of pyrochlore- and zirconolite-type materials prepared by the three synthesis methods (ceramic, coprecipitation, and sol-gel) were implanted with high energy Au^- ions to simulate radiation-induced structural damage. Ti K-edge glancing angle XANES showed no change in the radiation resistance of zirconolite prepared by any of the synthesis methods. The pyrochlore-type materials exhibited reduced radiation resistance when the synthesis method was changed from ceramic or coprecipitation to sol-gel. This effect could be due to an increase in the porosity of the material. Therefore, it has been shown that pyrochlore- and zirconolite-type materials can be synthesized at temperatures as low as 800 and 900 °C, respectively, by using a coprecipitation or sol-gel method, due to the atomic scale mixing of reactants which occurs in solution. However, use of these synthesis methods could decrease the ability of the materials to withstand radiation-induced structural damage. The reduction of the annealing temperatures required to form pyrochlore- and zirconolite-type materials results in more cost-efficient processing which is ideal for industrial scaling.

Acknowledgements

I would like to thank my family, friends, and coworkers who have supported me throughout my graduate program. Thanks to the Grosvenor group members; I have enjoyed our academic (and other interesting) discussions. I would especially like to thank Dr. Andrew Grosvenor for being a fantastic supervisor. I have learned a lot from you and I appreciate your patience, advice, and detailed feedback. Thank you to the members of my Advisory Committee for providing me with helpful suggestions and critiques. I would also like to thank Leah Hildebrandt, Bonita Wong, and Erin Wasylow for their valuable administrative support, and Drs. Alex Bartole-Scott and Adrian Clark for being my TA supervisors and helping me to develop my teaching skills.

I want to thank the many people who have helped to collect the data which has been included in this thesis. Thanks to Arthur Situm, Derek Holzscherer, Dr. Jeremy Beam, Dr. Vince Guo, and Dr. Andrew Grosvenor for their help with XANES data collection, and the beamline scientists, Zou Finfrock, Matthew Ward, Tianpin Wu, and George Sterbinsky, at the APS. I would like to thank all others who contributed to this thesis, as follows:

Chapter 2 – Tom Bonli (University of Saskatchewan) for collecting SEM images, and Alicia Koo (University of Saskatchewan) for performing initial method development and proof of concept experiments.

Chapter 3 – Tom Bonli (University of Saskatchewan) for collecting SEM images, and Ifeoma Ebinumoliseh ($ZrSiO_4$), Arthur Situm ($CaTiO_3$), Mike Gaultois (Ba_2TiO_4, $Ba_2TiSi_2O_8$), and James Walker (Gd_2ZrTiO_7) for allowing me to include Ti K- and Zr K-edge XANES spectra from materials prepared during their research (**Figures 3-4(c)** and **3-5(c)**).

Chapter 4 – Tom Bonli (University of Saskatchewan) for collecting SEM images and Jack Hendriks from Interface Science Western (University of Western Ontario) for performing ion implantation experiments.

The funding agencies are thanked for providing the funds required to perform this research. The Natural Sciences and Engineering Research Council (NSERC) of Canada funded this project through a discovery grant awarded to Dr. Andrew Grosvenor. I acknowledge the receipt of support from the CLS Graduate and Post-Doctoral Student Travel Support Program for travel to the

Advanced Photon Source (APS) for XANES collection. The Canadian Foundation for Innovation (CFI) is thanked for providing funds to purchase the PANalytical Empyrean powder X-ray diffractometer that was used in this project. This research used resources of the Advanced Photon Source, an Office of Science User Facility operated for the U.S. Department of Energy (DOE) Office of Science by Argonne National Laboratory and was supported by the U.S. DOE under Contract No. DE-AC02-06CH11357, and the Canadian Light Source and its funding partners.

I personally completed all experimental work (method development, material synthesis, data collection and analysis), with the exceptions outlined above. All chapters were written by me, with editing by Andrew P. Grosvenor.

Contents

List of Tables

List of Figures

List of Abbreviations

α	Alpha Particle
B	Corrected Line Broadening
D	Crystallite Size
d	Distance Between Lattice Planes
I_0	Intensity of Incident X-rays
I_f	Intensity of Fluorescent Photons
I_{ref}	Intensity of X-rays Transmitted Through a Reference Foil
I_t	Intensity of Transmitted X-rays
K	Scherrer Shape Factor
l	Orbital Quantum Number
λ	Wavelength
μ	Absorption Coefficient
n	Principal Quantum Number
t	Sample Thickness
θ	Angle of Incident X-rays
APS	Advanced Photon Source
BM	Bending Magnet
CLS	Canadian Light Source
CN	Coordination Number
EXAFS	Extended X-ray Absorption Fine Structure
FWHM	Full Width at Half Maxima

GA	Glancing Angle
HIP	Hot Isostatic Pressing
HLW	High Level Waste
IAEA	International Atomic Energy Agency
ICP-OES	Inductively Coupled Plasma – Optical Emission Spectroscopy
IEA	International Energy Agency
ILW	Intermediate Level Waste
ISW	Interface Science Western
LINAC	Linear Accelerator
LLW	Low Level Waste
NNN	Next Nearest Neighbour
RE	Rare-Earth
RF	Radio Frequency
SEM	Scanning Electron Microscopy
SRIM	Stopping Range of Ions in Matter
SYNROC	Synthetic Rock
TEY	Total Electron Yield
VESTA	Visualization for Electronic and Structural Analysis
XANES	X-ray Absorption Near-Edge Spectroscopy
XAS	X-ray Absorption Spectroscopy
XRD	X-ray Diffraction

Chapter 1

Introduction

1.1 Nuclear power and radioactive waste

Nuclear power is a major source of electricity worldwide.[1,2] As of 2017, there were 446 operable reactors which were responsible for generating 11.5% of the world's electricity.[2] With 60 reactors under construction, 168 ordered, and 345 proposed, the global nuclear industry is expanding.[2] Nuclear power is the second largest source of electricity in Canada and contributes more than 60,000 jobs and $6 billion to the economy per year.[2] Canada is also the second largest uranium producer in the world (after Kazakhstan), with the world's highest-grade uranium deposits located in Saskatchewan.[2]

In 2008, the International Energy Agency (IEA) projected that world energy requirements will nearly double by 2030.[3] Various "green" energy sources such as wind, solar, and nuclear have been proposed to meet these energy demands while combatting the prospect of climate change by producing little to no CO_2 emissions.[1,4] These energy sources can result in additional health benefits to communities as there are no SO_x, NO_x, or particulate emissions from these processes, which are responsible for smog in large urban areas.[3] Intermittent sources of energy, like solar and wind energy, would rely on backup sources approximately 80% of the time, whereas nuclear power is available on a consistent basis.[2] Reliance on nuclear power provides energy security as the fuel is available from many politically stable countries, and the high energy density of uranium allows for easier storage of large energy reserves when compared to fossil fuels.[3] The major disadvantage of nuclear power is the generation of nuclear (radioactive) waste.

Radioactive waste in Canada is generated from: uranium mining, milling, and refining; nuclear fuel fabrication; nuclear reactors; nuclear research; and radioisotope manufacturing and use.[2,5] This waste is categorized depending on the level of radioactivity detected and/or the heat

emitted by the material.[6] Low-level radioactive waste (LLW) are those materials that are used in the workplace surrounding the use of radioactive materials (e.g. gloves, cloths, protective clothing), and this category accounts for about 98% of all Canadian radioactive waste.[5,6] Intermediate-level radioactive waste (ILW) has had more direct contact with radioactive materials, such as ion-exchange resins and reactor components.[6,7] High-level radioactive waste (HLW) is defined as spent fuel and other materials emitting >2 kW/m^3 of heat.[6,8] **Table 1-1** shows the inventory of radioactive waste in Canada as of 2015, and the projected quantities of waste to 2050.[2,5] Additionally, approximately 300,000 L of liquid HLW is currently in storage from the production of medical isotopes and Cold War-era experiments.[5]

Table 1-1 Inventory of LLW, ILW, and HLW nuclear waste produced in Canada to the end of 2013 and projected to the end of 2050.[5]

Waste Category	**Waste Inventory to the End of 2013 (m^3)**	**Projected Waste Inventory to the End of 2050 (m^3)**
High-Level Waste	10,021	20,000
Intermediate-Level Waste	34,770	67,000
Low-Level Waste	2,353,000	2,594,000

There are currently three disposal routes proposed for the various types of radioactive wastes: landfill, near-surface, and deep geological disposal.[6] The landfill type of disposal has been implemented in several countries (e.g. Czech Republic, Finland, France, Japan, Spain, Sweden, the United Kingdom, and the United States) for the storage of LLW at or above ground level.[6] Near-surface storage occurs at depths of a few tens to hundreds of metres and has been implemented in Finland and Sweden for LLW and short-lived ILW.[6,9] Most countries with HLW have investigated storing this waste in deep geological repositories several hundred to thousands of metres below ground.[6,7,9,10] The plan for the long-term care of Canada's nuclear waste is to isolate the waste in a deep geological repository.[6,10] Sites for this repository are currently being evaluated.[6,10]

1.2 Nuclear wasteforms

A wasteform is defined as "waste in its physical and chemical form after treatment and/or conditioning (resulting in a solid product) prior to packaging".[11,12] The ultimate purpose of radioactive waste management is to immobilize radioactive elements in wasteforms to prevent the release of those radionuclides into the environment.[13–19] Groundwater leaching has been identified as the most likely mechanism by which release of radionuclides may occur.[4,17,20–22] Therefore, the most important requirement for a wasteform is to be chemically durable.[11,12,14,16–18,20–25] Additionally, an ideal wasteform should be resistant to damage caused by radioactive decay processes, incorporate a wide range of elements with high loading, and be easy to fabricate with reasonable synthesis conditions.[11,13,15,18,20,23–26] Several types of wasteforms have been studied to date including glasses, ceramics, and glass-ceramic composites.

1.2.1 Glass wasteforms

Vitrification of HLW is currently the most common route of radioactive waste immobilization in many countries around the world, such as France, Japan, Russia, the United Kingdom, and the United States.[3,6] This is due to several reasons, including the simple processing to form glass wasteforms and the wide range of elements that can be incorporated into a glass.[18,20,23,27–32] The most commonly used compositions of nuclear waste glasses are borosilicate and phosphate glasses, but the exact composition of the glass is adjusted for each waste stream to prevent phase separation and crystallization.[12,18,20,28,30,31,33–35] The waste loading in these wasteforms ranges between 25 and 35 wt%, however, most actinides are incorporated at much lower loadings (3 to 10 wt%).[18,30,32] Waste elements can be contained in the glass by chemical incorporation into the glass structure as network formers or modifiers, or by physical encapsulation.[20,28] Glass wasteforms generally show lower thermal stability and chemical durability than other types of wasteforms, such as ceramics, which has led to an interest in developing more sophisticated wasteforms.[25,28,30,36,37]

1.2.2 Ceramic wasteforms

Ceramic oxide materials have attracted a substantial amount of interest as nuclear wasteforms, with many different compositions being proposed, including brannerite- ($Ce_2Ti_2O_6$), hollandite- ($BaAl_2Ti_6O_{16}$), perovskite- (ABO_3), zircon- ($ZrSiO_4$), pyrochlore- ($A_2B_2O_7$), and zirconolite-type

($CaZrTi_2O_7$) oxides.[13,15,18,25,27,28,33,38–40] This is because of the existence of naturally occurring analogues which have been shown to contain radionuclides and withstand radiation damage over geological timescales.[13,18,23,27–29,37–39,41–44] Ceramics can demonstrate superior physical properties to glasses such as increased loading of waste elements, higher thermal stability, and higher chemical durability.[25,27,28,34–37,39,45,46] In ceramic materials, radionuclides occupy specific sites within a crystal structure.[12,15,18,23,27,28,35,37,40,47,48] This contributes to the improvement in physical properties relative to glass wasteforms; however, only specific elements (depending on the ionic radius and oxidation state) can substitute into these sites.[28,37] This problem can be solved by combining different crystalline materials into multi-phase ceramic wasteforms.[13,15,25,45,49] The most commonly known multi-phase ceramic for nuclear waste sequestration is SYNROC ("synthetic rock") which is a mixture of hollandite, perovskite, rutile (TiO_2), and zirconolite.[13,18,25–27,37–39,45,49,50] Multi-phase ceramics may be implemented in the future for nuclear waste sequestration, but before that can occur, the important properties of each ceramic phase as pertains to waste sequestration must be fully understood. The two ceramic phases that have been investigated in this thesis work are pyrochlore- and zirconolite-type oxides. These materials show significantly improved resistance to leaching, as shown in **Figure 1-1**, as well as other properties that are beneficial to the implementation of these materials as nuclear wasteforms.[13,18,38,39,41,50]

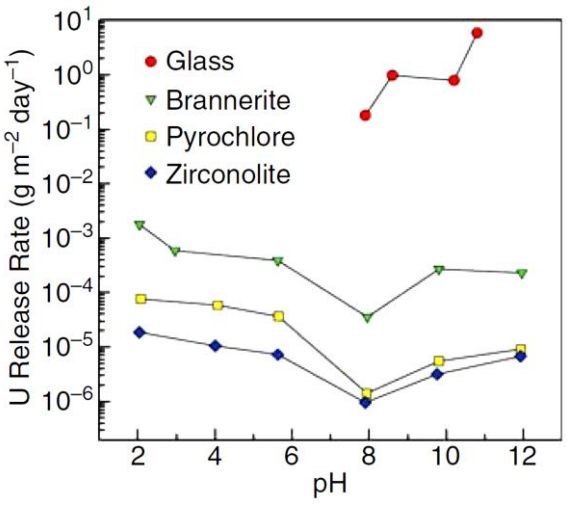

Figure 1-1 Comparison of the U leach rate from glass, brannerite, pyrochlore, and zirconolite materials, demonstrating the increased chemical durability of ceramic materials relative to glass. Figure reproduced with permission from Cambridge University Press.[28]

1.2.2.1 Pyrochlore-type oxides

Pyrochlore-type oxides are a family of oxides with the general formula $A_2B_2O_7$.[1,13,14,22,33,46,50–67] The structure is cubic with the space group $Fd\bar{3}m$, where the A-site is 8-coordinate in a distorted cubic environment and the B-site is 6-coordinate in a distorted octahedral environment, as shown in **Figure 1-2(a)**.[1,13,14,19,22,33,38,39,46,50,53,56–60,62–64,66–70] The pyrochlore structure is related to the fluorite structure, MO_2, where $1/8^{th}$ of the fluorite anion sites (the 8a crystallographic site) are unoccupied, which results in two distinct cation coordination environments (A and B), rather than a single cation site (M) within the fluorite structure as shown in **Figure 1-2(b)**.[1,13,19,22,33,46,52–54,58–60,63,67,68,70,71] The formation of the pyrochlore structure, rather than the disordered defect fluorite structure, depends on the radius ratio of the cations.[22,33,53,54,56,60,63,64,66–68,70,72,73] If the ratio of the ionic radius of the A-site cation (r_A) to the radius of the B-site cation (r_B) is between 1.46 and 1.78, the pyrochlore structure is formed. However, if the ratio r_A/r_B is less than 1.46, then the disordered fluorite structure is formed.[13,22,33,53,54,56,60,63,64,66–68,70,73] This is because as the ionic radii of the two cations become more similar, the amount of disorder in the structure increases.[13,22,60,63,67,68,73] More than 500 compositions are known to form the pyrochlore structure due to the structural flexibility of this type of ceramic.[1,13,22,33,39,40,54,63,68] The A- and B-sites can incorporate combinations of elements with 3+ and 4+ oxidation states, 2+ and 5+ oxidation states, as well as mixtures of the two.[1,13,22,26,38,50,54,63–65] The compositions with A^{3+} and B^{4+} cations are most relevant to nuclear waste applications due to their ability to incorporate trivalent rare-earth elements and tri- and tetravalent actinides.[22,54,63,74] The titanate ($A_2Ti_2O_7$) and zirconate ($A_2Zr_2O_7$) variants of the pyrochlore structure are of particular interest as nuclear wasteforms due to their resistance to radiation damage and chemical durability relative to borosilicate glass.[31,33,39,46,47,52–54,59,67–70,73,74] Natural pyrochlore analogues can contain up to 30 wt% UO_2, 9 wt% ThO_2, and 16 wt% RE_2O_3 (rare-earth oxide) while retaining their structural integrity over geological timescales.[22,38,75]

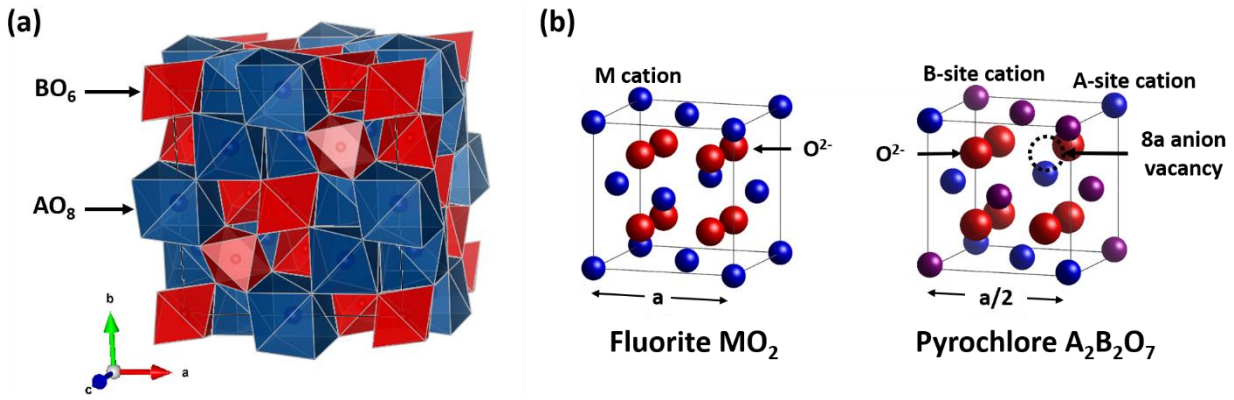

Figure 1-2 (a) The pyrochlore-type structure. The 8-coordinate A-site is shown in blue, and the 6-coordinate B-site is shown in red. The O atoms occupy tetrahedral interstitial sites. The structure was generated using the VESTA software program. **(b)** A comparison of the fluorite and pyrochlore-type structures. Figure adapted from Ewing, R. C.; Weber, W. J.; Lian, J. Nuclear Waste Disposal-Pyrochlore ($A_2B_2O_7$): Nuclear Waste Form for the Immobilization of Plutonium and "Minor" Actinides. *J. Appl. Phys.* **2004**, *95*, 5949–5971.[22]

1.2.2.2 Zirconolite-type oxides

Zirconolite-type oxides are related to the pyrochlore structure by compression along the [111] direction, resulting in the lower symmetry monoclinic space group $C2/c$.[19,38,49] The ideal mineral formula of zirconolite is $CaZrTi_2O_7$.[25,32,38,39,41,49,50,76] The structure consists of two different cation layers, one composed of 8-coordinate Ca^{2+} and 7-coordinate Zr^{4+} polyhedra and the other of corner sharing 6-coordinate and 5-coordinate Ti^{4+} polyhedra in a 2:1 ratio, shown in **Figure 1-3**.[19,25,32,40,41,49] Several zirconolite polytypes exist (e.g. 2M, 3T, 3O, 4M, and 6T) that vary according to the layer stacking pattern.[19,25,39,40,49,50] The 2M polytype forms for compositions of $CaZr_xTi_{3-x}O_7$ where x ranges from 0.7 to 1.3.[19,49] Zirconolite-type oxides have been investigated for nuclear waste sequestration applications for several decades. Actinides and rare-earth elements may substitute into both the Ca and Zr sites, with charge balance maintained by substitution of Mg, Al, Fe, Nb, Ta, or W for Ti.[18,25,38–40,48–50,75,76] Zirconolite is generally more resistant to radiation-induced damage and is more chemically durable than pyrochlore-type materials.[33,38,75]

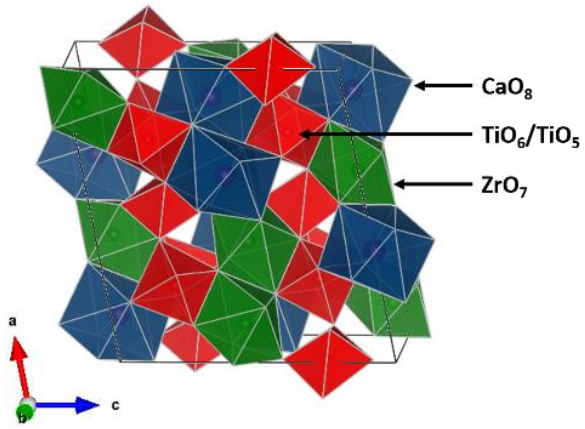

Figure 1-3 The 2M zirconolite-type structure ($CaZrTi_2O_7$). The 8-coordinate Ca-site is shown in blue. The 7-coordinate Zr-site is shown in green. The 6- and 5- coordinate Ti-sites are shown in red. The structure was generated using the VESTA software program.

1.2.3 Glass-ceramic composite wasteforms

Glass-ceramic wasteforms combine the benefits of both glasses and ceramics into one wasteform.[14,16,28,30–32,36,42,77] Both the glass and ceramic phases can incorporate actinides and fission products, which makes these wasteforms ideal for waste streams that are difficult to process.[14,17,18,20,35] For example, the immobilization of ^{137}Cs and ^{90}Sr in Mo-rich waste streams is difficult as these elements tend to be present in concentrations higher than would be soluble in borosilicate glass and can cause the melt to phase separate.[17,23,42] By adding additional alkaline earth metals, alkaline-earth molybdates will crystallize within the glass to form one continuous wasteform.[17,23,42] There is also the potential benefit of the glass phase acting as a secondary barrier for the leaching of radionuclides from the ceramic phase upon radiation damage.[14,17,27,32,35,77] Research into glass-ceramic composites is ongoing due to the need to understand the crystallization mechanisms within the melt and the effect of the glass-ceramic interface on the properties of the composites which are pertinent to radioactive waste sequestration.[14,17,30,32,35,78]

1.3 Synthesis methods

A wide variety of synthesis methods can be used to prepare ceramic materials. The most commonly used method is the ceramic method, but interest in alternative methods to prepare materials with desirable physical properties is growing.[79–82] The work presented in this thesis utilized three synthesis methods (ceramic, coprecipitation, and sol-gel) to prepare pyrochlore- and zirconolite-type oxides.

1.3.1 Ceramic

The ceramic (high-temperature solid-state) method is the most widely used method for the synthesis of bulk metal oxides.[46,48,64,77,79,82] This technique involves the direct reaction of metal oxide powders which are mechanically mixed to form the product. The powder mixture tends to be well mixed at the particle (μm) scale, but is inhomogeneous at the atomic scale.[46,49,59,80,82–85] Because of this, high temperatures are usually required to ensure that diffusing ions have sufficient thermal energy to migrate through the material.[59,64,79,80,82,83,85,86] Intermediate grinding stages are also frequently required to break up reactant/product interfaces and form new reactant/reactant interfaces to allow for faster reaction times.[49,59,64,77,80,82,83,85,86] A range of solution-based synthesis methods have been investigated to mitigate the limitations of solid-state diffusion, such as coprecipitation, sol-gel, and other methods.[45,46,48,59,64,74,77,79–81,83–88] A chemically homogeneous precursor can be obtained by mixing reactants in a solution phase, which should result in lower annealing temperatures and shorter annealing times to form ternary or quaternary oxides.[22,46,64,74,84–88]

1.3.2 Coprecipitation

The coprecipitation method involves the dissolution of metal-containing reagents followed by the precipitation of all metal ions, typically as hydroxides or oxalates.[46,80,81] A homogeneous mixture of powders is obtained if all species precipitate at the same pH.[46,81] Some materials cannot be easily synthesized by this method. Alkali or alkaline earth metals tend to be highly soluble, even at high pH, and some transition metals are known to form soluble hydroxide complexes.[45,80] Thus, pH control is very important when using coprecipitation methods.[46,81] Complexing agents, such as oxalic acid, can sometimes be used to avoid these solubility issues.

1.3.3 Sol-gel

Sol-gel can be considered as a broad classification of solution-based synthesis methods, which result in the formation of a semi-solid gel.[79,85] Traditionally, sol-gel methods are defined as the transformation of molecular precursors from a solution to a sol (a colloidal suspension of particles < 1 μm in size) to a gel (a three-dimensional solid network containing a liquid).[79,82,85] The gel can then be dried to obtain the final solid material, either an aerogel or a xerogel depending on whether the structure of the network is retained.[79,82,85] Gels can be classified into five different types: colloidal, metal-oxane polymers, metal complexes, *in situ* polymerizable complexes (Pechini method), and coordinating and crosslinking polymers.[85] The structures of these gels are shown in **Figure 1-4**.

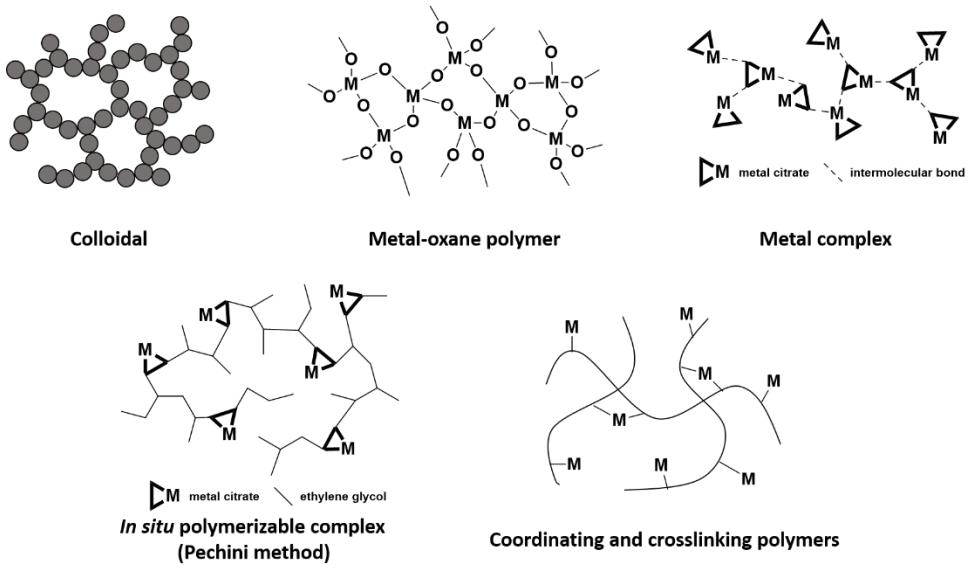

Figure 1-4 The five different types of gels produced from sol-gel synthesis. Figure adapted from Danks, A. E.; Hall, S. R.; Schnepp, Z. The Evolution of 'Sol–gel' Chemistry as a Technique for Materials Synthesis. *Mater. Horiz.* **2016**, *3*, 91–112.[85]

Colloidal gels are formed from particles of metal oxides or hydroxides connected by intermolecular forces.[82,85] Metal-oxane polymer gels are formed from the hydrolysis and condensation of metal alkoxides to form inorganic polymers composed of covalently bonded metals and oxygen.[79,85,89] During hydrolysis of metal alkoxides, the alkoxide groups are replaced by a water molecule followed by deprotonation of the water group to form a metal hydroxide

species (**Figure 1-5(a)**) and an alcohol.[79,82,85] Condensation occurs between a metal hydroxide and either a second metal hydroxide (oxolation) or a metal alkoxide (alkoxolation) to form a metal-oxygen-metal bond and either water or an alcohol (**Figure 1-5(bc)**).[79,82,85] Gels can also form in concentrated metal complex solutions by intermolecular attractions.[85]

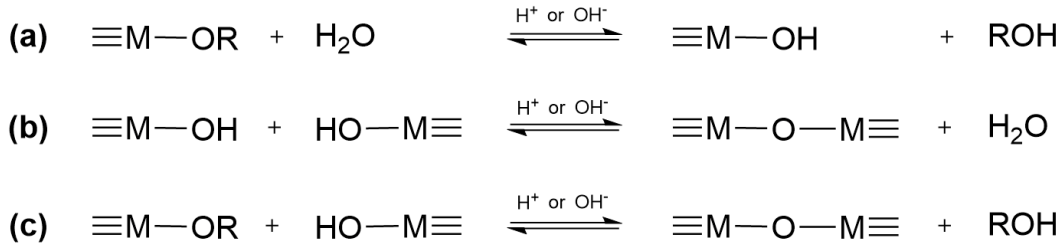

Figure 1-5 (a) The general reaction for hydrolysis of a metal alkoxide. **(b)** A general oxolation reaction. **(c)** A general alkoxolation reaction.

The Pechini method involves polyesterification between a polyhydroxy alcohol (e.g. ethylene glycol) and a carboxylic acid metal complex (e.g. metal-citrate) upon heating.[22,82,85] A gelatinous polymer is formed in situ around complexed metal ions.[82,85] The gel can then be heated to induce pyrolysis of the organic polymer, leaving a homogeneous metal oxide powder.[22,82,85] Lastly, a polymer that directly bonds to a metal can be used to form a gel, rather than forming from the polymerization of a chelating ligand bonded to a metal.[85]

Various analysis techniques are required to understand the structure of ceramic materials. The techniques used in this thesis include powder X-ray diffraction, X-ray absorption spectroscopy, and ion implantation. A brief description of each of these techniques and related analyses are provided below.

1.4 Powder X-ray diffraction

Powder X-ray diffraction (XRD) is used to identify crystalline components of a material and is one of the most powerful analysis methods in materials science.[82,90,91] A crystal can be thought of as a series of lattice planes which diffract X-rays.[82,90] If the diffracted X-rays interfere constructively according to Bragg's law,

$$2d \sin\theta = n\lambda \quad (1.1)$$

where d is the spacing between crystal lattice planes, θ is the diffraction angle, n is a positive integer, and λ is the wavelength of the incident X-rays, then a diffraction peak is observed at a specific angle.[82,90,91] Particles within a powder diffraction sample should be randomly oriented to ensure that a fraction of the crystallites is oriented at the proper angle.[82,90,91] Preferred orientation exists when the sample is not randomly oriented, which can affect the relative intensities of the diffraction peaks.[82,90,91] In addition to simply identifying crystalline components of a material, powder diffraction patterns can also be used to refine unit cell parameters of a known crystal structure and to estimate the average crystallite size of the crystalline components of a material.[82,90]

1.4.1 Rietveld refinement

Rietveld refinement is a technique that uses a least-squares minimization approach to model powder diffraction patterns.[90–92] By varying multiple structural and instrumental parameters, a calculated pattern is generated to fit an experimental pattern.[90,91] The difference between the observed and calculated intensities of every experimental data point is minimized according to Equation 1.2, where Y_o is the observed intensity of a data point, Y_c is the calculated intensity, and w is a weight factor for each point based on the uncertainty in the measurement.[90–93] This is accomplished by fitting the overall pattern with mathematical models describing peak position, intensity, and shape.[90]

$$M = \sum w(Y_o - Y_c)^2 \quad (1.2)$$

These three components are determined by the crystal structure of the material, various physical properties of the sample, and instrumental parameters.[90] Peak position is affected by the unit cell parameters of the crystal structure, the type of X-ray source used, and the alignment of the diffractometer.[90] Peak intensity is affected by the atomic positions within the crystal structure, preferred orientation of the sample, and absorption of the incident X-rays by the sample.[90] Peak shape is affected by the crystallinity of the material, the presence of disorder or defects, grain size, stress, strain, and the spectral purity of the X-rays.[90]

When performing a refinement, the scale factor and instrument displacement (zero shift) parameter must be refined first after determination of a suitable background for the experimental pattern.[90,93] The scale factor linearly scales the calculated pattern to be in the correct intensity range of the experimental pattern.[90] The zero shift parameter accounts for the improper setting of zero angles for one or more diffractometer axes (X-ray source or detector).[90] Unit cell parameters (*a*, *b*, *c*, α, β, γ) and the general positional parameters for each occupied crystallographic site (*x*, *y*, *z*) are refined for the crystal structure.[93] Either an isotropic or anisotropic atomic displacement parameter can be refined for each crystallographic site, or an overall atomic displacement parameter can be refined (B_{OVL}).[90,93] These factors mainly account for the thermal vibrations of atoms within a crystal lattice, as well as lesser factors such as deformation of electron density around the atom.[82,90] A preferred orientation factor may also be refined if it is known or suspected that the sample is not randomly oriented, as is the case for highly anisotropic materials, e.g. platelet- or needle-like crystallites.[90] All these parameters affect either the peak position or intensity.[90] The peak shape must also be refined using a peak shape function. The refinements that were performed in this thesis were conducted by refining variables in the following order: scale factor, zero shift, unit cell parameters, atomic positional parameters, peak shape variables, and atomic displacement parameter.

In this thesis, the XRD patterns were modeled with the Pseudo-Voigt peak shape function, shown in Equation 1.3.[90,91] The Pseudo-Voigt function is a linear combination of Gaussian and Lorentzian peak shape functions.[90,91]

$$y(x) = \eta \frac{C_G^{1/2}}{\sqrt{\pi} H} \exp(-C_G x^2) + (1 - \eta) \frac{C_L^{1/2}}{\pi H} (1 + C_L x^2)^{-1} \tag{1.3}$$

In this equation, *H* is the full width at half maxima (FWHM) of a peak, which is described by the Caglioti equation,

$$H = \sqrt{U \tan^2 \theta + V \tan \theta + W} \tag{1.4}$$

where *U*, *V*, and *W* are free variables, referred to as Caglioti parameters.[90,91,93] The Pseudo-Voigt function mixing parameter, η, describes the fractional contribution of the Gaussian function to the Pseudo-Voigt function, given by Equation 1.5,

$$\eta = \eta_0 + \eta_1 2\theta + \eta_2 2\theta^2; \quad 0 \leq \eta \leq 1 \tag{1.5}$$

where η_0, η_1, and η_2 are free variables. $C_G^{1/2}/\sqrt{\pi}H$ and $C_L^{1/2}/\pi H$ are normalization factors for the Gauss and Lorentz functions respectively, with $C_G = 4\ln 2$ and $C_L = 4$.[90] The variable *x* represents the Bragg angle of the ith point (θ_i) with its origin in the position of the kth peak (θ_k) divided by the FWHM of the kth peak (H_k):[90]

$$x = (2\theta_i - 2\theta_k)/H_k \tag{1.6}$$

The calculated pattern can be compared to the experimental pattern by various residual functions, also referred to as R-factors (Equations 1.7-1.9), and the goodness of fit (Equation 1.10).[90,93] The profile R-factor, R_p, is a simple summation of the difference in observed and calculated intensities, divided by the sum of the observed intensities.[82,90]

$$R_p = \frac{\sum|Y_o - Y_c|}{\sum Y_o} \tag{1.7}$$

The weighted profile R-factor, *Rwp*, considers the statistical weightings of each data point.[90,92,93]

$$R_{wp} = \sqrt{\frac{M}{\sum wY_o^2}} \tag{1.8}$$

The expected R-factor, R_{exp}, is mathematically the best possible R_{wp} value that could be obtained from the refinement, where *N* is the number of data points collected and *P* is the number of parameters refined (degrees of freedom).[90,92,93]

$$R_{exp} = \sqrt{\frac{N-P}{M}} \tag{1.9}$$

The goodness of fit, χ^2, compares the weighted profile R-factor to the best possible R-factor for the experimental pattern.[90,92,93] This value should always be greater than 1, and lower values of χ^2 generally indicate a better fit.[90,92,93] Very large values for goodness of fit can indicate that the model used in the refinement is incorrect.

$$\chi^2 = \left(\frac{R_{wp}}{R_{exp}}\right)^2 \tag{1.10}$$

R-factors and goodness of fit alone cannot be used to determine whether a refinement is "good".[90–93] One reason for this is that these factors contain contributions from the background

which can artificially lower these R-factors when the background is high.[90,92] This can make the refinement appear to be good when it may not be. Additionally, even small differences in peak shape or position can dramatically increase the difference between R_{exp} and R_{wp} when experimental patterns with very high counts are used due to increased statistical precision in the measurement.[90,92] The quality of a refinement is therefore judged based on the values of the R-factors and goodness of fit, the chemical plausibility of the refined values, and the visual fit of the calculated pattern to the experimental pattern.[90–93]

1.4.2 Crystallite size

In a powder diffraction experiment, radiation diffracted from a sample of small crystals results in broadening of the diffracted beam, and the subsequent broadening of peaks in the diffraction pattern. Powder X-ray diffraction patterns can be used to estimate the crystallite size of a material using the Scherrer Equation,

$$D = \frac{\mathrm{K}\lambda}{B\cos\theta} \tag{1.11}$$

where D is the average crystallite size, K is the shape factor, λ is the X-ray wavelength, B is the corrected line broadening at the full width at half maximum (FWHM), and θ is the Bragg angle.[91,94–96] The shape factor is a unitless scale factor that is defined based on the known or assumed shape of the crystallites.[91,95,96] The most commonly used value is K = 0.9 for spherical crystallites, but these values can range from 0.6-2.2 for non-spherical crystallites. The width of a diffraction peak depends on both crystallite size and the resolution of the diffractometer that is used.[95] Thus, the FWHM must be corrected to account for the instrumental contribution.[91] This is typically done by collecting a diffraction pattern from a highly crystalline reference material, such as LaB_6 or Si, and subtracting the width of one of the peaks from this diffraction pattern from the FWHM of the sample diffraction pattern.[91] This gives the corrected line broadening, B. While the Scherrer equation gives a reasonable estimate for the crystallite size of the material, it is limited by the use of many assumptions and disregard for other peak broadening factors, such as strain within the sample.[91,95] The value that is calculated by the Scherrer equation is the average crystallite size of a polycrystalline material, and should not be mistaken for grain size, except in the case of single crystals.[91,95]

1.5 X-ray absorption spectroscopy

In contrast to X-ray diffraction, which provides information on the long-range structure of a crystalline material, X-ray absorption spectroscopy (XAS) provides information on the average local structure of atoms within a material.[13,14,60,66,68,97–105] The spectra are element specific, and sensitive to the oxidation state and chemical environment of the absorbing element.[13,14,60,66,68,82,97–99,101,102,104,105] This technique can be applied to most elements and to many different sample types, such as amorphous solids, crystalline solids, solutions, or polymers.[82,97–99,101,106]

In an XAS experiment, a core electron is excited to an unoccupied conduction state (or out of the atom) by the absorption of an X-ray.[13,97,100,107] The energy at which the core electron is excited is referred to as the absorption edge and is identified by the principal quantum number of the electron being excited (e.g., n = 1 is the K-edge, n = 2 is the L-edge, etc.).[82,100,107] The energy of the absorption edge is affected by the coordination environment and the oxidation state of the absorbing atom. The excitation of the core electron generally follows the conservation of angular momentum, $\Delta l = \pm 1$, resulting in prominent dipolar electronic transitions (main edge features).[13,66,100,107] However, weak quadrupolar transitions, $\Delta l = \pm 2$, can be observed (pre-edge features).[13,66,100,105–107] The intensity of these features depend on the overlap of the orbitals involved in the electronic transition.[13,66,100,102,103,105,106,108] These electronic transitions are shown schematically in **Figure 1-6(a)** and graphically in **Figure 1-6(b)**.

A core (electron) hole is created by the absorption of an X-ray.[97,100] The two main mechanisms by which the excited state can decay are X-ray fluorescence and the emission of an Auger electron.[97,100] During fluorescence, a higher energy core electron relaxes into the core hole emitting an X-ray.[97,100] These fluorescence energies are well known for each element.[97] An Auger electron is emitted if the relaxation of an electron to fill the core hole transfers its energy to another electron which is then ejected from the material.[97,100] The measurement of Auger electrons is limited by the mean free path of the emitted electrons, making this measurement inherently surface sensitive.[66,100] Both fluorescence and electron emission can be used to measure X-ray absorption spectra.[66,100]

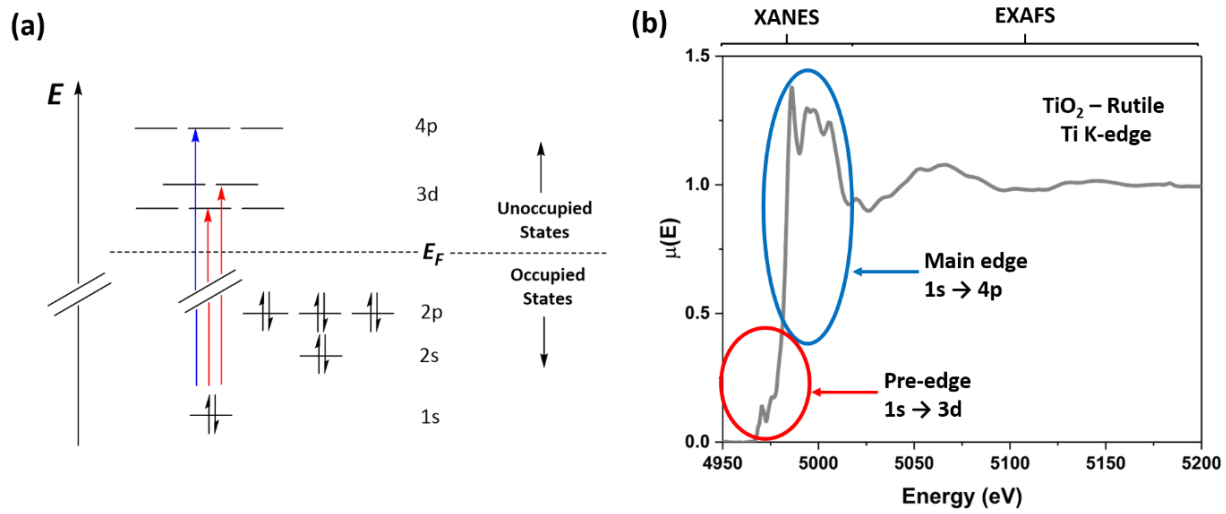

Figure 1-6 (a) Schematic of a K-edge electronic excitation by X-ray absorption. Blue arrow shows the $\Delta l = \pm 1$ transition. Red arrows show the $\Delta l = \pm 2$ transitions. **(b)** Rutile Ti K-edge XAS spectrum.

X-ray absorption spectroscopy is composed of two parts: X-ray absorption near edge spectroscopy (XANES; also referred to as X-ray absorption near edge structure) and extended X-ray absorption fine structure (EXAFS).[60,68,82,97,100,101,107] In XANES, a core electron is excited to an unoccupied conduction state, whereas in EXAFS the electron is excited out of the absorbing atom and is scattered by neighbouring atoms.[100] While both XANES and EXAFS regions were collected in this thesis, only analysis of the XANES regions will be presented. XANES is highly sensitive to the oxidation state and coordination environment (e.g. coordination number; CN) of the absorbing atom.[14,60,68,97,100,103]

1.5.1 Synchrotron radiation

X-ray absorption spectroscopy requires a tunable X-ray source with high intensity to obtain high-quality data.[82,97,101,107,109,110] This is accomplished by the use of a synchrotron light source, such as the Canadian Light Source (CLS), Advanced Photon Source (APS), and many other facilities around the world. Within a synchrotron source, electrons are accelerated to speeds nearing the speed of light.[82,91,101,109,110] The electron beam is directed in a circular path by use of magnetic fields, which results in the loss of kinetic energy by emission of radiation tangential to the path of the electrons.[82,91,101,109] The radiation that is emitted ranges from infrared to hard X-rays and

beamlines are built to harness a specific energy region within this range.[82,91,101] The main advantages of using a synchrotron source rather than a conventional laboratory radiation source are the significantly higher flux (photons/second/mrad/unit bandwidth) and brightness (photons/second/unit source area/unit bandwidth).[82,101,109]

Figure 1-7 shows a general schematic of a synchrotron facility. Electrons are generated by an electron gun via thermionic emission from a metal filament, usually tungsten.[109] These electrons are accelerated within a linear accelerator and the booster ring to increase the energy of the electrons to MeV and GeV, respectively[109]. Once the electrons reach this high energy they are then injected into the storage ring.[109] The storage ring is comprised of a series of straight and curved sections with dipolar, quadrupolar, and sextapolar magnets at various locations around the ring to maintain the path of the electrons and the beam size.[82,101,109] Insertion devices (e.g. wigglers or undulators) consist of an array of magnets with alternating polarity which causes the electron to follow a sinusoidal path, increasing the brightness of the radiation.[82,91,101,109] Experiments can then be performed in end stations which are connected to the storage ring by a beamline.[109]

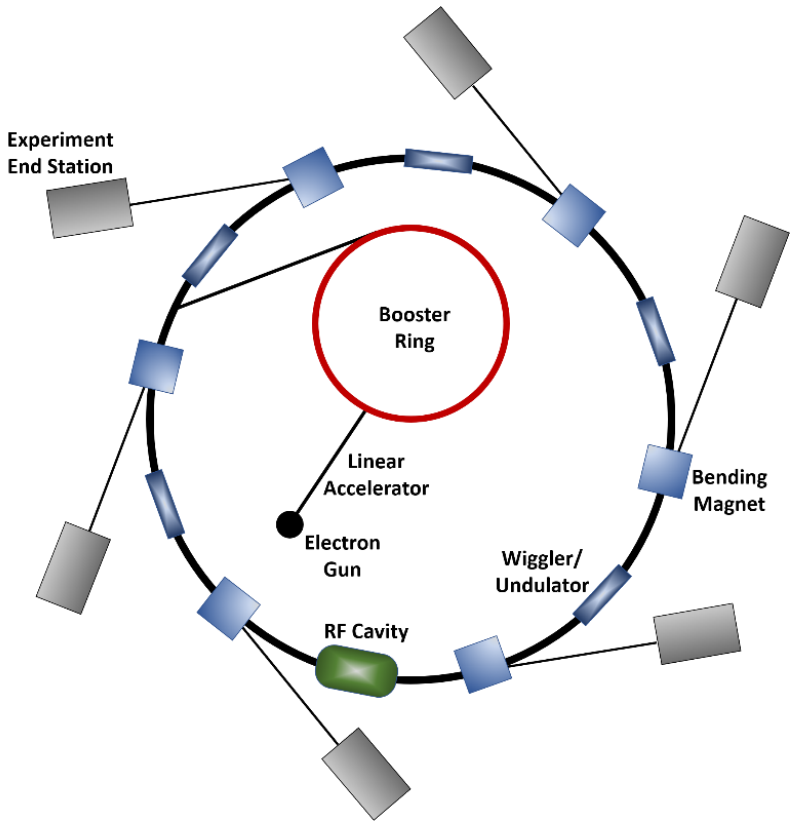

Figure 1-7 Schematic diagram of a synchrotron radiation source.

1.5.2 Beamline setup

A synchrotron beamline is composed of three parts: the front-end, beamline optics, and experimental end station.[109] The front-end connects the storage ring to the beamline and includes safety systems to prevent radiation exposure to those inside the end station and to prevent malfunctions within the end station from affecting the storage ring.[109] The beamline optics can include monochromators, diffraction gratings, and mirrors.[109] Most high energy beamlines operate with double crystal Si or Ge monochromators which transmits the diffracted beam parallel to the incident beam and can be detuned to remove harmonic energies.[97,109,110] Diffraction gratings serve the same purpose as monochromators but are generally used for low energy beamlines.[110] Mirrors are used for power filtering, harmonic rejection, collimation and focusing of the beam.[109] The end station is where experimentalists can physically manipulate the sample which they are analyzing.[109] The end station contains optics to view the sample, a sample stage that can manipulate the position of the sample, and detectors (e.g. fluorescence, ion chambers, etc.).[109]

XAS data can be collected in transmission, electron yield, or fluorescence modes.[100,110] A typical experimental setup for XAS measurements is shown in **Figure 1-8**. The incident X-ray beam passes through an ion chamber to determine the initial intensity of photons before being passed through the sample.[97] In a transmission experiment, the transmitted photons are measured by a second ion chamber.[97,110] The intensity of the transmitted photons (I_t) is dependent on the intensity of the incident photons (I_0), the sum of the absorption coefficients of all components of the material (μ), and the thickness (t) of the sample, following the Beer-Lambert law (Equation 1.12).[97,100] XAS spectra are plotted as the absorption coefficient, μ, as a function of energy.

$$I_t = I_0 e^{-\mu t} \tag{1.12}$$

It is important that the sample is of uniform thickness when obtaining transmission measurements to prevent pinhole effects.[97] If the sample is an uneven thickness, then the resulting transmission will be non-uniform.[97] It is possible to collect reference spectra concurrently with sample transmission spectra by placing a reference sample between the second ionization chamber and a third ionization chamber. Alternatively, reference spectra can be collected in the same manner as sample spectra.

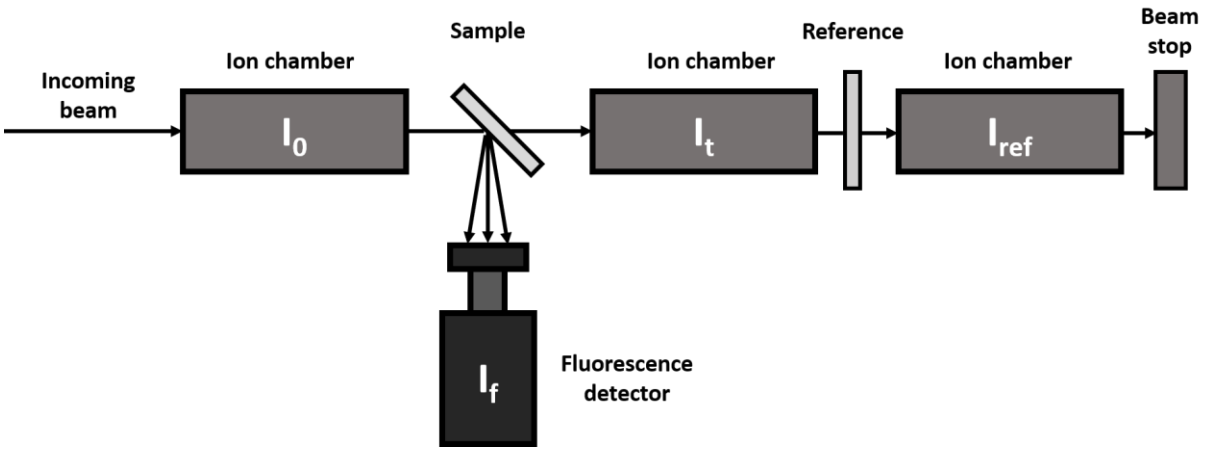

Figure 1-8 Schematic of a typical transmission/fluorescence XAS experimental beamline setup with reference spectra collected concurrently.

Transmission experiments directly measure the number of photons absorbed by the sample, but there are also indirect methods of measuring absorption. As previously discussed, there are two mechanisms by which an electron core-hole can be filled: fluorescence and Auger emission. Fluorescence is the preferred method of detection for samples with low concentrations of the element of interest and is widely used in the study of biological and environmental samples.[97,100] Fluorescence can be measured in air for hard X-rays, but ultrahigh vacuum conditions are required for soft X-rays to prevent the absorption of fluorescent photons by air molecules.[110] Electron yield modes measure the drain current required to replace electrons emitted from the material by Auger decay processes.[100,110] This detection mode is inherently surface sensitive due to the mean free path of the emitted photoelectrons.[100,110] Both fluorescence and electron yield signals are directly proportional to the absorption coefficient of the material ($I \propto \mu I_0$).[97,100]

1.6 Ion implantation

The nuclear decay of radionuclides can cause significant damage within a material.[1,14,43,66,111,112] Transuranium nuclides generally decay by the release of α-particles, which can cause up to 1000 displacements per atom (dpa) per decay event.[1,22,71,76,99,105] The emitted α-particle carries most of the decay event energy (4.5-5.5 MeV), however, the lower energy (70-100 keV) recoil nucleus is responsible for most of the structural damage which occurs.[1,22,28,29,37,43,71,76,112] Radiation-induced

structural damage can lead to volume swelling and cracking of the material, which in turn can increase the leach rate of radionuclides.[1,11,12,21,22,28,30,39,41,47,58,60,66,71,76,77,111] The incorporation of radionuclides into ceramic materials results in a crystalline to amorphous phase transition (metamiction) over extended periods of time, and it is important to understand how nuclear wasteforms behave during this process.[11,12,22,37,39,41,43,60,65,76,105,113] The two routes to study the effects of radioactive decay on materials are to incorporate short-lived radionuclides into the materials or to conduct ion implantation experiments.[21,24,37,39,58,71,112] The incorporation of radionuclides like ^{238}Pu or ^{244}Cm is the ideal method for studies of radiation-induced damage in materials; however, these studies tend to occur over the course of several years, require nuclear permits, and require characterization techniques specialized for the analysis of radioactive materials.[22,24,37,39,41,71,113] A more accessible option to study nuclear materials is to implant high energy heavy ions into simulator materials.[13,14,24,32,37,39,54,58,60,66,74,111,114] These materials contain simulator ions, such as rare-earth (RE) elements, which take the place of and simulate the chemistry of radionuclides in the structure.[13,40,50,60,75,115]

In an ion implantation experiment, a high energy beam of ions is focused onto the sample, with the temperature, ion energy, flux (ions/cm^{2}s), and total fluence (total ions/cm^2) experimentally controlled.[1,24,71,113] **Figure 1-9** shows a schematic of the Tandetron accelerator, located at the University of Western Ontario, which was used for ion implantation of materials in this thesis.[116] A duoplasmatron or sputter source produces ions from a gaseous or solid elemental material respectively.[116] The ions are then injected into the high-current Tandem accelerator, which accelerates the ions to MeV energies.[116] The high energy ions can then be used for several applications, including Rutherford backscattering spectroscopy (RBS), elastic recoil detection (ERD) analysis, medium energy ion scattering (MEIS), molecular beam epitaxy, and ion implantation.[37,116] The depth of ion implantation in solids varies depending on the energy and fluence of the ion beam, and the composition and density of the material.[116] The penetration depth of ions can be calculated using the program Stopping Range of Ions in Matter (SRIM).[117]

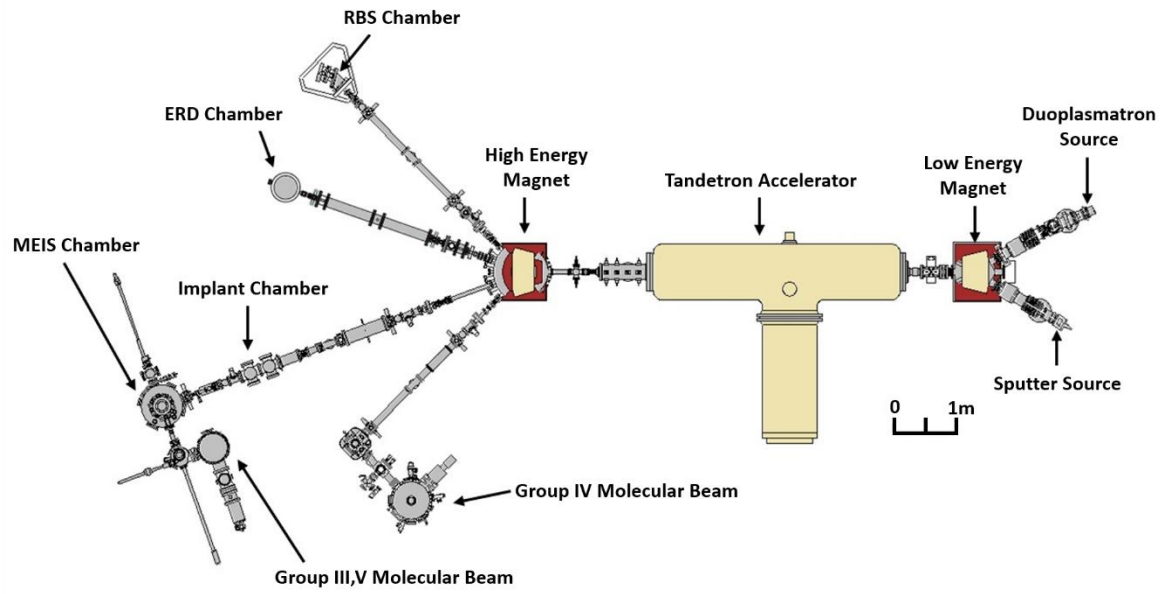

Figure 1-9 Schematic of the Tandetron accelerator located at the University of Western Ontario, used for ion implantation experiments. The diagram is adapted from the Interface Science Western (ISW) website.[116]

1.6.1 Glancing-angle XANES

Surface-sensitive characterization methods are required to study ion-implanted samples because ion implantation only affects the surface region of a material.[13,14,22,32,37,60,66,71] Glancing-angle X-ray absorption near edge spectroscopy (GA-XANES) can be used to investigate the damaged surface layer of materials.[32,60,66,99] This method is used to collect XANES spectra from different regions of a material. The X-ray attenuation depth in a material depends on the density of the material, the X-ray energy, and the angle at which the beam is set relative to the material.[98,118] In this technique, the incident X-ray beam is set to a low (glancing) angle relative to the surface of the material, rather than 45° as is common for fluorescence experiments. At very low angles (just above the angle of total external reflection) X-rays probe the near-surface region of the material.[13,14,32,60,66,98,118] As the angle is increased, the X-rays probe further into the material.[13,66,118] This method can thus be used to investigate the effect of radiation-induced damage in potential nuclear wasteforms.[13,32,60,66]

1.7 Thesis objectives

The Canadian nuclear industry has defined its waste management goal as being to "isolate and contain the radioactive material so that no long-term surveillance by future generations will be required and that there will be negligible risk to man and his environment at any time".[119] To achieve this objective, detailed structural information must be known about a wide range of materials. The research conducted in this thesis will contribute to the development of ceramic oxide materials and low-temperature synthesis methods for nuclear waste sequestration. This thesis has three main objectives:

1. Synthesize pyrochlore- and zirconolite-type oxides at lower annealing temperatures via coprecipitation and sol-gel methods. Lower temperature synthesis methods are more practical and economical than current high-temperature methods used for the production of nuclear wasteforms.
2. Determine the effect of synthesis method and/or annealing temperature on the long-range and local structure of pyrochlore- and zirconolite-type oxides using powder X-ray diffraction and X-ray absorption spectroscopy.
3. Investigate the effect of synthesis method and/or annealing temperature on the ability of pyrochlore- and zirconolite-type oxides to resist radiation-induced structural damage.

It is hypothesized that using solution-based synthesis methods such as coprecipitation and sol-gel will result in lower required annealing temperatures for the formation of ceramic oxides. Pyrochlore-type oxides were selected to test this hypothesis, with a second system (zirconolite-type oxides) being chosen to demonstrate that these synthesis methods can be applied to multiple ceramic systems. Additionally, since both ceramic systems have applications as nuclear wasteforms, it is important to demonstrate that synthesizing these materials at lower temperatures does not have an impact on the radiation resistance of the materials. It is expected that there should be no change in the radiation resistance properties of a material regardless of the method used to prepare the material.

Chapter 2 shows the low-temperature synthesis of $RE_2Ti_2O_7$ (RE = Sm, Gd, Yb) pyrochlore-type oxides via a coprecipitation method. **Chapter 3** shows the low-temperature synthesis of $CaZrTiO_7$ zirconolite-type oxides by coprecipitation and sol-gel methods. **Chapter 4**

shows the low-temperature synthesis of $RE_2Ti_2O_7$ (RE = Sm, Gd, Yb) pyrochlore-type oxides via a sol-gel method and examines the radiation resistance of pyrochlore and zirconolite-type oxides synthesized at low temperatures using coprecipitation and sol-gel methods compared to the same materials synthesized at high temperatures using the ceramic method. The results from **Chapters 2**, **3**, and **4** are summarized and discussed in **Chapter 5** in relation to pyrochlore- and zirconolite-type oxides prepared by the ceramic method and recommendations for future experiments are suggested.

Chapter 2

Low-temperature synthesis of $RE_2Ti_2O_7$ (RE = Sm, Gd, Yb) pyrochlore-type materials via a coprecipitation method*

2.1 Introduction

Pyrochlore-type oxides have been investigated for a variety of applications, including catalysis, ferromagnetism, luminescence, ionic conductivity, and radioactive waste sequestration.[22,51,55–57,61–64,70,80,83,84,86,88,120–124] A wide range of pyrochlore compositions has been found to demonstrate characteristics suitable for a nuclear wasteform. It has been shown that oxides adopting the pyrochlore structure can incorporate large amounts of U, Th, and Pu with high loading.[53,65,70,74,125–129] Pyrochlore compositions containing Ti or Zr have also been shown to be chemically durable and resistant to radiation-induced structural damage, which is important for the long-term reliability of these materials as wasteforms. [31,33,39,46,47,52–54,59,67–70,73,74]

The typical synthesis method used to form these materials is the conventional high-temperature solid-state (ceramic) route which requires high annealing temperatures and long annealing times.[59,64,79,80,82,83,85,86] Large-scale production of these materials is much more practical and economically feasible if performed at lower temperatures. This is difficult to achieve by the ceramic method due to the solid-state diffusion limitations that are imposed by mechanical mixing of reactants. This type of mixing results in well-mixed particles, but highly inhomogeneous mixtures at the atomic scale.[46,49,59,80,82–85] The introduction of a solution-based synthesis method may reduce the required annealing temperature by mixing the precursors at a near-atomic level, reducing the diffusion distances required for ions to travel to form the desired material. Several wet chemical approaches have been reported to synthesize pyrochlore-type oxides, including

* A version of this chapter, authored by Sarah McCaugherty, Alicia Koo, and Andrew P. Grosvenor, has been submitted for publication. The manuscript has been reformatted for inclusion in this thesis. The Introduction section has been altered to avoid excessive repetition of Chapter 1 content.

hydrothermal methods,[64,84,86] coprecipitation,[30,51,55,56,69,80,83,120,130] and sol-gel processing,[61,62,67,88,123,124] however, the effect of synthesis conditions on the long-range and local structures of these materials has not been examined.

The long- and short-range structure of $RE_2Ti_2O_7$ (RE = Sm, Gd, Yb) pyrochlore-type materials synthesized at varying temperatures via a coprecipitation method were investigated in this study by use of powder X-ray diffraction (XRD) and X-ray absorption near-edge spectroscopy (XANES). Materials prepared by the ceramic method were also studied so as to understand the effect of the synthetic method on the structure of these materials. Typical coprecipitation syntheses involve the precipitation of all precursors concurrently as hydroxides or oxalates. This study has shown that the resulting powders can then be annealed to form a homogeneous crystalline product at lower temperatures than by the ceramic method over comparable (or shorter) annealing times.

2.2 Experimental

2.2.1 Synthesis

$RE_2Ti_2O_7$ (RE = Sm, Gd, Yb) materials were synthesized using the ceramic method and a coprecipitation method. For the ceramic method, Sm_2O_3 (Alfa Aesar, 99.9%), Gd_2O_3 (Alfa Aesar, 99.99%), or Yb_2O_3 (Alfa Aesar, 99.9%) and TiO_2 (Alfa Aesar, 99.6%) powders were mixed stoichiometrically and pressed into pellets uniaxially at 6 MPa. The pellets were placed in alumina crucibles and heated in air at 1400 °C for 6 days or 800 °C for 12 days with intermediate grinding and pelleting after every 3 days of annealing. For the coprecipitation method, the rare earth oxides (Sm_2O_3, Gd_2O_3, Yb_2O_3) were first dissolved in hot (30 - 90 °C) concentrated HNO_3 (Fisher Scientific, 70%). The solutions were cooled to room temperature before the stoichiometric addition of $Ti[OC(CH_3)_3]_4$ (Acros Organics, 98%). NH_4OH (Fisher Scientific, 28.0-30.0%) was added to the solutions until a pH of 10 was reached to precipitate all metals as hydroxides. The mixtures were then vacuum filtered using ashless filter paper, and the precipitate and filter paper were heated at 650 °C to burn off the filter paper, leaving only the dry powder precursor. The powders were pelletized and annealed in a tube furnace at temperatures ranging from 700 to 1400 °C for 3 (1400, 1300, 1200, 1100 °C), 6 (1000, 900 °C), or 9 days (800, 700 °C), followed by the removal of the sample from the furnace and cooling in air.

2.2.2 Powder XRD

Diffraction patterns used for phase analysis were collected using a PANalytical Empyrean X-ray diffractometer with a Co $K\alpha_{1,2}$ X-ray source operating at 40 kV and 45 mA. Diffraction patterns used for phase analysis were collected in the 2θ range of 10-80° with a step size of 0.017°. Diffraction patterns used for Rietveld refinement were collected in the 2θ range of 10-130° with a step size of 0.017°. Rietveld refinement was performed using the PANalytical X'Pert HighScore Plus software program. The scale factor, zero shift, lattice constant, oxygen 48f(x) positional parameter, profile variables, and the overall isotropic thermal parameter (B_{OVL}) were allowed to vary during the refinement. It should be noted that B_{OVL} was set to 0.5 when it could not be refined accurately. The crystallite size was calculated from the powder X-ray diffraction data using the Scherrer equation (Equation 1.11). The line broadening of the instrument was determined from a polycrystalline Si reference disk and subtracted from the experimental FWHM to give the corrected line broadening value (*B*). The crystallite size was calculated from the four highest intensity diffraction peaks and the error was determined from the standard deviation of these calculated values.

2.2.3 SEM

Scanning electron microscopy (SEM) was used to study the particle size of $Gd_2Ti_2O_7$ materials prepared by the coprecipitation method and annealed at 700, 800, and 1400 °C. Imaging was performed using a JEOL 840A scanning electron microscope. Samples were mounted on double-sided carbon tape and sputter coated with approximately 200 Å of gold prior to loading them into the SEM. Images were acquired at 15 kV under a working distance of 15 mm and were analyzed using Gellar Analytical's dPict image acquisition software.

2.2.4 Ti K-edge XANES

Ti K-edge XANES spectra were collected using the Sector 9 and Sector 20 bending magnet beamlines (9BM and 20BM) located at the Advanced Photon Source (APS; Argonne National Laboratory).[131] Samples were finely ground, spread onto Kapton tape, and layered to maximize absorption. XANES spectra were collected in partial fluorescence mode using a 13-element Ge detector, and transmission mode with a mixture of He and N_2 gases in the incident ionization

chamber and 100 % N_2 gas in the transmission and reference ionization chambers. A Si (111) double crystal monochromator was used, providing a spectral resolution of 0.7 eV at 4966 eV.[131] Spectra from Ti metal foil (E_0 = 4966 eV) were collected concurrently in transmission mode and used for calibration. XANES spectra were collected using a step size of 0.15 eV through the absorption edge. All XANES spectra presented here were calibrated, normalized, and analyzed using the Athena software program.[132]

2.3 Results and Discussion

2.3.1 XRD and Rietveld Refinement

The powder XRD patterns from the $RE_2Ti_2O_7$ (RE = Sm, Gd, Yb) materials prepared by the ceramic and coprecipitation methods using different annealing temperatures are presented in **Figure 2-1,** where the intensities of the patterns have been normalized to a value of 1. The XRD patterns of materials prepared by the coprecipitation method and annealed at temperatures ranging from 700 to 1400 °C, as well as the materials prepared by the ceramic method and annealed at 1400 °C, confirmed the formation of the pyrochlore phase. The only material which was shown to contain crystalline impurities was $Sm_2Ti_2O_7$ annealed at 700 °C, which contains the unreacted starting materials TiO_2 (rutile) and Sm_2O_3. The crystallinity of the pyrochlore materials decreased as the annealing temperature was lowered, as shown by a broadening of the diffraction peaks. The diffraction peaks were very broad and low in intensity when the annealing temperature was decreased to 700 °C, indicating that the pyrochlore phase was not fully crystallized and may contain an amorphous fraction. A comparison of the unscaled diffraction patterns from the pyrochlore-type materials annealed at 700 and 1400 °C are shown in **Figure A1**. The crystallinity of the materials annealed at 700 and 800 °C was not observed to improve with prolonged heating. The samples prepared by the ceramic method and annealed at 800 °C resulted in the formation of a small amount of the desired pyrochlore phase with unreacted starting materials as the major phases (diffraction patterns not shown). $RE_2Ti_2O_7$ (RE = Sm, Gd, Yb) materials are generally reported to form phase pure after annealing at 1200 °C or higher when prepared by the ceramic method.

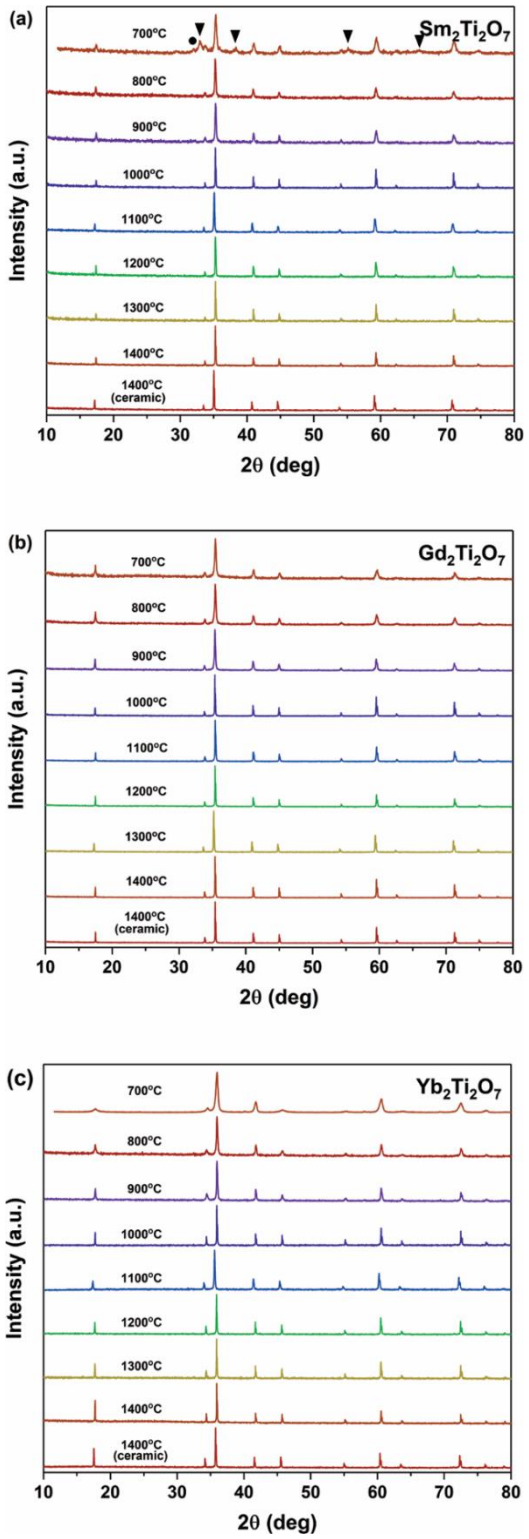

Figure 2-1 Powder XRD patterns for **(a)** $Sm_2Ti_2O_7$ (triangles show peaks originating from Sm_2O_3 and diamonds show peaks from TiO_2), **(b)** $Gd_2Ti_2O_7$, and **(c)** Yb_2Ti2O_7 prepared by the coprecipitation method. Patterns are compared to the same material prepared by the ceramic method and annealed at 1400 °C.

The long-range order of the pyrochlore materials annealed at high and low temperatures was examined by Rietveld refinement of the powder XRD patterns from $Gd_2Ti_2O_7$ annealed at 1400, 1100, and 800 °C, and $Sm_2Ti_2O_7$ and $Yb_2Ti_2O_7$ annealed at 1400 and 800 °C. The diffraction patterns from materials annealed at 700 °C were not refined as these materials were not fully crystalline, as determined from the Ti K-edge XANES spectra (*vide infra*). Peaks corresponding to a small quantity of impurity in the material are present in the patterns but were not included in the refinement. The refined patterns show good fits to the experimental data, as shown in **Figure 2-2**, **A2**, and **A3**. The refined lattice constant, oxygen 48f(x) positional parameter, B_{OVL}, and agreement indices for the $Gd_2Ti_2O_7$ materials prepared by the coprecipitation method are presented in **Table 2-1** (refined data for $Sm_2Ti_2O_7$ and $Yb_2Ti_2O_7$ materials is presented in **Table A1**). Given little to no change in the lattice constant and positional parameter of these materials, it can be concluded that only minor changes are observed in the long-range structure of $RE_2Ti_2O_7$ materials prepared by the coprecipitation method when the annealing temperature was decreased from 1400 to 800 °C.

Table 2-1 Rietveld refinement results for $Gd_2Ti_2O_7$ materials prepared by the coprecipitation method and annealed at 1400, 1100, and 800 °C.

	$Gd_2Ti_2O_7$		
Annealing Temperature	**1400°C**	**1100°C**	**800°C**
Lattice constant, a (Å)	10.17669(5)	10.18313(6)	10.1840(1)
O 48f(x) positional parameter, x	0.4261(5)	0.4294(4)	0.4275(4)
B_{OVL}	1.26(3)	0.5	0.52(2)
R_{exp}	5.77433	6.43333	5.54593
R_p	5.9622	8.02426	5.69274
R_{wp}	7.63122	10.35648	7.17571
χ^2	1.74657	2.59151	1.6741

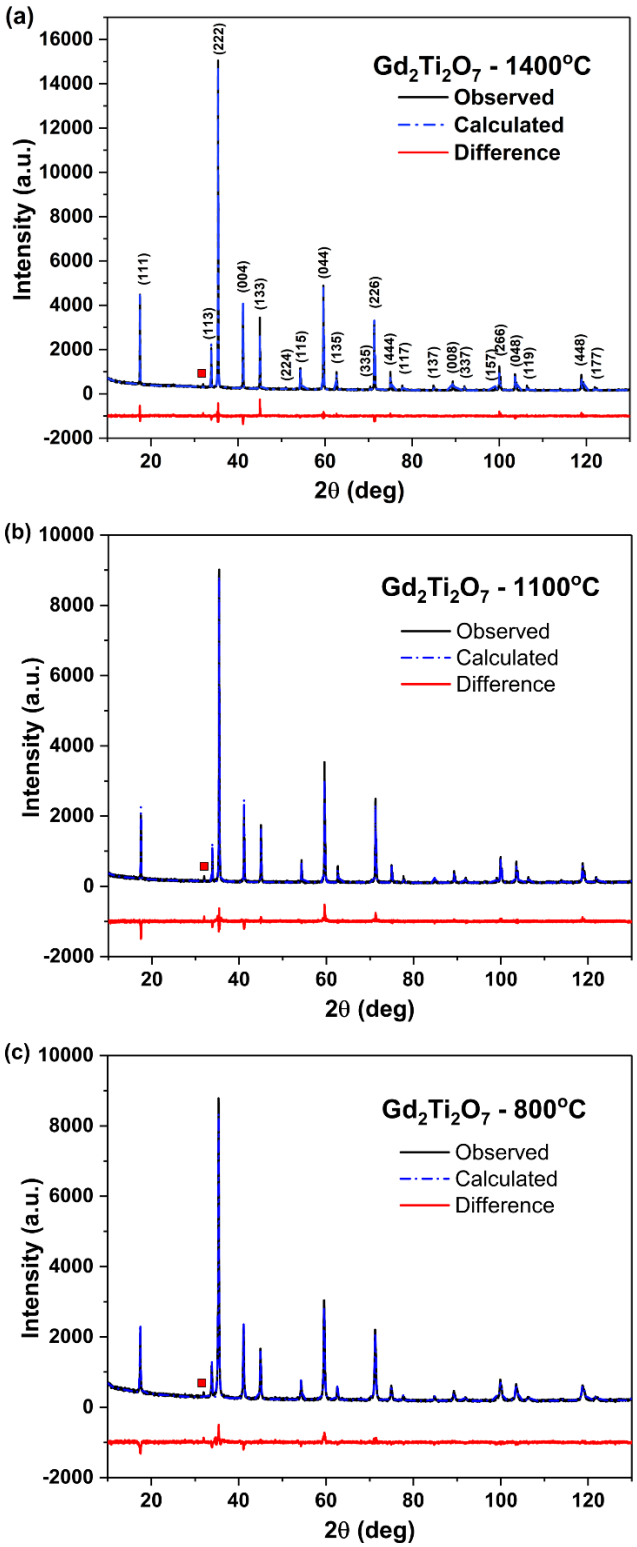

Figure 2-2 Rietveld refined powder XRD patterns from $Gd_2Ti_2O_7$ prepared by the coprecipitation method and annealed at **(a)** 1400 °C, **(b)** 1100 °C, and **(c)** 800 °C. Squares mark impurity peaks which were not included in the refinements.

2.3.2 Crystallite and Particle Size

The crystallite size of the $RE_2Ti_2O_7$ (RE = Sm, Gd, Yb) materials after annealing at various temperatures were calculated by the Scherrer equation and are shown in **Figure 2-3**. The crystallite size of the materials increases with annealing temperature, as is expected. The large crystallite size after annealing at high-temperature results in decreased reliability of the Scherrer equation, and thus large error bars. The materials that were annealed at low temperature show a very narrow range of calculated crystallite size. SEM was used to confirm this trend in crystallite size, as the crystallite and particle size should be related. **Figure 2-4** shows SEM images from $Gd_2Ti_2O_7$ powders prepared by the coprecipitation method and annealed at 1400, 800, and 700 °C. The average particle size of the powders decreased from more than 1 μm (**Figure 2-4(a)**) to less than 500 nm (**Figure 2-4(b)**) when the annealing temperature was decreased from 1400 to 800 °C. No apparent change in the particle size was observed when the annealing temperature was reduced from 800 to 700 °C (**Figure 2-4(c)**). The particle size distribution within the SEM images of the materials annealed at low temperatures (700 and 800 °C) appear to be very narrow (tens of nanometers), especially when compared to the images from the material annealed at high temperature (several hundred nanometers). These trends are consistent with the trends observed for the calculated crystallite sizes of the materials.

2.3.3 Ti K-edge XANES

Titanium K-edge XANES spectra were collected to determine the effect of decreasing annealing temperature on the short-range order of the pyrochlore-type structure and are presented in **Figure 2-5**. XANES is a powerful technique for investigating the structural and electronic properties of materials. The shape and intensity of the pre-edge and main-edge features provide information on the local coordination number (CN), oxidation state, and bonding environment of the absorbing atom.[13,14,66,108] The spectra consist of two regions: low-intensity quadrupolar transitions (pre-edge; 1s→3d; A) and high-intensity dipolar transitions (main-edge; 1s→4p; B and C).[13,66,102,108]

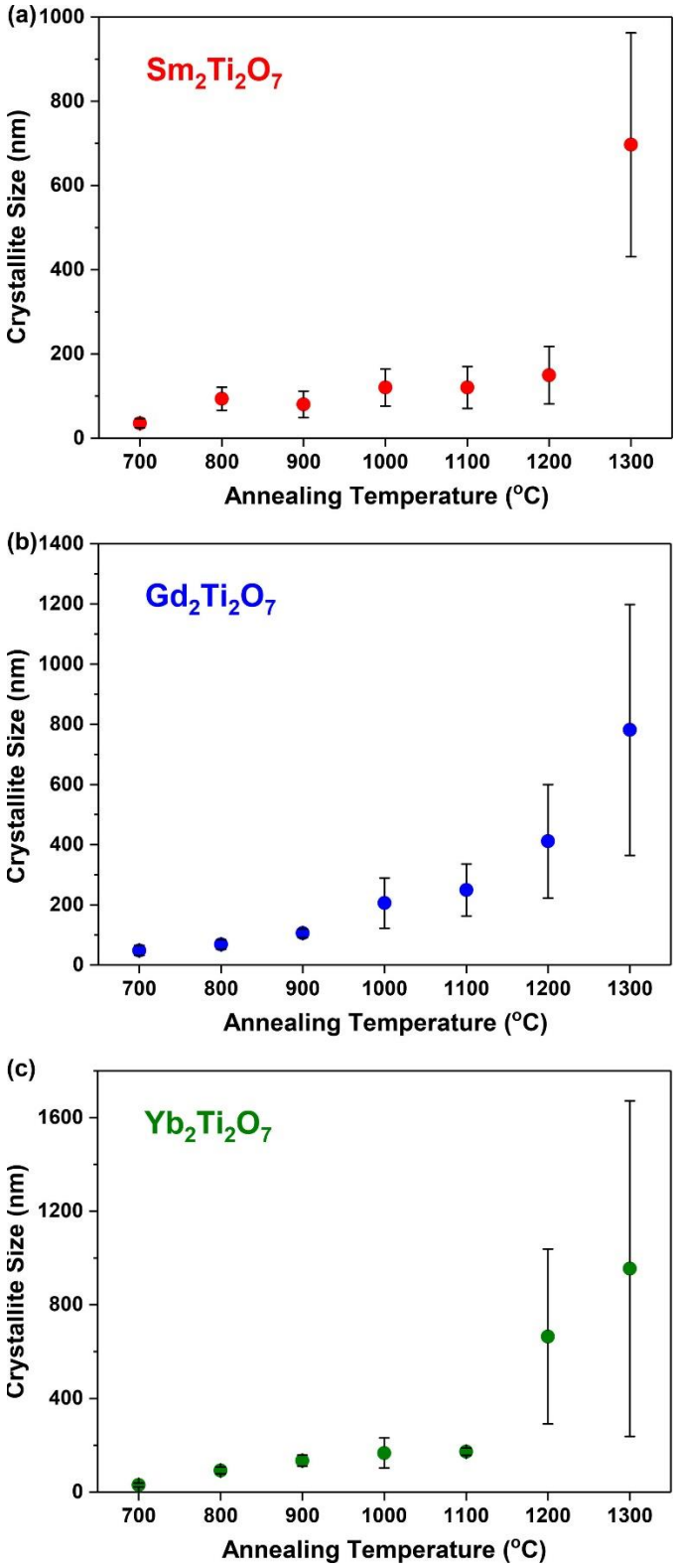

Figure 2-3 Crystallite size calculated by the Scherrer equation from the powder XRD patterns from **(a)** $Sm_2Ti_2O_7$, **(b)** $Gd_2Ti_2O_7$, and **(c)** $Yb_2Ti_2O_7$ materials prepared by the coprecipitation method. Error bars correspond to the standard deviation of the calculated values.

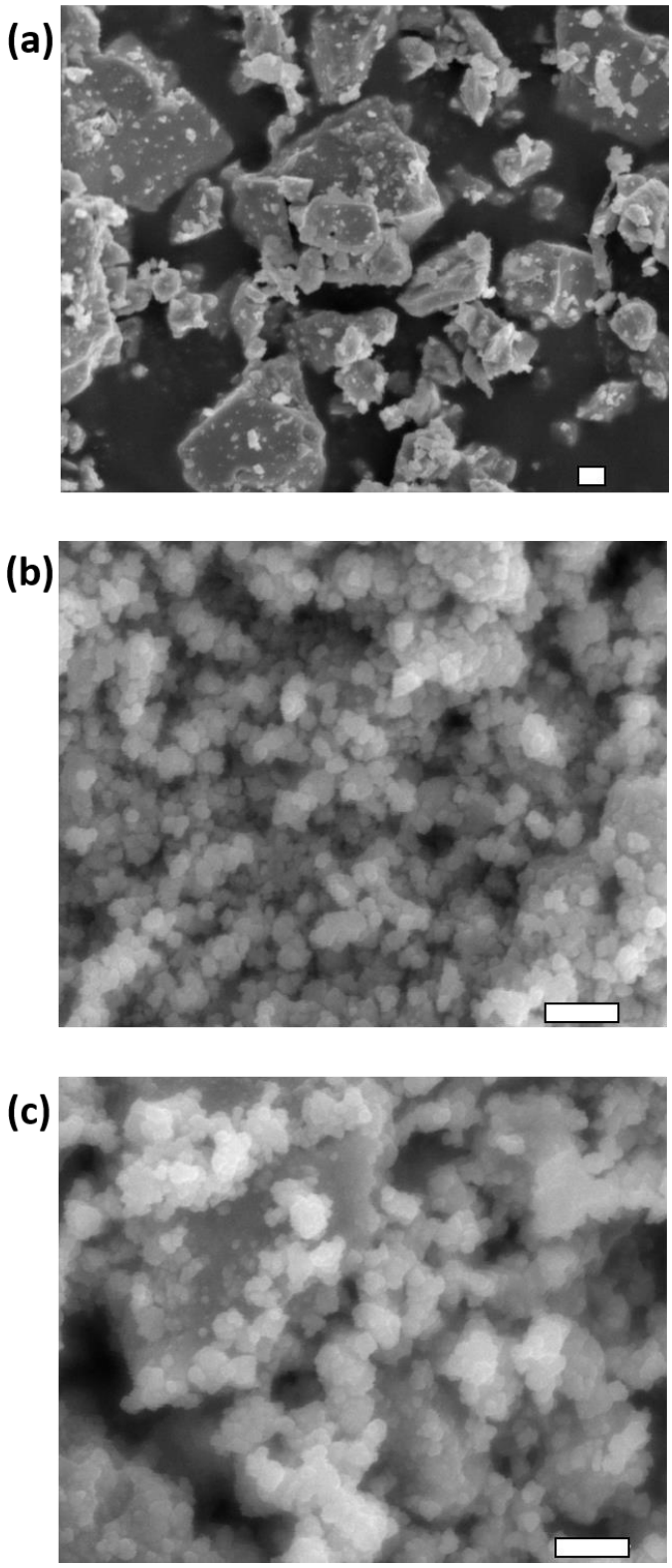

Figure 2-4 SEM images of $Gd_2Ti_2O_7$ materials prepared by the coprecipitation method and annealed at **(a)** 1400 °C (5,000x magnification), **(b)** 800 °C (20,000x magnification), and **(c)** 700 °C (20,000x magnification). The scale bars are 1 μm.

The pre-edge region is divided into three features (A_1, A_2, and A_3) because of crystal field splitting of the 3d states (A_1: 1s→3d t_{2g} and A_2: 1s→3d e_g^*) and non-local excitations (A_3: intersite-hybrid).[14,66,106,108] The intersite-hybrid peak results from the excitation of a 1s electron of the absorbing atom through an O 2p orbital to the next-nearest-neighbour (NNN) Ti 3d orbital.[66] The intensity of this feature is dependent on the overlap of the Ti 4p, O 2p, and NNN Ti 3d orbitals.[66,108]

The XANES spectra for each pyrochlore composition prepared by the coprecipitation method and annealed from 1400 to 800 °C show nearly identical line shapes to the spectra from the samples prepared by the ceramic method and annealed at 1400 °C. This line shape is characteristic of Ti^{4+} in a distorted octahedral environment.[13,14,66,68,102,103,106,108,133] The spectra from all materials annealed at 700 °C show an increase in the intensity of the pre-edge features and a decrease in intensity and broadening of the main edge features. The changes in the pre-edge features can be attributed to a decrease in the coordination number of Ti.[14,66,102,103,106,108,133] As the coordination number decreases, the dipole character of the quadrupolar transition increases due to increased overlap of the Ti 4p and 3d orbitals.[14,66,102,106,108] This decrease in coordination number can be attributed to the presence of Ti in the amorphous precursor materials, wherein metals may be 4-, 5-, or 6-coordinate.[102,103,105,133] The changes in the main edge features of the XANES spectra from the sample annealed at 700 °C corresponds to increased disordering of the material, which results in variation of the absorption energy from different coordination sites.[102,133] The combination of XANES and XRD measurements indicates that an annealing temperature of 700 °C is insufficient to convert all amorphous starting materials to the pyrochlore structure using the coprecipitation method, even with prolonged heating.

A trend in the intensity of the intersite-hybrid peak (A_3) was also observed depending on the annealing temperature; the intensity of this feature was observed to decrease with decreasing annealing temperature. The intensity of the intersite-hybrid peak is dependent on the overlap of the absorbing Ti 4p orbital, the nearest-neighbour O 2p orbital, and the next-nearest-neighbour Ti 3d orbital.[66] The observed trend can be attributed to some local disorder within the material. Disordering of Ti would result in changes in the bond angles and increased bond lengths, which would result in a decrease in the overlap of the above-mentioned orbitals.

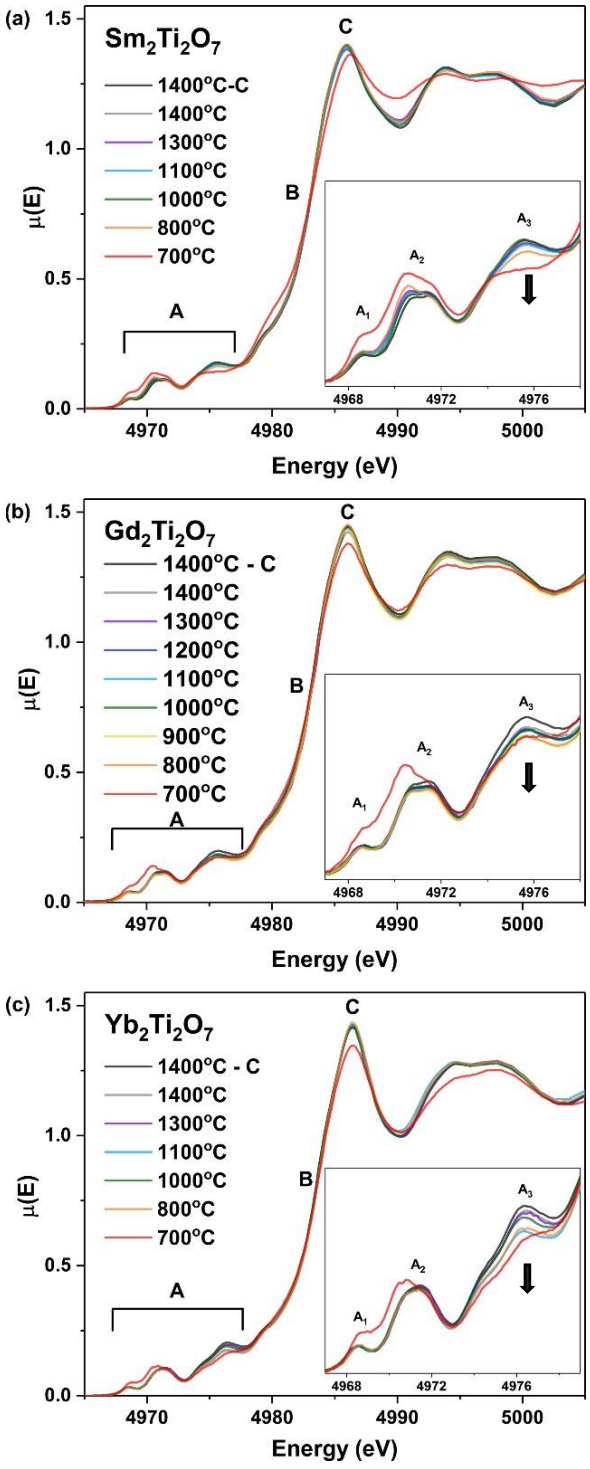

Figure 2-5 Ti K-edge XANES spectra from **(a)** $Sm_2Ti_2O_7$, **(b)** $Gd_2Ti_2O_7$, and **(c)** $Yb_2Ti_2O_7$ prepared by the coprecipitation method and annealed at temperatures from 700 to 1400 °C. Black spectra are from the same material prepared by the ceramic method. The features A_1, A_2, and A_3 correspond to $1s \rightarrow 3d\ t_{2g}$, $1s \rightarrow 3d\ e_g^*$, and intersite-hybrid excitations respectively. Features B and C represent the main-edge region of the spectrum. Arrows show changes in the spectra with decreasing annealing temperature.

2.4 Conclusions

Pyrochlore-type oxides ($RE_2Ti_2O_7$; RE = Sm, Gd, Yb) have been synthesized using a coprecipitation method with annealing temperatures ranging from 700 to 1400 °C. Minor changes in the long-range and local structure of the materials were observed as evidenced by small increases in the lattice constants and decreases in the intensity of the Ti K-edge intersite hybrid peak with decreasing annealing temperature. The materials annealed at 700 °C were poorly crystalline (likely with an amorphous fraction) which was confirmed by analysis of the Ti K-edge XANES spectra. The Ti K-edge XANES spectra from these materials showed an increase in the intensity of the pre-edge region and decrease in the intensity and broadening of main edge features due to the presence of Ti in an amorphous phase. The line shape of all Ti K-edge XANES spectra from materials annealed between 800 and 1400 °C was identical except for the intensities of the intersite-hybrid peaks, which is attributed to a slight local disordering of the Ti coordination environment with decreasing annealing temperature. It has been shown here that crystalline pyrochlore-type oxides can be prepared using a coprecipitation method and annealing temperatures as low as 800 °C with only minor changes to the short- and long-range order of the materials being observed.

Chapter 3

Low-temperature synthesis of $CaZrTi_2O_7$ zirconolite-type materials via coprecipitation and sol-gel methods*

3.1 Introduction

The zirconolite-type structure is related to the pyrochlore structure, as was described in **Section 1.2.2.2**, and has been investigated for several decades for nuclear waste sequestration applications. It was shown in the previous chapter that the annealing temperature required to form pyrochlore-type oxides could be substantially reduced by using a coprecipitation method to form the precursor powder. It was thus desirable to determine whether these results could be extended to another ceramic system which is relevant for nuclear waste sequestration applications.

The sol-gel method is one of the most widely used solution-based synthesis methods to prepare ceramic materials. This technique is broadly defined as the formation of a gel from a solution, resulting in the formation of a three-dimensional solid network.[79,82,85] A relatively small amount of energy is required to arrange the ions into an ordered, crystalline material because the solid structure is already mostly formed. Another solution-based synthesis method, coprecipitation, requires the precipitation of all metals in solution, typically as hydroxides.[46,80,81] The diffusion distances required to form the material are shortened due to the very small particle size of the precursors, which reduces the energy required to form the product.

In contrast to these solution-based synthesis methods, the ceramic method requires the diffusion of ions through many lattice sites and defects, which is a much higher energy process. Sol-gel and coprecipitation methods are commonly used to prepare materials at relatively lower

* A version of this chapter, authored by Sarah McCaugherty and Andrew P. Grosvenor, has been submitted for publication. The manuscript has been reformatted for inclusion in this thesis. The Introduction section has been altered to avoid excessive repetition of Chapter 1 content.

annealing temperatures for this reason, particularly in synthetic applications where high temperatures are not feasible.[22,46,64,74,84–88] In terms of nuclear waste sequestration applications, industrial-scale synthesis of wasteform materials needs to be as cost-effective as possible. Low-temperature synthesis methods are thus highly desirable, as they reduce equipment and operating costs.

In this study, zirconolite-type ($CaZrTi_2O_7$) materials were prepared by ceramic, coprecipitation, and sol-gel methods to determine the effect of synthesis method on the long-range and local structures of the materials. The synthesized materials were studied using a combination of powder XRD and XANES to determine the lowest temperature at which phase-pure $CaZrTi_2O_7$ was formed.

3.2 Experimental

3.2.1 Synthesis

Zirconolite-type materials ($CaZrTi_2O_7$) were synthesized using the ceramic method, a coprecipitation method, and a sol-gel method. For the ceramic method, $CaCO_3$ (EMD, ≥99.0%), ZrO_2 (Alfa Aesar, 99.7%), and TiO_2 (Alfa Aesar, 99.6%) powders were mixed stoichiometrically and pressed into a pellet uniaxially at 6 MPa. The pellet was placed in an alumina crucible and heated in air at 1450 °C for 6 days with intermediate grinding and pelleting after 3 days of annealing, followed by quench cooling in air.

For the coprecipitation method, calcium carbonate, titanium tert-butoxide, and an aqueous zirconium solution were used as reagents. The zirconium solution was prepared by dissolving $ZrOCl_2 \cdot xH_2O$ (Alfa Aesar, 99.9%) in HNO_3 (pH≈1). The concentration of zirconium in this solution was determined by ICP-AES analysis. $CaCO_3$ and $Ti[OC(CH_3)_3]_4$ (Acros Organics, 98%) were added to an appropriate amount of the zirconium solution and stirred until dissolved. $CaCO_3$ was added in 100% stoichiometric excess to account for the partial solubility of $Ca(OH)_2$.[45] NH_4OH (Fisher Scientific, 28.0-30.0 %) was then added to the solution until a pH of 10 was reached to precipitate all metals as hydroxides. The mixtures were then vacuum filtered, and the filter paper was burned off at 650 °C, resulting in a dry powder precursor. The white powders were

pelletized and annealed at temperatures ranging from 900 to 1400 °C for 6 days or 700 to 800 °C for 12 days followed by quench cooling in air.

A modified Pechini method was used for the sol-gel method due to the compatibility of this method with aqueous reagents. As previously discussed in **Section 1.3.3**, the Pechini method results in gelation by the condensation polymerization of a polyhydroxy alcohol and a carboxylic acid metal complex, which are typically ethylene glycol and citric acid, respectively.[22,82,85] An appropriate amount of zirconium solution was first concentrated to ~1 mL by heating to evaporate excess water (to improve the quality of the gel obtained and gelation time) followed by the addition of 2 mL of ethylene glycol (Alfa Aesar, 99%) to prepare 0.25 g of product. Stoichiometric amounts of $CaCO_3$ and $Ti[OC(CH_3)_3]_4$ were then added along with 1 mL of concentrated HNO_3 and 0.5 mL of glacial acetic acid (Fisher, 99.7%). The solution was stirred in a sand bath at 80±5 °C for ~2 hours until an opaque white gel was obtained. The gel was then dried in a furnace at 250 °C for 1 hour, resulting in a fine black powder. This powder was ground and heated at 650 °C for 6 hours to burn off any remaining carbon-containing components, resulting in a fine white powder. This powder was then pelleted and annealed at 1400 °C for 3 days, 1200 or 900 °C for 6 days, or 800 °C for 9 days with intermediate grinding as previously described, followed by quench cooling in air.

3.2.2 Powder XRD

Diffraction patterns used for phase analysis were collected using a PANalytical Empyrean X-ray diffractometer with a Co $K\alpha_{1,2}$ X-ray source operating at 40 kV and 45 mA in the 2θ range of 10-80° with a step size of 0.017°. Diffraction patterns used for Rietveld refinement were collected using a PANalytical Empyrean X-ray diffractometer with a Cu $K\alpha_{1,2}$ X-ray source operating at 40 kV and 45 mA in the 2θ range of 10-110° with a step size of 0.017°. Rietveld refinement was performed using the X'Pert HighScore Plus software program. The scale factor, zero shift, lattice constants, atomic positional parameters, profile variables, and the overall isotropic thermal parameter (B_{OVL}) were allowed to vary during the refinement. The XRD figures presented in this chapter are presented with 2θ values representative of a Co X-ray source.

3.2.3 SEM

Scanning electron microscopy (SEM) was performed to study the particle size of $CaZrTi_2O_7$ materials prepared by the ceramic method (annealed at 1400 °C), the coprecipitation method (annealed at 900 °C), or the sol-gel method (annealed at 900 °C). Imaging was performed using a JEOL 840A scanning electron microscope. Samples were mounted on double-sided carbon tape and sputter coated with approximately 200 Å of gold prior to loading them into the SEM. Images were acquired at 15 kV under a working distance of 15 mm and were analyzed using the Gellar Analytical's dPict image acquisition software program.

3.2.4 Zr K-edge XANES

Zr K-edge XANES spectra were collected using the Sector 20BM beamline located at the APS.[131] Samples were finely ground, spread onto Kapton tape, and layered to maximize absorption. XANES spectra were collected in partial fluorescence mode using a 13-element Ge detector and transmission mode with 100 % N_2 gas in the incident ion chamber and a mixture of Ar and N_2 gases (70:30) in the transmission and reference chambers. A Si (111) double crystal monochromator was used, providing a spectral resolution of 2.5 eV at 17998 eV.[131] Spectra from Zr metal foil (E_0 = 17998 eV) were collected concurrently in transmission mode and used for calibration. XANES spectra were collected using a step size of 0.3 eV through the absorption edge.

3.2.5 Ti K-edge XANES

Ti K-edge XANES spectra were collected using the Sector 20BM beamline located at the APS.[131] Samples were finely ground, spread onto Kapton tape, and layered to maximize absorption. XANES spectra were collected in partial fluorescence mode using a 13-element Ge detector and transmission mode with a mixture of He and N_2 gases (70:30) in the incident ion chamber and 100% N_2 gas in the transmission and reference chambers. A Si (111) double crystal monochromator was used, providing a spectral resolution of 0.7 eV at 4966 eV.[131] Spectra from Ti metal foil (E_0 = 4966 eV) were collected concurrently in transmission mode and used for calibration. XANES spectra were collected using a step size of 0.15 eV through the absorption edge. All XANES (Ti K- and Zr K-edge) spectra presented here were calibrated, normalized, and analyzed using the Athena software program.[132]

3.3 Results and Discussion

3.3.1 Powder XRD and Rietveld Refinement

The powder XRD patterns from $CaZrTi_2O_7$ zirconolite-type materials prepared by the coprecipitation and sol-gel methods are presented in **Figure 3-1(ab)**. These patterns are compared to the diffraction pattern from the material prepared by the ceramic method and annealed at 1450 °C. The XRD patterns of materials prepared by the coprecipitation or sol-gel method and annealed at temperatures ranging from 800 to 1400 °C confirmed the formation of the zirconolite phase. $CaZrTi_2O_7$ zirconolite-type materials are generally reported to form phase pure after annealing at 1200 °C or higher when prepared by the ceramic method. The pattern from the material prepared at 800 °C show the presence of an unknown phase. To further investigate this phase, a material was prepared by the coprecipitation method and annealed at 700 °C. **Figure 3-1(c)** shows that after annealing at 700 °C, only peaks corresponding to the unknown phase were observed. The peak positions and relative intensities are indicative of a defect fluorite structure. Rietveld refinement was performed on the XRD pattern from this material, using a $(Ca_{0.25}Zr_{0.25}Ti_{0.5})O_{1.75}$ defect fluorite structure as the model. The theoretical site occupancy values were used due to the difficulty in refining site occupancies of three atoms in one site. The results from this refinement are shown in **Figure 3-1(d)**. The calculated pattern shows a good fit to the experimental pattern.

The long-range order of the zirconolite materials prepared by the coprecipitation and sol-gel methods and annealed at high (1300/1400 °C) and low (900 °C) temperatures was examined by Rietveld refinement of the powder XRD patterns. The diffraction patterns from materials annealed at 800 °C were not refined as these materials were not phase-pure zirconolite, as discussed above. The refined patterns show good fits to the experimental data, as shown in **Figure 3-2**. Small changes in the lattice parameters and atomic coordinates (**Table 3-1**) were observed depending on the annealing temperature used. Generally, *a*, *c*, and β increased, and *b* decreased with decreasing annealing temperature. Despite these changes in lattice parameters, there was <0.1% change in the unit cell volume. Therefore, the materials prepared at high and low temperatures using either synthesis method (coprecipitation or sol-gel) show very little long-range structural change.

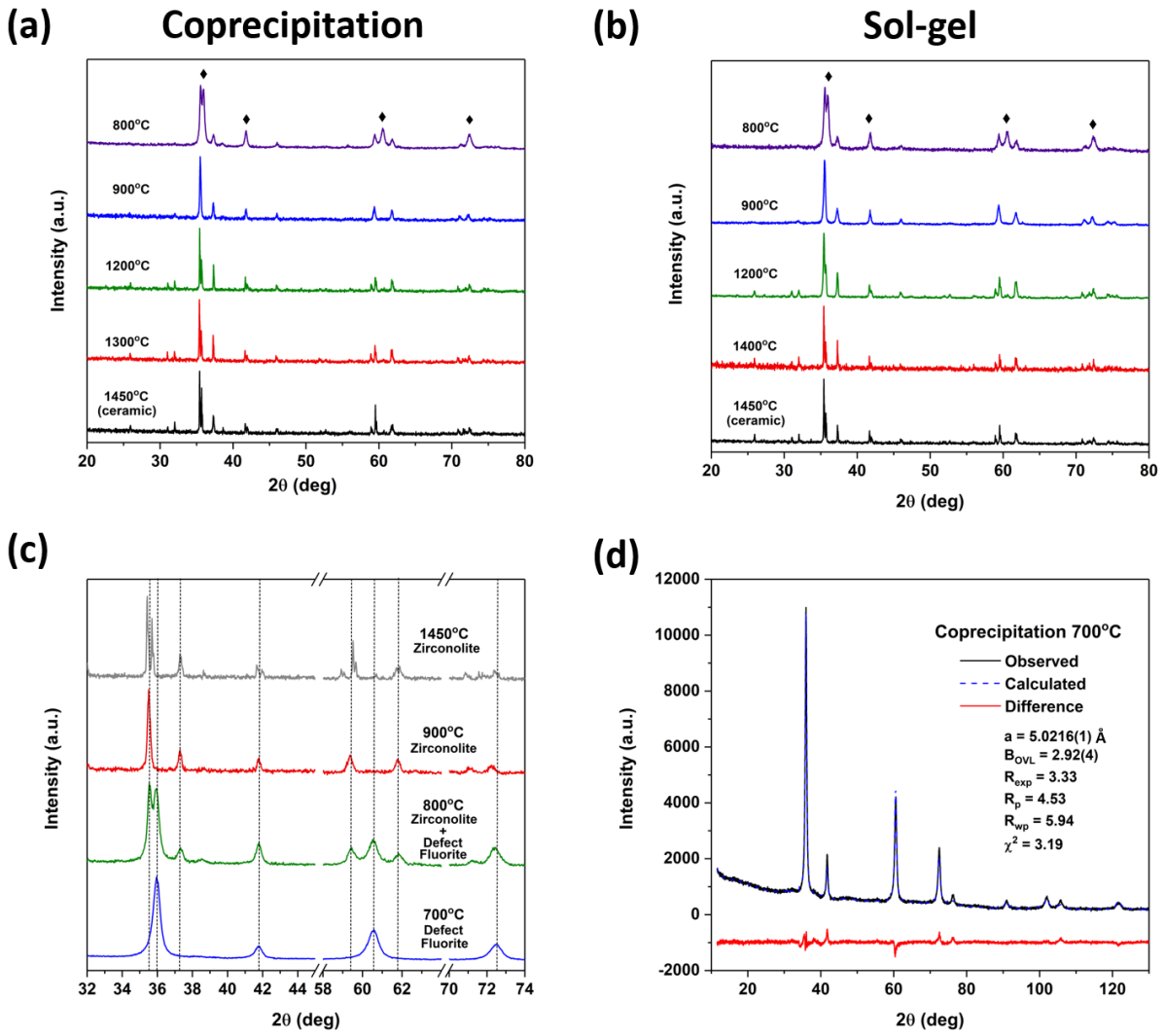

Figure 3-1 Powder XRD patterns for $CaZrTi_2O_7$ zirconolite-type materials prepared by the **(a)** coprecipitation and **(b)** sol-gel methods. All patterns are compared to $CaZrTi_2O_7$ prepared by the ceramic method and annealed at 1450 °C. Diamonds indicate peaks from an unknown phase. **(c)** Enlarged XRD patterns from $CaZrTi_2O_7$ materials prepared by the ceramic method and annealed at 1450 °C and by the coprecipitation method and annealed at 900, 800, and 700 °C. Dotted lines mark peak positions. **(d)** Rietveld refinement of the diffraction pattern from the material prepared by the coprecipitation method and annealed at 700 °C. The pattern was fit to a $(Ca_{0.25}Zr_{0.25}Ti_{0.5})O_{1.75}$ defect fluorite model.

Table 3-1 Results of the Rietveld refinements of the XRD patterns from the $CaZrTi_2O_7$ materials prepared by the coprecipitation (P) and sol-gel (S) methods and annealed at high and low temperatures. Oxygen positional parameters were not refined.

		Reference[134]	P-1300°C	P-900°C	S-1400°C	S-900°C
a (Å)		12.4458(7)	12.4531(2)	12.508(1)	12.4462(1)	12.510(1)
b (Å)		7.2734(4)	7.2755(1)	7.2294(8)	7.27174(8)	7.2314(7)
c (Å)		11.3942(9)	11.3814(2)	11.4064(9)	11.3813(8)	11.3987(7)
β (°)		100.533(7)	100.570(1)	100.69(1)	100.5587(8)	100.669(9)
B_{OVL}		-	0.54(3)	1.21(5)	0.27(3)	0.81(4)
Cell Volume (Å^3)		1014.1	1013.7	1013.5	1012.6	1012.0
	x	0.373(1)	0.3727(5)	0.377(1)	0.3725(5)	0.384(1)
Ca1 8f	**y**	0.123(2)	0.127(1)	0.097(3)	0.125(1)	0.136(2)
	z	0.4949(8)	0.4979(4)	0.503(1)	0.4967(4)	0.505(1)
	x	0.1222(5)	0.1236(2)	0.1288(6)	0.1238(2)	0.1314(7)
Zr1 8f	**y**	0.1222(9)	0.1247(5)	0.108(1)	0.1239(5)	0.113(1)
	z	0.9744(5)	0.9748(2)	0.9900(7)	0.9749(2)	0.9894(5)
	x	0.2497(9)	0.2525(5)	0.244(1)	0.2505(5)	0.247(1)
Ti1 8f	**y**	0.122(2)	0.126(1)	0.138(3)	0.124(1)	0.138(2)
	z	0.7467(8)	0.7451(4)	0.741(1)	0.7436(4)	0.7437(8)
	x	0.474(2)	0.4721(8)	0.517(4)	0.4720(9)	0.492(4)
Ti2 8f	**y**	0.056(2)	0.0573(9)	0.097(3)	0.0500(9)	0.095(3)
	z	0.250(3)	0.249(1)	0.275(2)	0.256(1)	0.222(2)
Ti3 4e	**y**	0.127(2)	0.125(1)	0.124(3)	0.126(1)	0.114(3)
R_{exp}		-	4.44	4.33	4.69	4.38
R_p		-	4.64	6.47	4.87	5.64
R_{wp}		-	6.04	8.80	6.32	7.51
χ^2		-	1.85	4.12	1.82	2.94

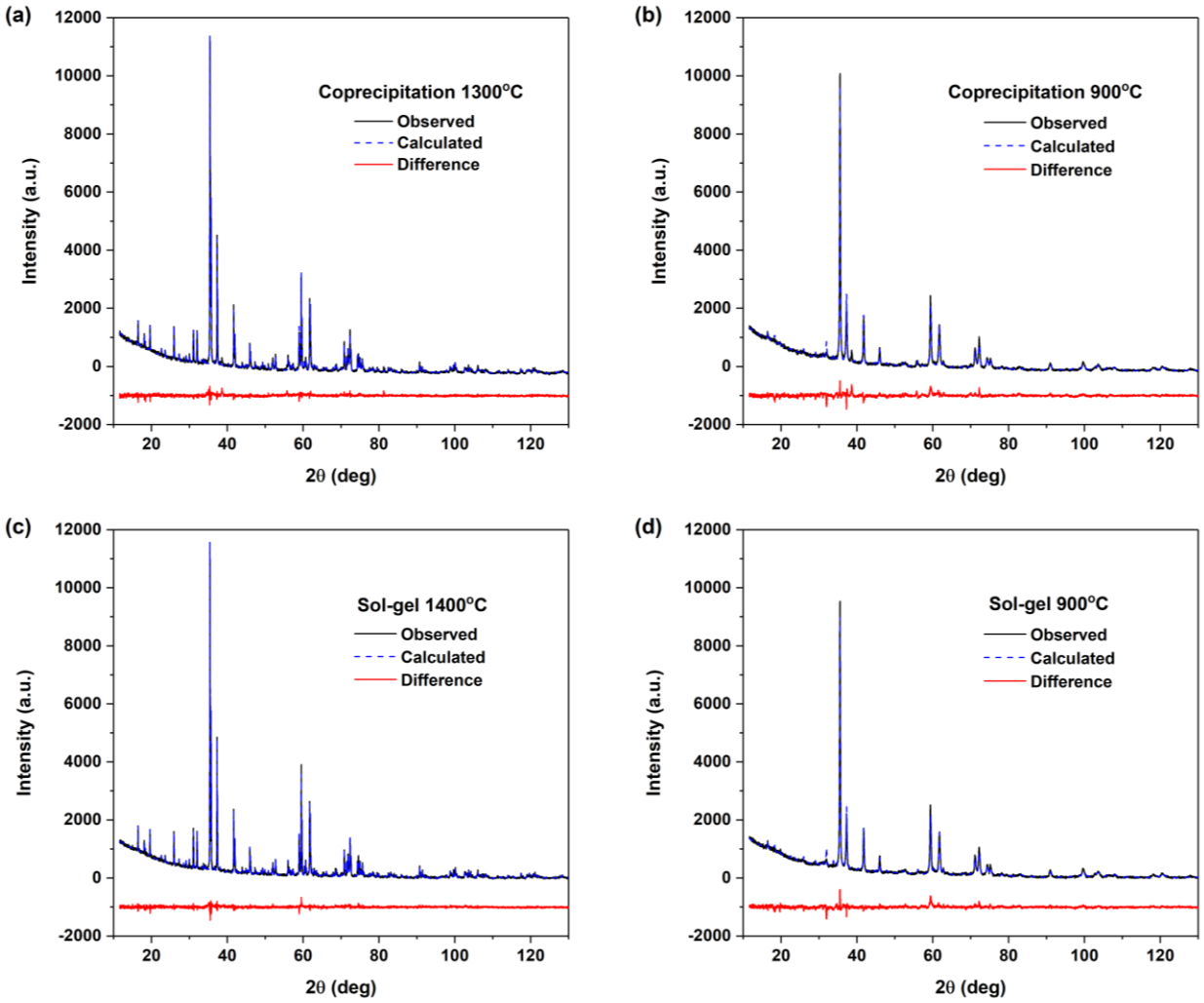

Figure 3-2 Rietveld refined powder XRD patterns from the $CaZrTi_2O_7$ materials prepared by the coprecipitation method and annealed at **(a)** 1300 °C and **(b)** 900 °C, and prepared by the sol-gel method and annealed at **(c)** 1400 °C and **(d)** 900 °C.

3.3.2 SEM

SEM images were obtained to compare the particle sizes of materials prepared by the three synthesis methods at high and low annealing temperatures. **Figure 3-3** shows the SEM images from the powdered materials prepared by the ceramic method and annealed at 1400 °C and prepared by the coprecipitation and sol-gel methods and annealed at 900 °C. The particle size of the material is significantly larger (~10-20 μm) when prepared by the ceramic method and annealed at high temperature than the materials prepared by either the coprecipitation or sol-gel methods (~200-500 nm) and annealed at low temperature (i.e., 900 °C). The materials prepared by the coprecipitation and sol-gel methods followed by annealing at 900 °C were similar in particle size and distribution (**Figure 3-3(bc)**). This trend in particle size is also reflected in the crystallite size calculated by the Scherrer equation for these materials. The crystallite sizes of the materials prepared by the coprecipitation method were calculated to be 290±30 and 70±20 nm for materials annealed at 1300 and 900 °C, respectively. Similarly, the crystallite sizes of the materials prepared by the sol-gel method were calculated to be 600±100 and 70±10 nm for materials annealed at 1400 and 900 °C, respectively.

3.3.3 Zr K-edge XANES

Zr K-edge XANES spectra were collected from the zirconolite materials made by the ceramic method (annealed at 1450 °C), the coprecipitation method, and the sol-gel method, and are presented in **Figure 3-4(ab)**. No differences in the line shape of the spectra from any of the materials prepared by the coprecipitation or sol-gel methods and annealed at 900 or 1400 °C were observed when compared to the spectrum from the material prepared by the ceramic method. The spectra from both materials annealed at 800 °C show very small changes in the line shape of the spectra. The XRD patterns from the materials prepared by the coprecipitation and sol-gel methods annealed at 800 °C showed that Zr is present in both $CaZrTi_2O_7$ and a defect fluorite-type phase. Zr is 7-coordinate in zirconolite and 7-coordinate in defect fluorite. The rounded feature above the absorption edge is typical of either 7-coordinate Zr or 8-coordinate Zr with longer than average bond lengths, such as in zirconolite (7-coordinate; average bond length = 2.166 Å) or zirconium sulphate tetrahydrate (8-coordinate; average bond length = 2.180 Å).[135]

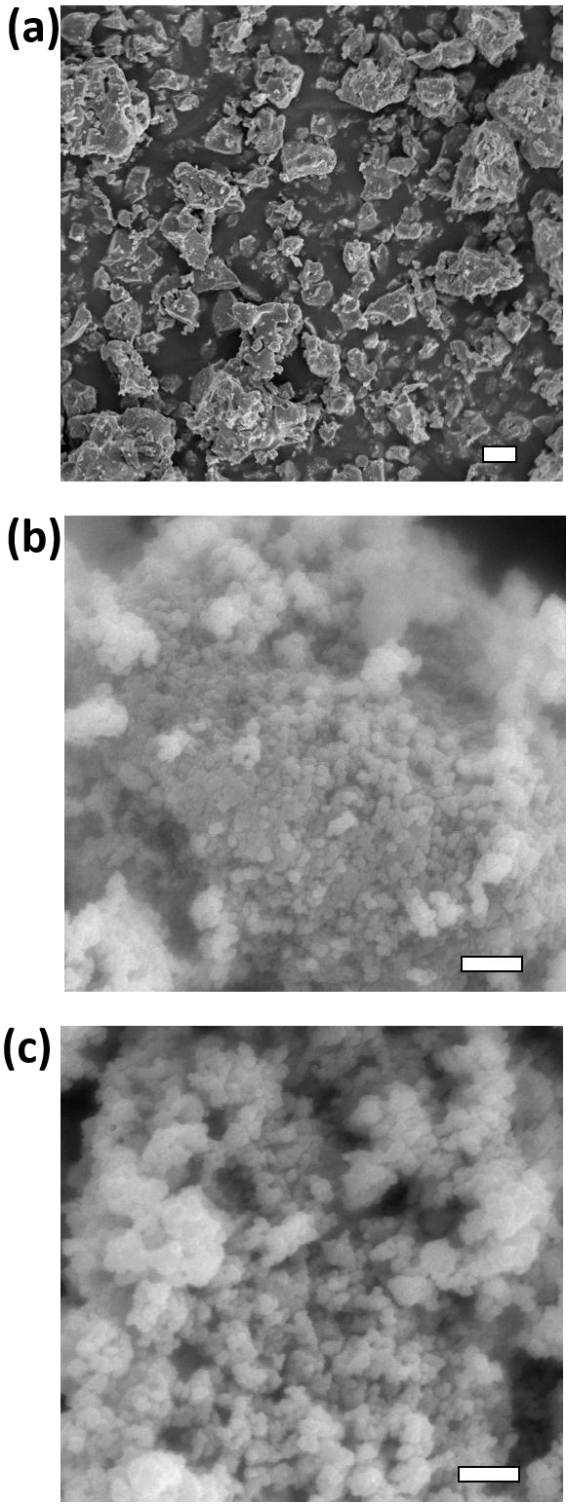

Figure 3-3 SEM images of $CaZrTi_2O_7$ materials **(a)** prepared by the ceramic method and annealed at 1400 °C (the scale bar is 10 μm); **(b)** prepared by the coprecipitation method and annealed at 900 °C (the scale bar is 1 μm); **(c)** prepared by the sol-gel method and annealed at 900 °C (the scale bar is 1 μm).

This feature can be split into two peaks if Zr is octahedrally coordinated, as in perovskite, or if the environment is 8-coordinate but highly distorted, as in zircon, as shown in **Figure 3-4(c)**.[135] The observed changes are very small, likely due to the similarity in the local environment of Zr in zirconolite and defect fluorite. Additionally, the energy resolution of XANES measurements at the Zr K-edge is ~2.5 eV, which makes reliably identifying small changes in these spectra difficult.[13,68]

3.3.4 Ti K-edge XANES

Ti K-edge XANES spectra were collected from the zirconolite materials made by the ceramic method (annealed at 1450 °C), the coprecipitation method, and the sol-gel method. These spectra are presented in **Figure 3-5(ab)**. The line shapes of the spectra from the materials prepared by the coprecipitation and sol-gel methods annealed at 1400, 1300 °C, and 900 °C are identical to the line shape of the spectrum from the material prepared by the ceramic method and annealed at 1450 °C. The spectra from both the coprecipitation and sol-gel materials annealed at 800 °C show a small change in the main edge feature (C). **Figure 3-5(c)** shows the spectra from the material prepared by the ceramic method and annealed at 1450 °C and the material prepared by the coprecipitation method and annealed at 800 °C compared to reference spectra from materials with different Ti coordination numbers. The local environment of Ti in zirconolite is a mixture of 5- and 6-coordinate. An increase in the intensity of the pre-edge peak was not observed, which would indicate that there was not an increase in the amount of 4- or 5-coordinate Ti in the materials prepared at 800 °C. The narrowing of the main edge feature appears to mimic the shape of the $Gd_2Ti_2O_7$ pyrochlore spectrum, indicating that the amount of 6- or (potentially) 7-coordinate Ti relative to 5-coordinate is higher in the material prepared at 800 °C than at higher temperatures. This is supported by the presence of peaks corresponding to a defect fluorite-type phase in the diffraction pattern of the material annealed at 800 °C.

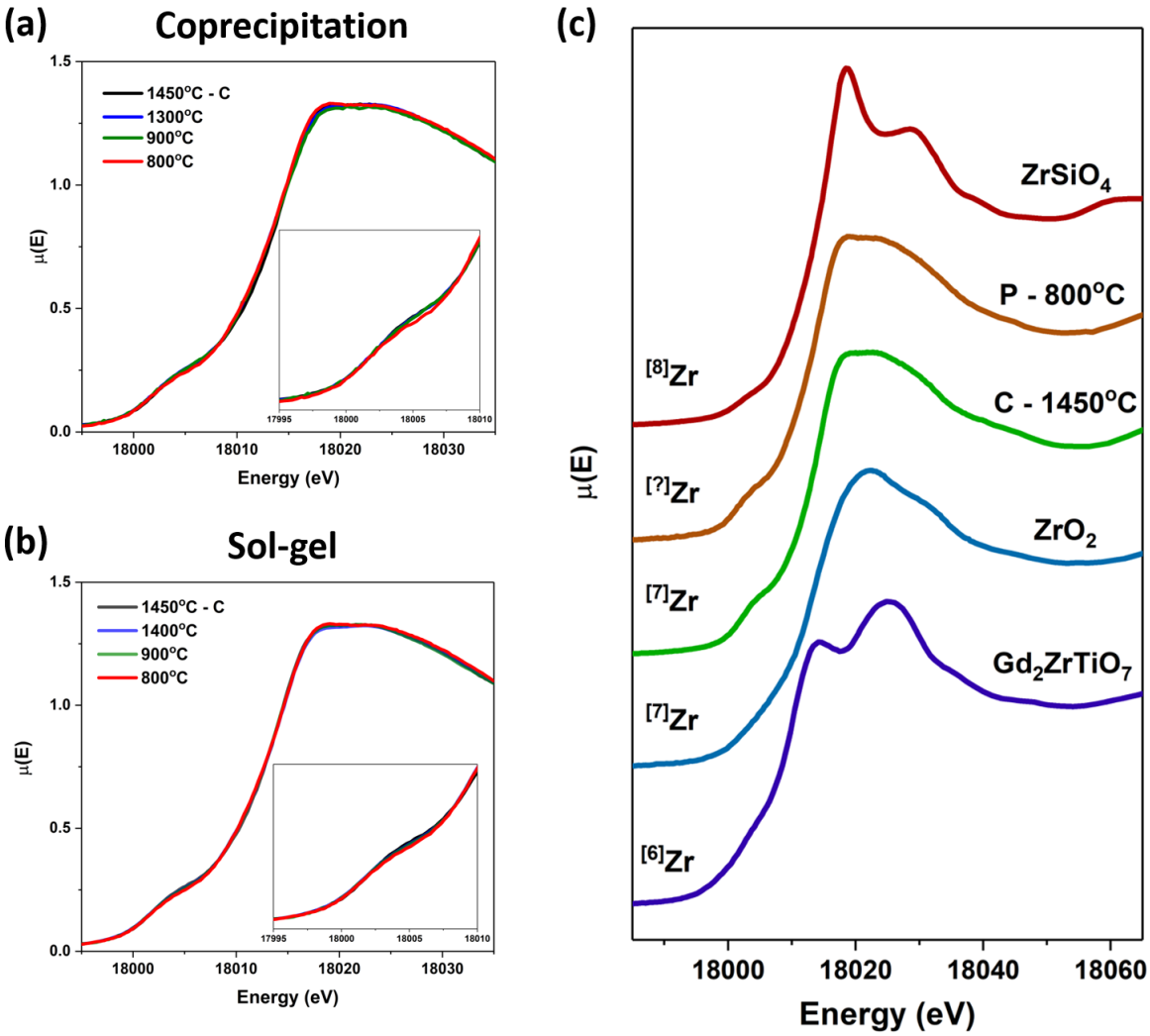

Figure 3-4 Zr K-edge XANES spectra from $CaZrTi_2O_7$ materials prepared by **(a)** the coprecipitation method and **(b)** by the sol-gel method, compared to the spectrum from the material prepared by the ceramic method (black spectrum); **(c)** Zr K-edge spectra from reference compounds with different Zr coordination numbers.

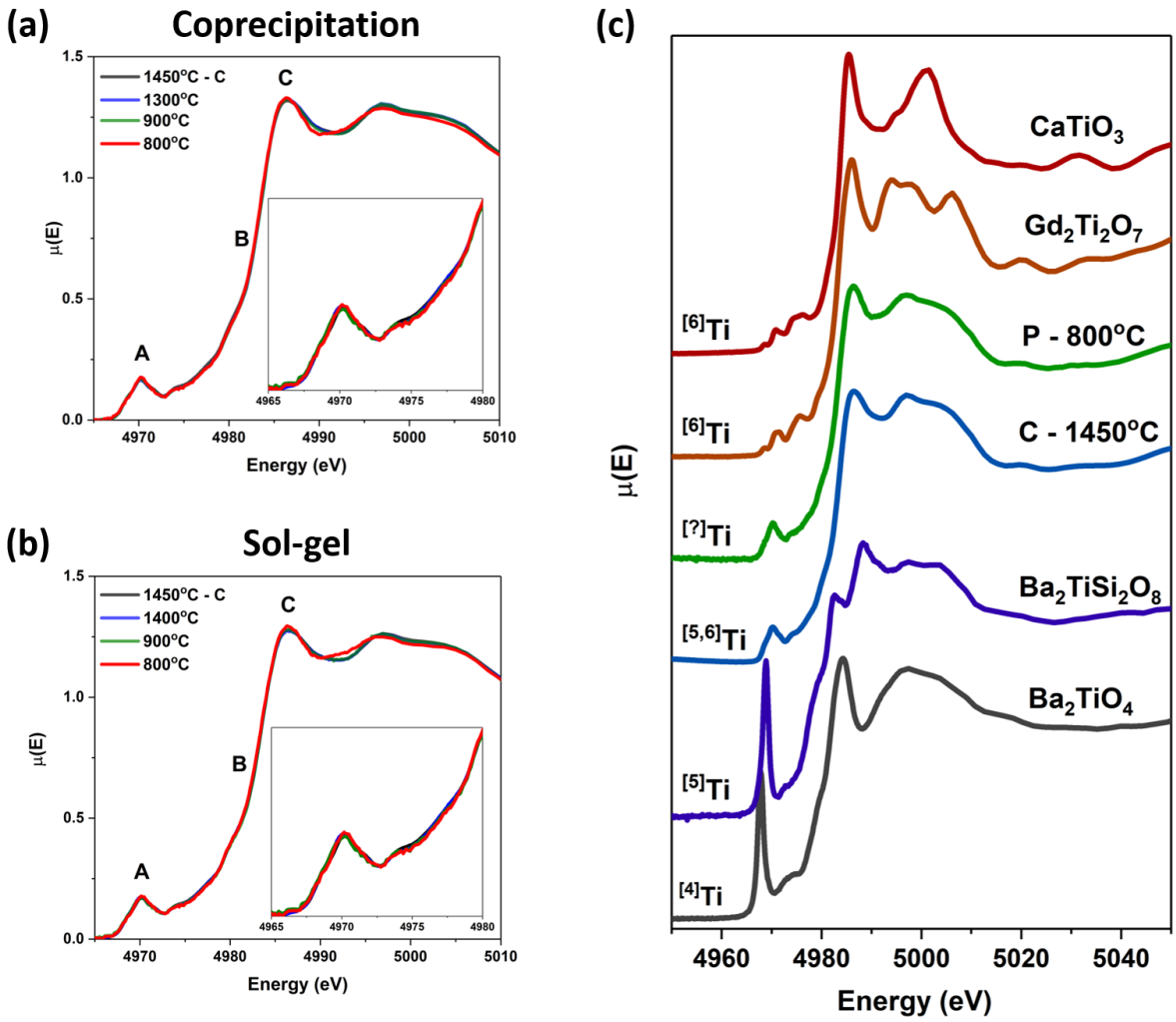

Figure 3-5 Ti K-edge XANES spectra from the $CaZrTi_2O_7$ materials prepared by **(a)** the coprecipitation method and **(b)** by the sol-gel method, compared to the spectrum from the material prepared by the ceramic method (black spectrum). The pre-edge (A) and main edge (B, C) regions are indicated. **(c)** Ti K-edge XANES spectra from the $CaZrTi_2O_7$ materials prepared by the ceramic (C) and coprecipitation (P) methods annealed at 1450 and 800 °C, respectively, and reference compounds with different Ti coordination numbers.

3.4 Conclusions

Zirconolite-type oxides ($CaZrTi_2O_7$) have been successfully synthesized using a coprecipitation and a sol-gel method with annealing temperatures ranging from 900 to 1400 °C. Materials prepared using these methods followed by annealing at 800 °C contained a $(Ca_{0.25}Zr_{0.25}Ti_{0.5})O_{1.75}$ defect fluorite-type material. The diffraction patterns showed that 900 °C is the lowest temperature at which zirconolite can be formed phase-pure by these methods. Rietveld refinement of XRD patterns from zirconolite materials prepared by the coprecipitation and sol-gel methods showed very small structural changes when the material was annealed at high or low temperatures. Examination of the Zr K-edge XANES spectra from these materials showed a very small change in the line shape of the spectra from materials prepared at 800 °C due to the similarity in the local environment of Zr in zirconolite and defect fluorite. These differences may be more apparent in Zr $L_{2,3}$-edge XANES spectra due to increased energy resolution. A small change in the shape of the main edge feature of the Ti K-edge XANES spectra was observed for the materials annealed at 800 °C which can be attributed to the presence of Ti in a defect fluorite-type material. It has been shown in this study that zirconolite-type oxides can be synthesized at temperatures as low as 900 °C using either a coprecipitation or sol-gel method with very little change in the short- or long-range structure of the material. This work contributes towards the development of economically viable processes for the synthesis of nuclear wasteforms.

Chapter 4

Effect of synthesis method on the radiation resistance of $Gd_2Ti_2O_7$ pyrochlore-type and $CaZrTi_2O_7$ zirconolite-type materials*

4.1 Introduction

The previous two chapters described the synthesis of $RE_2Ti_2O_7$ (RE = Sm, Gd, Yb) pyrochlore-type oxides by ceramic and coprecipitation methods, and $CaZrTi_2O_7$ zirconolite-type oxides by ceramic, coprecipitation, and sol-gel methods. These materials have been investigated for many years for nuclear wasteform applications due to their resistance to radiation-induced structural damage and resistance to leaching in water. It has been shown above that these materials can be prepared at significantly lower temperatures using solution-based synthesis methods when compared to the classic ceramic synthesis, with only minor changes in the structure being observed. However, it has yet to be demonstrated that the materials prepared by these solutions-based methods retain their radiation resistance properties, which are essential for nuclear wasteforms to limit the release of radionuclides to the environment.

Pyrochlore- and zirconolite-type oxides have been proposed for the storage of actinide elements (commonly present in HLW) which typically undergo α-decay and emit an α-particle and a heavy, high energy recoil nucleus.[1,22,28,29,37,43,71,76,112] The two most common approaches to study the effect of radioactive decay within a material are direct incorporation of radionuclides into the material causing *in situ* radiation damage (self-radiation) and external irradiation of the material using an ion accelerator (ion implantation).[21,24,37,39,58,71,112] Ion implantation is particularly useful to simulate the interactions of the daughter products with the surrounding material in

* A version of this chapter, authored by Sarah McCaugherty and Andrew P. Grosvenor, has been submitted for publication. The manuscript has been reformatted for inclusion in this thesis. The Introduction section has been altered to avoid excessive repetition of Chapter 1 content.

reasonable time scales (minutes to hours) rather than geologic time scales (thousands of years).[22,24,37,39,41,71,113]

In this work, $RE_2Ti_2O_7$ (RE = Sm, Gd, Yb) pyrochlore-type materials were synthesized by a sol-gel method and characterized by powder XRD, SEM, and Ti K-edge XANES. These results were compared to those from the same materials prepared by ceramic and coprecipitation methods presented in **Chapter 2**. The effect of annealing temperature on the structures of these pyrochlore-type materials prepared by sol-gel methods has not previously been reported. Pelleted $Gd_2Ti_2O_7$ and $CaZrTi_2O_7$ materials prepared by ceramic, coprecipitation, and sol-gel methods were implanted using a high energy beam of Au^- ions to simulate radiation damage caused by the decay of actinide radionuclides. The damaged surface region was probed by Ti K-edge glancing-angle (GA) XANES to evaluate the effect of the ion implantation on the local structure of the materials. GA-XANES is a surface-sensitive characterization technique wherein the incident angle of the X-rays is very small and can be adjusted to probe different regions in the material. The glancing-angle is set to be just above the critical angle, below which total external reflection occurs.

4.2 Experimental

4.2.1 Synthesis

Pyrochlore- ($RE_2Ti_2O_7$; RE = Sm, Gd, Yb) and zirconolite- ($CaZrTi_2O_7$) type materials were synthesized by ceramic, coprecipitation, and sol-gel methods. The ceramic and coprecipitation syntheses of the pyrochlore materials are described in **Section 2.2.1**. The sol-gel method used to prepare the pyrochlore-type materials involved the dissolution of rare earth nitrates and titanium tert-butoxide in ethanol with stirring until gel formation. $Sm(NO_3)_3{\cdot}6H_2O$ (Alfa-Aesar, 99.9%), $Gd(NO_3)_3{\cdot}6H_2O$ (Alfa Aesar, 99.9%), or $Yb(NO_3)_3{\cdot}xH_2O$ (Alfa Aesar, 99.9%) were dissolved in 1 mL absolute ethanol per 0.25 g of expected product. Absolute ethanol was used instead of 95% ethanol to prevent hydrolysis of titanium tert-butoxide and the precipitation of TiO_2. One drop of concentrated HNO_3 acid and a stoichiometric amount of $Ti[OC(CH_3)_3]_4$ was then added to the solution. A glassy, colourless gel was obtained after less than five minutes of stirring in a water bath at 40 °C. The gel was then dried at 100 °C overnight to yield a white powder, which was then pressed into pellets uniaxially at 6 MPa. Pelleted samples were annealed at temperatures ranging

from 700 to 1400 °C for 6 (1400, 1200 °C), 9 (1000, 800 °C), or 12 days (700 °C), followed by quench cooling in air. The synthesis of the zirconolite-type materials was described in **Section 3.2.1**.

4.2.2 Powder XRD

Diffraction patterns were collected from the $RE_2Ti_2O_7$ (RE = Sm, Gd, Yb) pyrochlore-type materials prepared by the sol-gel method using a PANalytical Empyrean X-ray diffractometer with a Co $K\alpha_{1,2}$ X-ray source operating at 40 kV and 45 mA and were collected in the 2θ range of 10-80° with a step size of 0.017°. XRD patterns from $RE_2Ti_2O_7$ (RE = Sm, Gd, Yb) pyrochlore-type oxides prepared by ceramic and coprecipitation methods were previously collected and are presented in **Section 2.3.1**. XRD patterns from $CaZrTi_2O_7$ zirconolite-type materials prepared by ceramic, coprecipitation, and sol-gel methods were also previously collected and are presented in **Section 3.3.2**. The average crystallite sizes of the pyrochlore materials prepared by the sol-gel method were calculated using the Scherrer equation (Equation 1-11). The line broadening from the diffractometer was determined from a polycrystalline Si reference disk and subtracted from the experimental FWHM to give the corrected line broadening value (*B*). The crystallite size was calculated from the four highest intensity diffraction peaks and the error was determined from the standard deviation of these calculated values.

4.2.3 Ion implantation

Pyrochlore- and zirconolite-type materials were implanted with a high energy (2 MeV) beam of Au^- ions to a dose of 5.0 x 10^{14} ions/cm^2 using the 1.7 MeV Tandetron accelerator located at Interface Science Western (ISW), University of Western Ontario. The materials listed in **Table 4-1** were pelleted uniaxially at 8 MPa before the final three days of annealing, followed by ion implantation of one flat surface of the pellet. The ion beam was aligned normal to the surface of the pellet.

The ion implantation depth and the number of vacancies per Au^- ion were calculated for both materials using the Stopping Range of Ions in Matter (SRIM-2013) software package and are presented in **Figure 4-1**.[117] The simulations were performed using 5000 Au^- ions with an ion beam energy of 2 MeV. The target displacement energies (the energy required to permanently displace

an atom from its lattice site to a defect position) were assumed to be 25 eV for Ca/Ti/Zr and 28 eV for O.[117,136] The density of $Gd_2Ti_2O_7$ and $CaZrTi_2O_7$ used in the calculations were 6.57 and 4.44 g/cm^3, respectively. The X-ray attenuation depth in the materials was calculated at the Ti K-edge absorption energy using an internet-based program provided by Lawrence Berkeley National Laboratory.[137] This program utilizes the Beer-Lambert law to calculate the depth to which X-rays of a given energy will penetrate a material as a function of angle, relative to the surface of the material. Two angles were chosen to be studied for each material. The first angle corresponds to a depth of ~100 nm within the material which is likely to be the most damaged region. The second angle was chosen to probe the entire region in which Au^- ions were calculated to be implanted.

Table 4-1 Synthesis conditions of ion implanted materials and the glancing angles studied by GA-XANES.

Material	Synthesis Method	Annealing Temperature	Annealing Time	Glancing Angles/Depths Studied
$Gd_2Ti_2O_7$	Ceramic	1400 °C	12 days	1.1°/100 nm 4.5°/450 nm
	Coprecipitation	800 °C	12 days	
	Sol-gel	800 °C	15 days	
$CaZrTi_2O_7$	Ceramic	1400 °C	12 days	0.8°/100 nm 3.1°/500 nm
	Coprecipitation	1200 °C	9 days	
	Sol-gel	1200 °C	9 days	

4.2.4 Ti K-edge XANES and GA-XANES

Ti K-edge XANES spectra were collected from the pyrochlore materials prepared by the sol-gel method using the Sector 20BM beamline located at the APS.[131] Ti K-edge XANES spectra from $RE_2Ti_2O_7$ (RE = Sm, Gd, Yb) pyrochlore-type oxides prepared by ceramic and coprecipitation methods were previously collected and are presented in **Section 2.3.3**. Samples were finely ground, spread onto Kapton tape, and layered to maximize absorption. XANES spectra were collected in partial fluorescence mode using a 13-element Ge detector and transmission mode with a mixture of He and N_2 (70:30) gases in the incident ion chamber and 100 % N_2 gas in the transmission and reference chambers. A Si (111) double crystal monochromator was used, providing a spectral resolution of 0.7 eV at 4966 eV.[131] Spectra from Ti metal foil (E_0 = 4966 eV) were collected

concurrently in transmission mode and used for calibration. XANES spectra were collected using a step size of 0.15 eV through the absorption edge.

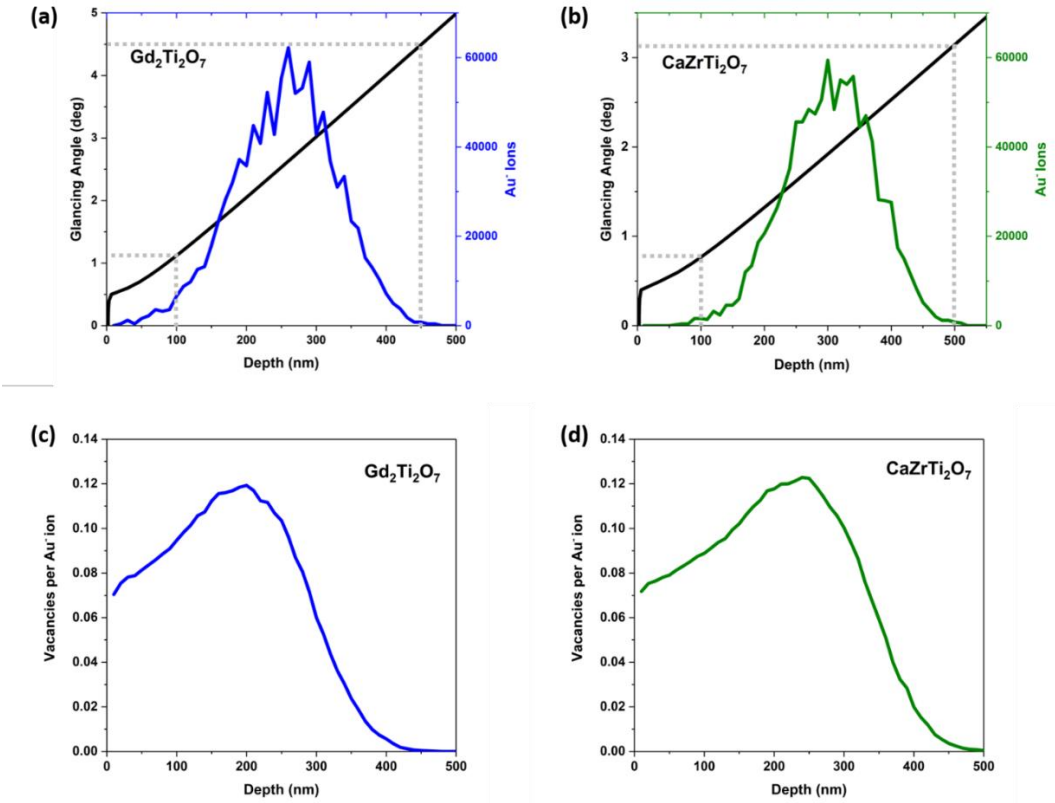

Figure 4-1 Ion implantation depth and X-ray attenuation depth for **(a)** $Gd_2Ti_2O_7$ and **(b)** $CaZrTi_2O_7$ materials; Number of vacancies produced per Au^- ion in **(c)** $Gd_2Ti_2O_7$ and **(d)** $CaZrTi_2O_7$ materials. Dotted lines mark angles/penetration depths studied by Ti K-edge GA-XANES.

Ti K-edge GA-XANES spectra were collected from ion-implanted materials using the Sector 20BM beamline in partial fluorescence mode.[131] The ion-implanted pellets were mounted on carbon tape and attached to a motor driven Huber goniometer which was used to adjust the glancing angle. The X-ray beam was vertically focused with a height of 2 mm and a beam width of 50 μm. The 0° angle was calibrated by adjusting the angle of the sample to achieve maximum transmission. The glancing angle was set to the desired value with a precision of 0.1° to probe different depths of the ion implanted material. All XANES spectra presented here were calibrated, normalized, and analyzed using the Athena software program.[132]

4.2.5 SEM

Scanning electron microscopy (SEM) was used to study the particle size of as-synthesized $Gd_2Ti_2O_7$ materials prepared by the sol-gel method and annealed at 800 °C. SEM images were previously collected from $Gd_2Ti_2O_7$ materials prepared by the coprecipitation method and annealed at 1400, 800, and 700 °C and are presented in **Section 2.3.2**. Images were also collected from the ion-implanted surface of $Gd_2Ti_2O_7$ pellets prepared by the ceramic method (annealed at 1400 °C) and the sol-gel method (annealed at 800 °C) to compare the surface morphologies. Imaging was performed using a JEOL 840A scanning electron microscope. Samples were mounted on double-sided carbon tape and sputter coated with approximately 200 Å of gold prior to loading them into the SEM. Images were acquired at 15 kV under a working distance of 15 mm and were analyzed using the Gellar Analytical's dPict image acquisition software program.

4.3 Results and Discussion

4.3.1 XRD Analysis of $RE_2Ti_2O_7$ Prepared by the Sol-gel Method

The powder XRD patterns from $RE_2Ti_2O_7$ (RE = Sm, Gd, Yb) materials prepared by the sol-gel method are presented in **Figure 4-2**. The diffraction patterns from the same materials prepared by the ceramic method and annealed at 1400 °C are shown for comparison. The diffraction patterns for all compositions show the formation of $RE_2Ti_2O_7$ with no crystalline impurities after annealing at temperatures ranging from 1400 to 700 °C. These results are very similar to those obtained for the same materials prepared by the coprecipitation method (see **Section 2.3.1**). Broadening of the diffraction peaks was observed from the samples annealed at lower temperatures. This is likely due to a decrease in the crystallite size of the materials.

4.3.2 Crystallite and Particle Size Analysis of $RE_2Ti_2O_7$ Prepared by the Sol-gel Method

The crystallite sizes of the $RE_2Ti_2O_7$ (RE = Sm, Gd, Yb) materials prepared by the sol-gel method after annealing at various temperatures are calculated using the Scherrer equation are shown in **Figure 4-3** and compared to the results from the same materials prepared by the coprecipitation method (previously discussed in **Section 2.3.2**). The crystallite size of the materials increased with increasing annealing temperature. This is typical for solid-state reactions as the diffusion path length increases as the crystallites grow, increasing the energy required for further growth. The large crystallite size after annealing at high-temperature results in decreased reliability of the Scherrer equation, and thus larger error bars. The materials that were annealed at low-temperature show very narrow ranges of calculated crystallite size. Similar results were obtained regardless of which method was used to prepare the materials (coprecipitation vs. sol-gel) for each annealing temperature.

An SEM image from the $Gd_2Ti_2O_7$ pyrochlore material prepared by the sol-gel method and annealed at 800 °C is shown in **Figure 4-4**. The average particle size of this material is approximately the same (300-500 nm) as that for the $Gd_2Ti_2O_7$ pyrochlore material prepared by the coprecipitation method and annealed at the same temperature (see **Figure 2-5**). The similarity between the observed particle size and the calculated crystallite size of this material indicates that the particle growth occurs at nearly the same rate when either method is used. Fundamentally, both synthesis methods should result in a precursor powder which is homogeneously mixed on the atomic scale, resulting in similar rates of crystallite and particle growth upon annealing.

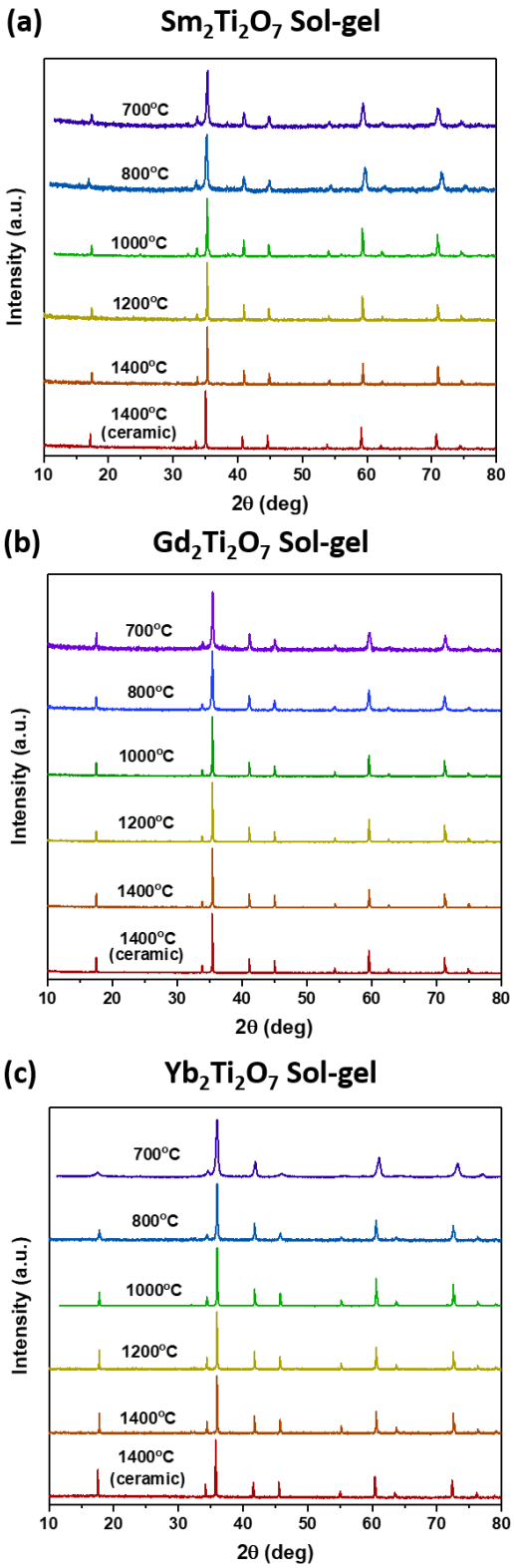

Figure 4-2 Powder XRD patterns from **(a)** $Sm_2Ti_2O_7$, **(b)** $Gd_2Ti_2O_7$, and **(c)** Yb_2Ti2O_7 prepared by the sol-gel method. The patterns are compared to the same material prepared by the ceramic method and annealed at 1400 °C.

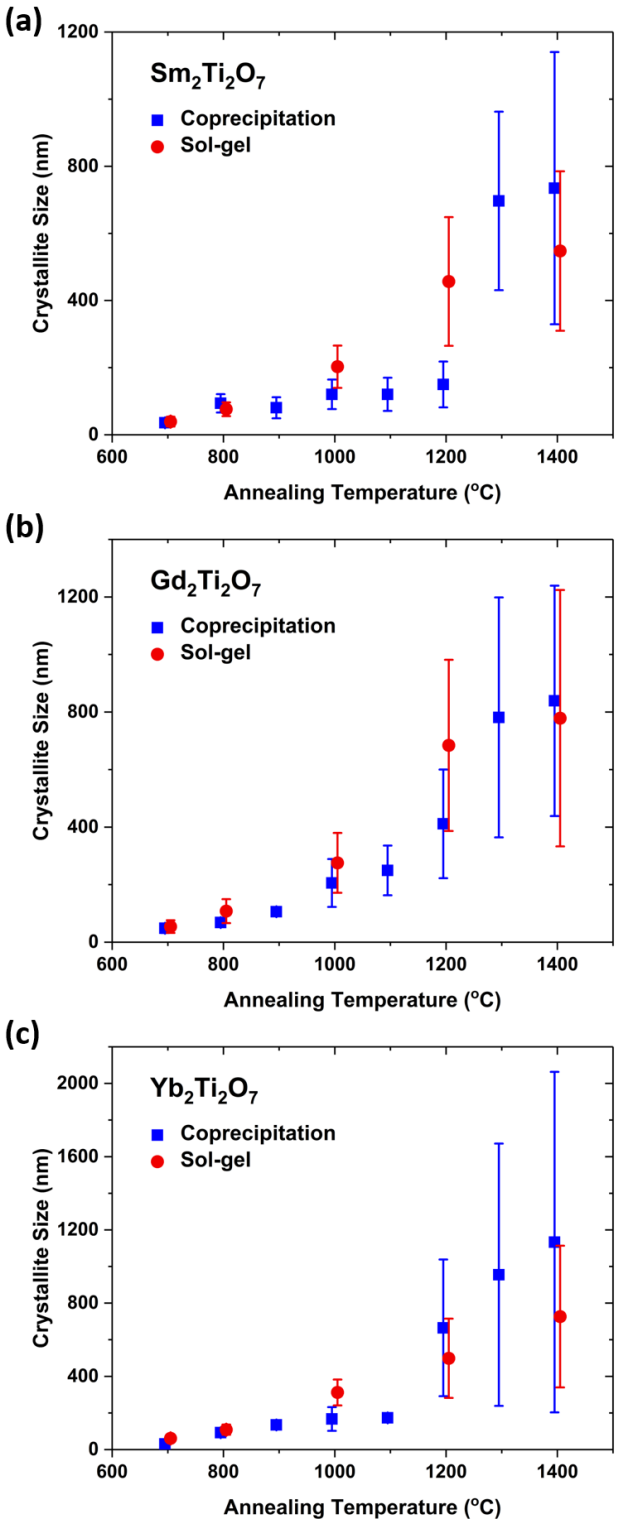

Figure 4-3 Crystallite sizes calculated by the Scherrer equation from the powder XRD patterns from **(a)** $Sm_2Ti_2O_7$, **(b)** $Gd_2Ti_2O_7$, and **(c)** $Yb_2Ti_2O_7$ materials prepared by the coprecipitation and sol-gel methods. Error bars correspond to the standard deviation of the calculated values.

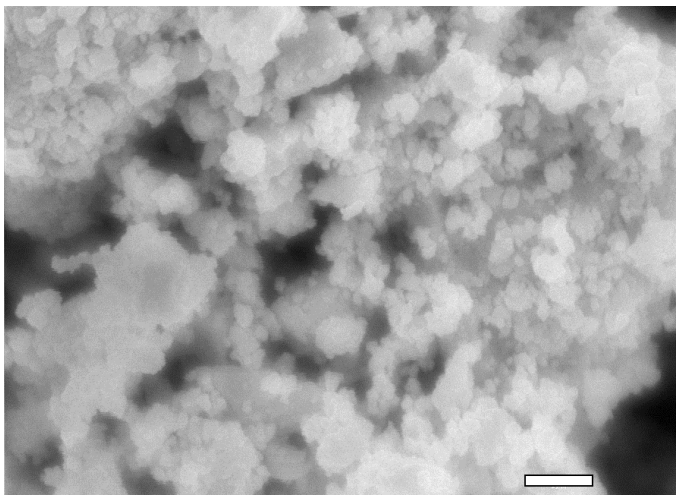

Figure 4-4 SEM image of the $Gd_2Ti_2O_7$ material prepared by the sol-gel method and annealed at 800 °C viewed at 20,000x magnification. The scale bar is 1 μm.

4.3.3 Ti K-edge XANES Spectra from $Gd_2Ti_2O_7$ Prepared by the Sol-gel Method

Ti K-edge XANES spectra were collected from $Gd_2Ti_2O_7$ materials prepared by the sol-gel method and annealed at 1400, 800, and 700 °C. These spectra are presented in **Figure 4-3(a)** and are compared to the spectra from the $Gd_2Ti_2O_7$ materials prepared by coprecipitation and annealed at the same temperatures (**Figure 4-3(b)**, previously shown in **Figure 2-5(b)**). No changes in the line shape of the spectra from the sol-gel samples annealed at 1400 and 800 °C were observed when compared to the spectrum from the material made by the ceramic method and annealed at 1400 °C. The spectrum from the material annealed at 700 °C show the same increase in the pre-edge region intensity, decrease in the main edge intensity, and broadening of the main edge features as the spectrum from the material prepared by coprecipitation and annealed at the same temperature. As was described in detail in **Section 2.3.3**, these changes in the spectral features result from the presence of Ti in an amorphous phase, wherein Ti is known to be 4- or 5-coordinate.

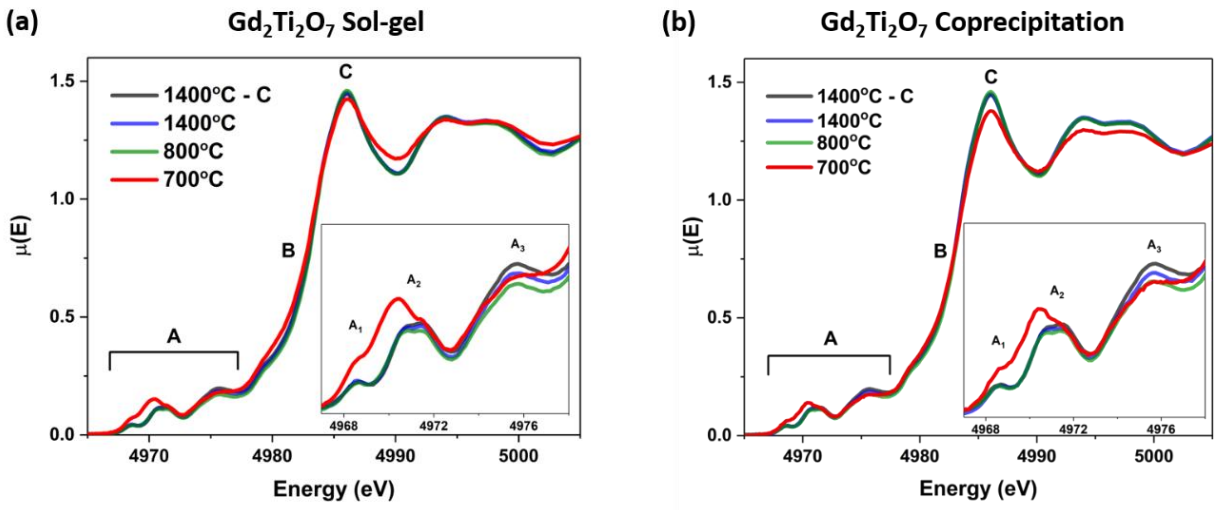

Figure 4-5 Ti K-edge XANES spectra from $Gd_2Ti_2O_7$ prepared by the **(a)** sol-gel and **(b)** coprecipitation method and annealed at temperatures ranging from 700 to 1400 °C. The black spectra are from materials prepared by the ceramic method and annealed at 1400 °C. The features A_1, A_2, and A_3 correspond to $1s \rightarrow 3d\ t_{2g}$, $1s \rightarrow 3d\ e_g^*$, and intersite-hybrid excitations, respectively. Features B and C represent the main-edge region of the spectrum.

4.3.4 $Gd_2Ti_2O_7$ and $CaZrTi_2O_7$ Ti K-edge GA-XANES

Ti K-edge GA-XANES spectra were collected from ion-implanted $CaZrTi_2O_7$ and $Gd_2Ti_2O_7$ materials prepared by the ceramic, coprecipitation, and sol-gel methods to determine the effect of the synthesis method on the resistance of these materials to radiation-induced structural damage. Spectra were collected at two angles from each material, one low angle to probe the most damaged region and another higher angle to probe the entire damaged region of the material, as determined by calculations using the SRIM program. These spectra were then compared to the spectrum from the as-synthesized material to show the change in the structure of the material after ion implantation.

Zirconolite-type materials are known to be highly resistant to radiation-induced structural damage, as can be seen in **Figure 4-6**. A small decrease in the intensity of the main-edge feature and an increase in the intensity of the pre-edge feature when the spectra from the ion implanted materials are compared to the spectra from the as-synthesized materials. This can be attributed to a decrease in the coordination number of Ti in the material because of partial amorphization.[66,76] The degree of amorphization can be concluded to be very small because the change in the spectrum

after implantation is minor.[76] The spectra from the $CaZrTi_2O_7$ materials prepared by the coprecipitation and sol-gel methods overlap completely with the spectrum from the material made by the ceramic method. This indicates that preparation of $CaZrTi_2O_7$ zirconolite-type materials by solution-based synthesis methods (coprecipitation and sol-gel) does not affect the radiation resistance properties of the materials, even at lower annealing temperatures.

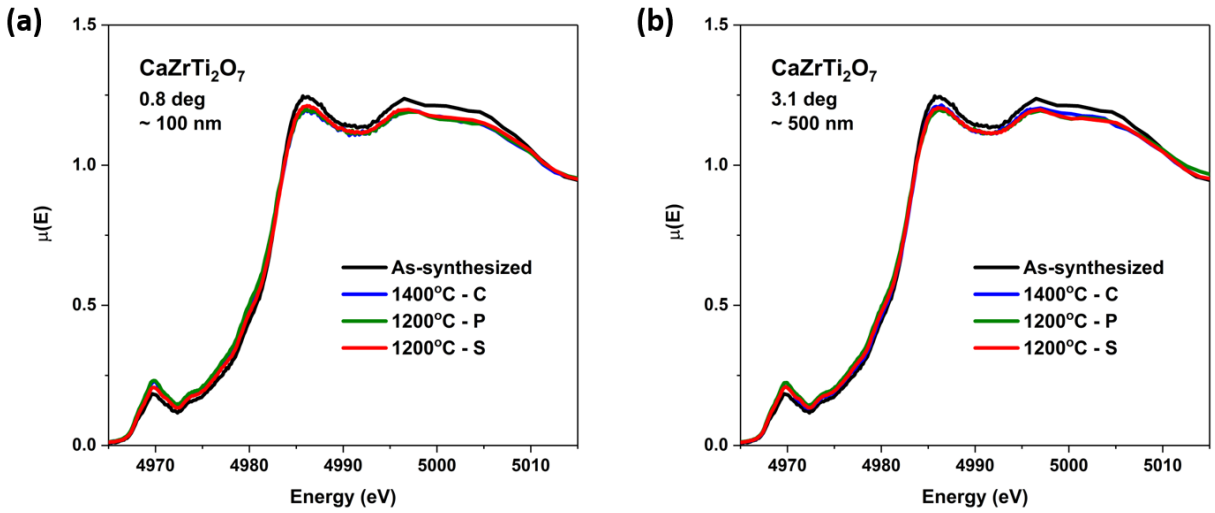

Figure 4-6 Ti K-edge GA-XANES spectra from ion-implanted $CaZrTi_2O_7$ materials prepared by the ceramic, coprecipitation, and sol-gel methods collected at **(a)** 0.8°/~100 nm and **(b)** 3.1°/~500 nm. The "As-synthesized" materials were prepared by the ceramic method and annealed at 1450 °C.

Ti K-edge GA-XANES spectra were also collected from ion implanted $Gd_2Ti_2O_7$ materials prepared by the ceramic, coprecipitation, and sol-gel methods (**Figure 4-7**). The spectra from the ion implanted materials show a decrease in the main edge intensity and an increase in the pre-edge intensity relative to the undamaged material, which is indicative of amorphization of the material. A similar observation was made when studying the zirconolite materials. However, the spectrum from the ion implanted $Gd_2Ti_2O_7$ material prepared by the sol-gel method collected at 1.1° (**Figure 4-7(a)**) shows that the material is significantly more damaged than the materials synthesized by the ceramic or coprecipitation methods. Similarly, the spectrum from the $Gd_2Ti_2O_7$ material prepared by the sol-gel method collected at 4.5° (**Figure 4-7(b)**) shows a slight decrease in the intensity of the main edge feature. The Au^- ions may be able to implant further into the material prepared by the sol-gel method if it is more porous than the materials prepared by the other two

methods, which could have caused an increase in structural damage within this region. Given that the powder XRD patterns and the Ti K-edge XANES spectra from the $Gd_2Ti_2O_7$ materials prepared by the sol-gel method showed no change in the structure of the material, this discrepancy is likely due to a bulk property of the material when prepared by this synthesis method rather than due to a change in the chemical structure of the material. SEM images were obtained from the ion-implanted $Gd_2Ti_2O_7$ pellets prepared by the ceramic and sol-gel methods to investigate the morphology of the material.

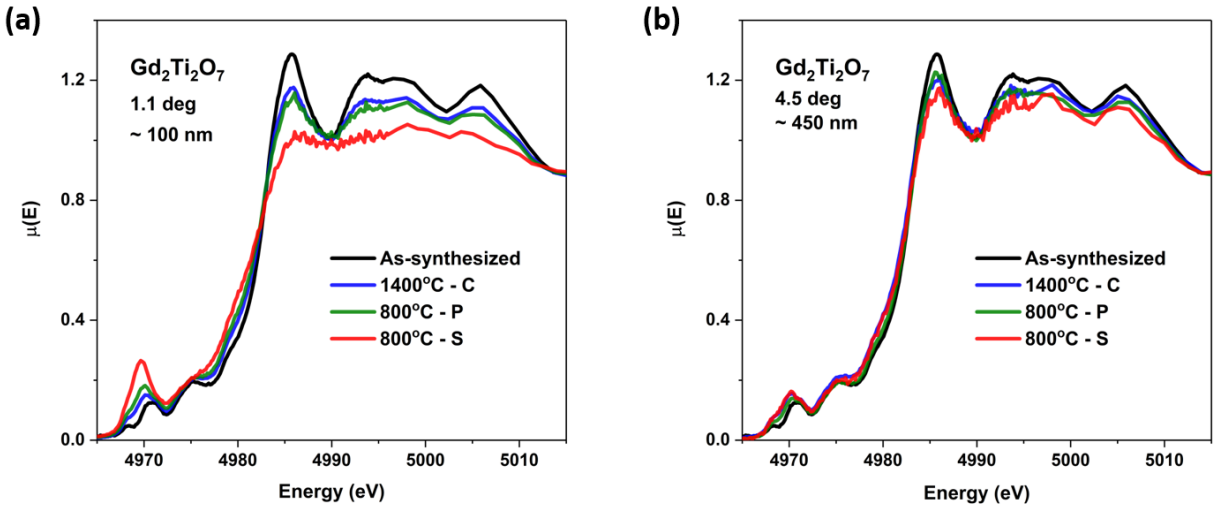

Figure 4-7 Ti K-edge GA-XANES spectra from ion-implanted $Gd_2Ti_2O_7$ materials prepared by the ceramic, coprecipitation, and sol-gel methods collected at **(a)** 1.1°/~100 nm and **(b)** 4.5°/~450 nm. The "As-synthesized" materials were prepared by the ceramic method and annealed at 1400 °C.

4.3.5 SEM from Ion-implanted $Gd_2Ti_2O_7$ Materials

The surface morphology of the ion-implanted $Gd_2Ti_2O_7$ pellets prepared by the ceramic and sol-gel methods are shown in **Figure 4-8**. The ceramic material is composed of large particles with well-defined grain boundaries. The sol-gel material is composed of small particles with ill-defined grain boundaries and contains small pores. Irradiation of crystalline materials results in the formation of interstitial and vacancy defects within the material which can eventually cause amorphization.[138,139] Grain boundaries act as sinks where these two types of defects can recombine, retaining the crystalline structure of the material.[114,115,138,139] It has been demonstrated that

nanocrystalline materials can exhibit higher radiation resistance than the corresponding large-grained materials for this reason.[115,138] However, porous nanocrystalline materials can undergo densification upon irradiation, as has been shown for several sol-gel derived ceramic thin-films.[140–143] The densification process can result in the loss of the grain structure in the surface region of the material due to amorphization. The surface of the $Gd_2Ti_2O_7$ material prepared by the sol-gel method has likely been densified by ion implantation resulting in the loss of the grain structure of the material. Additionally, the presence of a porous structure may allow deeper penetration of ions into the material, which would cause more structural damage at a given depth when compared to a nonporous material. A combination of this factor and densification may account for the increased amorphization observed in the Ti K-edge GA-XANES spectra from the material prepared by the sol-gel method.

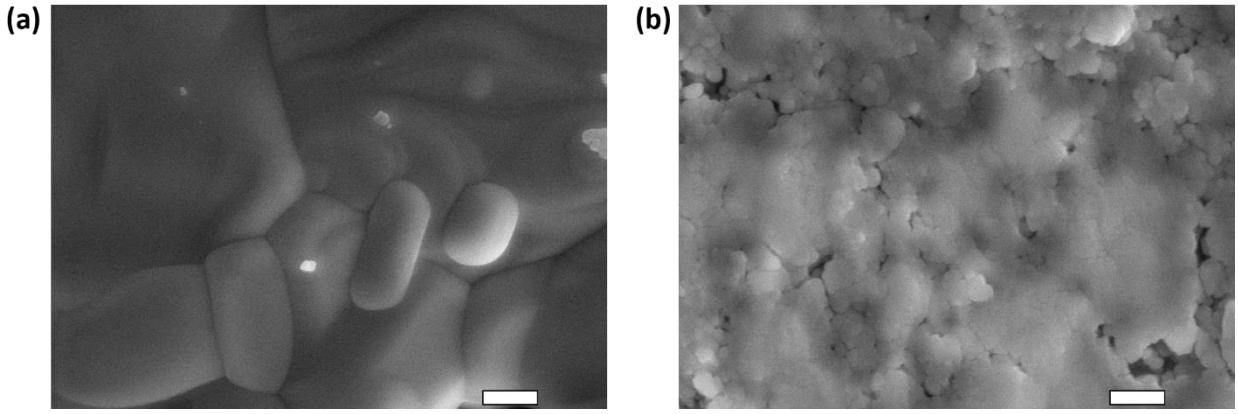

Figure 4-8 SEM images of the ion-implanted surface of the pelleted $Gd_2Ti_2O_7$ pyrochlore materials prepared by **(a)** the ceramic method (annealed at 1400 °C) and **(b)** the sol-gel method (annealed at 800 °C). The scale bars are 1 μm.

4.4 Conclusions

The radiation-resistance properties of $Gd_2Ti_2O_7$ pyrochlore-type and $CaZrTi_2O_7$ zirconolite-type materials synthesized by various methods were determined by the combination of ion implantation and GA-XANES. $RE_2Ti_2O_7$ (RE = Sm, Gd, Yb) materials were first synthesized via a simple sol-gel method and characterized by powder XRD, SEM, and Ti K-edge XANES. The annealing temperature required to form the pyrochlore structure was shown by XRD and XANES to be reduced to 800 °C using the sol-gel method, the same result that was shown in **Chapter 2** for these materials prepared using the coprecipitation method. The calculated crystallite size of these materials annealed at various temperatures was shown to be very similar to those calculated for the pyrochlore materials prepared by the coprecipitation method. Ti K-edge GA-XANES spectra from ion-implanted zirconolite materials showed a small change in the structure of these materials from irradiation. The materials prepared by the coprecipitation and sol-gel methods (annealed at 1200 °C) showed identical resistance to radiation damage as the material prepared by the ceramic method (annealed at 1400 °C). The Ti K-edge GA-XANES spectra from the $Gd_2Ti_2O_7$ pyrochlore-type materials after ion implantation also showed some amorphization of the material. This amorphization was much more significant for the material prepared by the sol-gel method, despite nanocrystalline materials generally showing higher radiation resistance. SEM images from the surface of the ion-implanted $Gd_2Ti_2O_7$ pellets showed that the sol-gel material may have experienced densification (loss of porous structure) upon irradiation, resulting in the loss of the grain structure in the surface region of the material which increased the amorphization of this region. Given that the GA-XANES spectrum from the coprecipitation pyrochlore material mostly overlapped the spectrum from the high-temperature ceramic material, it can be concluded that these two materials demonstrate similar radiation resistance. If the sol-gel method was revised to reduce the porosity of the resulting material, it seems likely that it too would show similar radiation resistance. Thus, it can be concluded that $CaZrTi_2O_7$ zirconolite-type materials and $Gd_2Ti_2O_7$ pyrochlore-type materials prepared by solution-based methods and annealed at low temperatures are just as effective as the same materials made by the ceramic method at high temperature for applications as nuclear wasteforms.

Chapter 5

Conclusions and Future Work

Pyrochlore-type oxides have been investigated here and in other works due to their potential application as nuclear wasteforms. The work presented in **Chapter 2** showed that $RE_2Ti_2O_7$ (RE = Sm, Gd, Yb) pyrochlore-type oxides could be prepared by annealing at temperatures as low as 800 °C using a coprecipitation synthesis method. Rietveld refinement of powder diffraction patterns showed that there was no significant change in the long-range structure of the materials when prepared at high or low temperatures (1400 versus 800 °C). Ti K-edge XANES showed only a decrease in the intensity of the intersite-hybrid peak of the spectra with decreasing annealing temperature, which was attributed to a small amount of local disordering of the material when compared to the same material prepared by the ceramic method and annealed at 1400 °C. Pyrochlore-type oxides are generally prepared via ceramic (solid-state) synthesis methods. **Figure 5-1** shows the XRD patterns from $Yb_2Ti_2O_7$ materials prepared by the ceramic method (methodology described in **Section 2.2**) and annealed at various temperatures. Phase-pure pyrochlore has formed after six days of annealing at 1400, 1300, and 1200 °C. Diffraction peaks from the pyrochlore phase as well as unreacted starting materials (Yb_2O_3 and TiO_2) are present in the diffraction patterns from the materials annealed at 1100 and 800 °C. The materials annealed at these two temperatures did not fully form the pyrochlore phase even after extensive annealing. Thus, it was shown that pyrochlore-type materials can be prepared at significantly lower temperatures (up to 400 °C lower) using a solution-based synthesis method like coprecipitation. To investigate whether this result could be extended to other materials, a second ceramic material with applications in nuclear waste sequestration was chosen for additional studies.

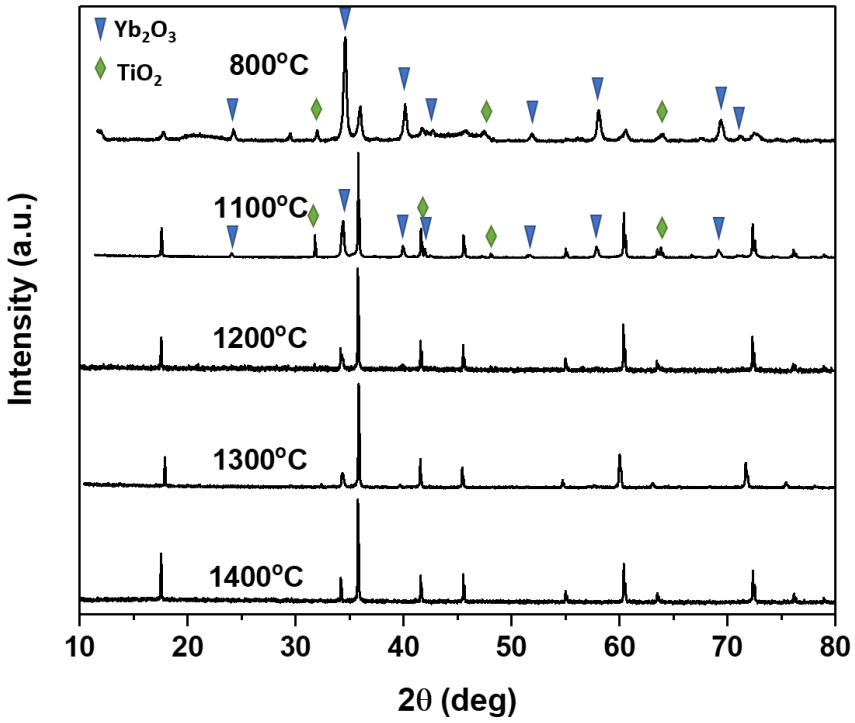

Figure 5-1 Powder XRD patterns from $Yb_2Ti_2O_7$ materials prepared by the ceramic method and annealed at various temperatures for 6 days.

The synthesis and characterization of $CaZrTi_2O_7$ zirconolite-type materials were presented in **Chapter 3**. These materials were prepared by a coprecipitation and a sol-gel method. Powder XRD showed the formation of the zirconolite phase without impurities at temperatures ranging from 1400 to 900 °C for materials prepared by both methods. A $(Ca_{0.25}Zr_{0.25}Ti_{0.5})O_{1.75}$ defect fluorite-type phase was found to be present in materials prepared at 800 °C. A phase transition from the defect fluorite structure to the zirconolite structure occurs between 700 and 900 °C. There was no change observed in the Zr K-edge XANES spectra from all materials annealed between 1400 and 900 °C, despite small changes in the long-range structure shown by Rietveld refinement of those diffraction patterns. Very small changes were observed in the Zr K-edge XANES spectra from the materials prepared at the previously mentioned temperatures and those annealed at 800 °C. The similarity in the shape of these spectra is due to the presence of the defect fluorite-type phase at this temperature wherein the local coordination environment of Zr is approximately 7-coordinate, the same as in zirconolite. Investigation of the local coordination environment of Zr in zirconolite may be better accomplished by examination of the Zr $L_{2,3}$-edge XANES spectra, since

the energy resolution at the energy of the Zr K-edge is poor (~2.5 eV), so distinguishing differences in similar line shapes at this energy is difficult.[13] Ti K-edge spectra were also collected to investigate any changes in the local structure of Ti in the materials. Narrowing of the main edge feature of the Ti K-edge spectra from the coprecipitation and sol-gel materials annealed at 800 °C was attributed to the presence of Ti in the pyrochlore-type phase. The change in the main edge feature resembles the line shape from 6-coordinate Ti (as in $Gd_2Ti_2O_7$ and $CaTiO_3$). The presence of the defect fluorite-type phase would increase the proportion of 6- or 7-coordinate Ti relative to 5-coordinate, explaining the increased resemblance of the spectrum to spectra from 6-coordinate Ti. Thus, it was concluded that phase-pure zirconolite was prepared by coprecipitation and sol-gel methods at 900 °C with very little change in the structure of the material. XRD patterns from materials prepared by the ceramic method (**Figure 5-2**) and annealed for 6 days shows that the zirconolite phase forms with small amounts of unreacted starting materials at temperatures as low as 1200 °C. The diffraction peaks from the starting materials disappear upon further heating of these materials. Thus, the annealing temperature required to form phase-pure $CaZrTi_2O_7$ can be reduced by 300 °C using either a coprecipitation or sol-gel synthesis method, given the same or shorter reaction times.

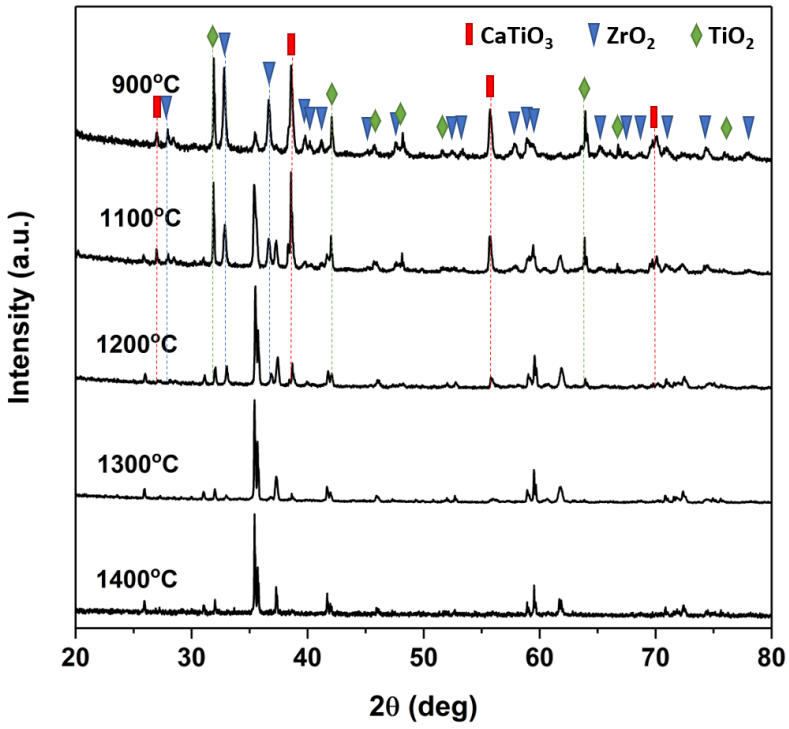

Figure 5-2 Powder XRD patterns from $CaZrTi_2O_7$ materials prepared by the ceramic method and annealed at various temperatures for 6 days. Dotted lines mark major peaks from impurity phases.

The work presented in **Chapters 2** and **3** show that the annealing temperature required to form pyrochlore- and zirconolite-type materials can be lowered by using solution-based synthesis methods such as coprecipitation or sol-gel. This is likely because of atomic-level mixing of reactants, reducing the diffusion distances required to form the materials. **Figure 5-3(a)** shows the XRD patterns from $Gd_2Ti_2O_7$ and $CaZrTi_2O_7$ materials prepared by the ceramic, coprecipitation, and sol-gel methods before annealing. The materials prepared by the solution-based methods (coprecipitation and sol-gel) are X-ray amorphous, while those prepared by the ceramic method show diffraction peaks from the mixed powder reagents. **Figure 5-3(b)** shows the density recovery of ^{244}Cm-doped $Gd_2Ti_2O_7$ and $CaZrTi_2O_7$ materials after a calculated cumulative dose of 20×10^{24} alpha decays/m^3.[41] The two materials were observed to be X-ray amorphous at this dosage. The authors of this study indicated that recrystallization of these materials began at 750 and 600 °C for $Gd_2Ti_2O_7$ and $CaZrTi_2O_7$, respectively. Full recovery of the $Gd_2Ti_2O_7$ material appears to occur at ~800 °C, which agrees with the observations in this thesis that it is possible to form phase-pure $Gd_2Ti_2O_7$ at 800 °C given an X-ray amorphous precursor. The data from the $CaZrTi_2O_7$ material

does not fit as well to the calculated trend lines, so it is not as easy to determine the point at which full recovery of the structure occurs. Another study that was conducted on a sample of X-ray amorphous (estimated dose of $>10^{26}$ alpha decays/m^3) natural zirconolite showed the onset of recrystallization in this sample to occur at 774 °C by differential thermal analysis (DTA).[76] This would agree with the results shown in this thesis that the zirconolite structure forms at 800 °C and not at 700 °C. Based on these studies and the consistency of results from coprecipitation and sol-gel methods, it seems likely that the annealing temperatures determined to be the minimum required to form the pyrochlore- and zirconolite-type materials are the lowest possible.

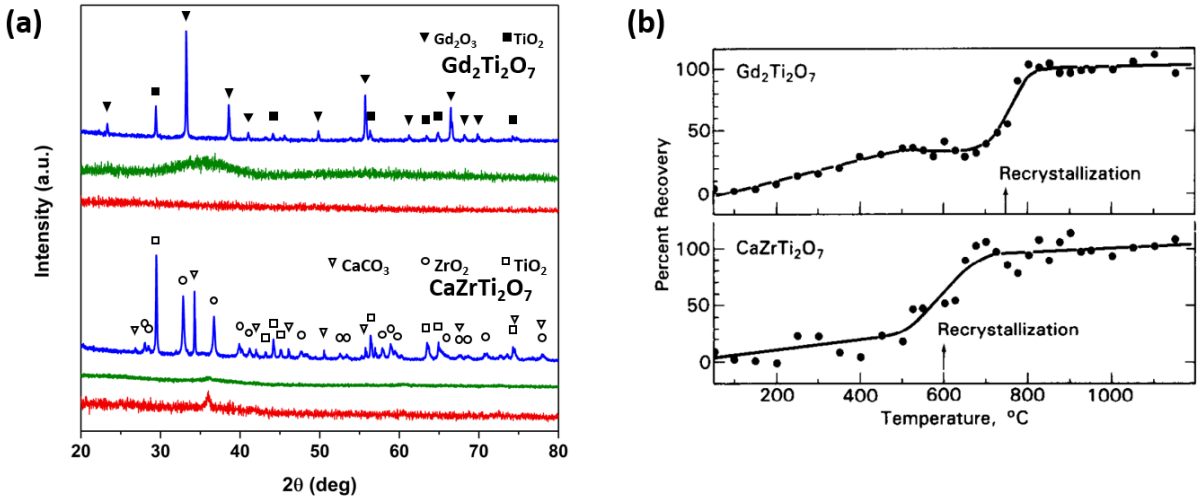

Figure 5-3 (a) XRD patterns from precursor mixtures used to form $Gd_2Ti_2O_7$ and $CaZrTi_2O_7$ materials prepared by the ceramic (blue), coprecipitation (green), and sol-gel (red) methods before annealing. **(b)** Density recovery of ^{244}Cm-doped $Gd_2Ti_2O_7$ and $CaZrTi_2O_7$ after a cumulative dose of $20x10^{24}$ alpha decays/m^3. Reprinted from Journal of Nuclear Materials, 138, Weber, W. J.; Wald, J. W.; Matzke, H. Effects of Self-Radiation Damage in Cm-Doped $Gd_2Ti_2O_7$ and $CaZrTi_2O_7$, 196-209, Copyright (1986), with permission from Elsevier.[41]

While it was shown in **Chapters 2** and **3** that the chemical structure of the pyrochlore- and zirconolite-type materials did not significantly change with annealing temperature, the particle size of the resulting materials was shown to decrease substantially with decreased annealing temperature. The particle size of ceramic materials has been shown to affect the radiation resistance of the material. The work presented in **Chapter 4** investigated the effect of synthesis method on the radiation resistance of the pyrochlore- and zirconolite-type materials prepared by ceramic, coprecipitation, and sol-gel methods. First, $RE_2Ti_2O_7$ (RE = Sm, Gd, Yb) pyrochlore-

type oxides were prepared by a sol-gel method and characterized by XRD and Ti K-edge XANES. These results were nearly identical to those shown in **Chapter 2** for pyrochlore-type materials prepared by the coprecipitation method, most notably that 800 °C was the lowest annealing temperature at which the pyrochlore phase was formed phase-pure. Then, $Gd_2Ti_2O_7$ pyrochlore and $CaZrTi_2O_7$ zirconolite materials were implanted with high energy Au^- ions to simulate radiation damage and Ti K-edge GA-XANES measurements were performed to investigate the resulting structural damage. The zirconolite materials prepared by the coprecipitation and sol-gel methods and annealed at 1200 °C showed identical radiation resistance to the material prepared by the ceramic method and annealed at 1400 °C. The pyrochlore material prepared by the coprecipitation method and annealed at 800 °C showed very similar radiation resistance to the material prepared by the ceramic method and annealed at 1400 °C. However, the pyrochlore material prepared by the sol-gel method and annealed at 800 °C showed much more structural damage than the other materials after implantation. This was attributed to an increased porosity of this material which resulted in densification of the surface material and allowed Au^- ions to penetrate further into the material. It is likely that this material could be prepared by the sol-gel method with lower porosity than the sample studied in future experiments, which could improve the observed radiation resistance of the material, likely to a similar level as seen in the sample prepared by the coprecipitation method.

Given that both solution-based synthesis methods result in the formation of the pyrochlore- or zirconolite-type structures at the same (low) temperatures, it is not obvious which method is superior for preparation of these materials for nuclear wasteform applications. Assuming that the porosity issue can be resolved for the pyrochlore materials prepared by the sol-gel method, neither method shows a clear advantage for radiation resistance. Therefore, the preferred method will depend on the ease of processing and the cost of materials. The pyrochlore coprecipitation synthesis involves the dissolution of rare-earth oxides in hot concentrated nitric acid, followed by increasing the pH by ~ 9 pH units with concentrated ammonium hydroxide. These are very harsh reagents and must be handled very carefully. Additionally, temperature control is very important as adding titanium tert-butoxide to hot nitric acid can result in the evolution of NO_x gas, which can also occur if the base is added too rapidly (due to the heat generated by the neutralization reaction). This synthesis can be altered to avoid these issues by using the water-soluble rare-earth nitrates as

reagents as was used for the sol-gel method. Given this change, most of the safety hazards can be eliminated. The filtration step in this method is likely the most challenging for scaling this process, as it is difficult to fully automate. The sol-gel method is a one-pot method which makes scaling simpler. However, this method is somewhat water-sensitive so there would be additional costs associated with maintaining dry solvents. The sol-gel method is likely the better option for the synthesis of pyrochlore-type oxides as the method would be easier to scale, and the synthesis and drying temperatures are lower than those used in the coprecipitation method. The zirconolite coprecipitation synthesis method has some of the same downsides as the pyrochlore coprecipitation synthesis (e.g. large pH change, difficult to automate), but does offer some benefits over the zirconolite sol-gel synthesis method. The zirconolite sol-gel synthesis method used ethylene glycol as the solvent rather than water, which is more expensive, and the gelation process takes significantly longer than the coprecipitation method (e.g., >1 hour to gel versus < 5 minutes to precipitate). Similar temperatures were used in both methods to dry the precipitate and the gel, but the sol-gel method still has the advantage of being a one-pot method. To determine which synthesis method should be used in industry, optimization of each method and complete cost analyses must be completed which is beyond the scope of this thesis.

5.1 Future Work

The work presented in this thesis focused on the low-temperature synthesis of specific pyrochlore- and zirconolite-type materials for applications as nuclear wasteforms. Similar studies could be conducted for many other ceramic materials which have applications as wasteforms, such as hollandite, brannerite, zircon, garnet, and perovskite. The low-temperature solution-based synthesis methods explored in this thesis could also be applied to glass-ceramic and multiphase ceramic systems where annealing temperature can affect the final composition of the material. This would be particularly useful for systems in which certain phases melt at temperatures below which other phases typically crystallize by ceramic methods. Melting could be avoided in these cases while fully crystallizing the desired products by using a coprecipitation or sol-gel method. These synthesis methods can also be applied to other fields of research, not just nuclear wasteforms. It has been shown that the particle size of ceramic materials could be tuned by adjusting the annealing temperature, which can then affect many material properties.

The synthesis methods described in this thesis require optimization before they can be implemented in industry, particularly the sol-gel methods. Further experiments could investigate the ideal ratio of reactants to solvent and additives (e.g. nitric acid, acetic acid) with the goal of minimizing amounts of reagents and gelation time. Another experiment could investigate how much time is required to completely dry the gels. It is possible that the ion-implanted pyrochlore sample prepared by the sol-gel method may have still contained some amount of ethanol trapped in the material which evaporated upon the final heating, creating a porous surface structure. Hot isostatic pressing (HIP) is commonly used to densify ceramic materials and should be used to determine if it has an effect on the radiation resistance of the $Gd_2Ti_2O_7$ material prepared by the sol-gel method and annealed at 800 °C.[30,59,120] Ion implantation experiments should be conducted on $CaZrTi_2O_7$ materials prepared by the coprecipitation and sol-gel methods and annealed at 900 °C. It is important to conduct this experiment as the bulk properties of the materials prepared by solutions-based synthesis methods and annealed at low temperatures may be different than those of materials prepared by the ceramic method at high temperature, as shown by the $Gd_2Ti_2O_7$ samples. Lastly, further characterization of the $(Ca_{0.25}Zr_{0.25}Ti_{0.5})O_{1.75}$ defect fluorite-type phase should be conducted. Neutron diffraction should be done to evaluate O disorder in the structure and improve the structural characterization of this material. Both Ti and Zr K-edge XANES spectra should be collected from this material and compared to the spectra presented in **Chapter 3**. Collection of Zr $L_{2,3}$-edge XANES spectra may be necessary to more clearly identify changes in the local coordination environment of Zr due to improved energy resolution of these spectra compared to the Zr K-edge XANES spectra. This material may show valuable physical properties, such as ionic conductivity, which should be investigated.

References

(1) Ewing, R. C. THE NUCLEAR FUEL CYCLE versus THE CARBON CYCLE. *Can. Mineral.* **2005**, *43*, 2099–2116.

(2) *The Canadian Nuclear Factbook*; 2017.

(3) *Nuclear Energy Outlook*; 2008.

(4) Ewing, R. C. Long-Term Storage of Spent Nuclear Fuel. *Nat. Mater.* **2015**, *14*, 252–257.

(5) *Inventory of Radioactive Waste in Canada*; 2012.

(6) *National Inventories and Management Strategies for Spent Nuclear Fuel and Radioactive Waste. Methodology for Common Presentation of Data*; 2016.

(7) Ewing, R. C.; Whittleston, R. A.; Yardley, B. W. D. Geological Disposal of Nuclear Waste: A Primer. *Elements* **2016**, *12*, 233–237.

(8) Rahman, R. O. A.; Ibrahium, H. A.; Hung, Y.-T. Liquid Radioactive Wastes Treatment: A Review. *Water* **2011**, *3*, 551–565.

(9) Hedin, A.; Olsson, O. Crystalline Rock as a Repository for Swedish Spent Nuclear Fuel. *Elements* **2016**, *12*, 247–252.

(10) Ramana, M. V. Shifting Strategies and Precarious Progress: Nuclear Waste Management in Canada. *Energy Policy* **2013**, *61*, 196–206.

(11) Ojovan, M. I.; Burakov, B. E.; Lee, W. E. Radiation-Induced Microcrystal Shape Change as a Mechanism of Wasteform Degradation. *J. Nucl. Mater.* **2018**, *501*, 162–171.

(12) Lee, W. E.; Jantzen, C. M.; Ojovan, M. I. Radioactive Waste Conditioning, Immobilisation, and Encapsulation Processes and Technologies: Overview and Advances. In *Radioactive Waste Management and Contaminated Site Clean-up: Processes, Technologies and International Experience*; 2012.

(13) Aluri, E. R.; Grosvenor, A. P. *A Review of X-Ray Absorption Near-Edge Spectroscopic Studies of Pyrochlore-Type Oxides Proposed for Nuclear Materials Applications*; Elsevier Inc., 2016.

(14) Aluri, E. R.; Grosvenor, A. P. A Study of the Electronic Structure and Structural Stability of $Gd_2Ti_2O_7$ Based Glass-Ceramic Composites. *RSC Adv.* **2015**, *5*, 80939–80949.

(15) Ewing, R. C. Ceramic Matrices for Plutonium Disposition. *Prog. Nucl. Energy* **2007**, *49*, 635–643.

(16) Davis, M. J.; Zanotto, E. D. Glass-Ceramics and Realization of the Unobtainable: Property Combinations That Push the Envelope. *MRS Bull.* **2017**, *42*, 195–199.

(17) McCloy, J. S.; Goel, A. Glass-Ceramics for Nuclear-Waste Immobilization. *MRS Bull.* **2017**, *42*, 233–238.

(18) Lee, W. E.; Ojovan, M. I.; Stennett, M. C.; Hyatt, N. C. Immobilisation of Radioactive Waste in Glasses, Glass Composite Materials and Ceramics. *Adv. Appl. Ceram.* **2006**, *105*, 3–12.

(19) Vance, E. R.; Lumpkin, G. R.; Carter, M. L.; Cassidy, D. J.; Ball, C. J.; Day, R. A.; Begg, B. D. Incorporation of Uranium in Zirconolite ($CaZrTi_2O_7$). *J. Am. Ceram. Soc.* **2004**, *85*, 1853–1859.

(20) Ojovan, M. I.; Lee, W. E. Glassy Wasteforms for Nuclear Waste Immobilization. *Metall. Mater. Trans. A Phys. Metall. Mater. Sci.* **2011**, *42*, 837–851.

(21) Tribet, M.; Rolland, S.; Peuget, S.; Broudic, V.; Magnin, M.; Wiss, T.; Jégou, C. Irradiation Impact on the Leaching Behavior of HLW Glasses. *2nd Int. Summer Sch. Nucl. Glas. Wasteform Struct. Prop. Long-Term Behav. SumGLASS 2013* **2014**, *7*, 209–215.

(22) Ewing, R. C.; Weber, W. J.; Lian, J. Nuclear Waste Disposal-Pyrochlore ($A_2B_2O_7$): Nuclear Waste Form for the Immobilization of Plutonium and "Minor" Actinides. *J. Appl. Phys.* **2004**, *95*, 5949–5971.

(23) Stewart, M. W. A.; Vance, E. R.; Moricca, S. A.; Brew, D. R.; Cheung, C.; Eddowes, T.; Bermudez, W. Immobilisation of Higher Activity Wastes from Nuclear Reactor Production of 99Mo. *Sci. Technol. Nucl. Install.* **2013**, *2013*, 1–16.

(24) Yudintsev, S. V; Lizin, A. A.; Livshits, T. S.; Stefanovsky, S. V; Tomilin, S. V; Ewing, R. C. Ion-Beam Irradiation and ^{244}Cm-Doping Investigations of the Radiation Response of Actinide-Bearing Crystalline Waste Forms. *J. Mater. Res.* **2015**, *30*, 1516–1528.

(25) Wang, L.; Liang, T. Ceramics for High Level Radioactive Waste Solidification. *J. Adv. Ceram.* **2012**, *1*, 194–203.

(26) Tumurugoti, P.; Sundaram, S. K.; Misture, S. T.; Marra, J. C.; Amoroso, J. Crystallization Behavior during Melt-Processing of Ceramic Waste Forms. *J. Nucl. Mater.* **2016**, *473*, 178–188.

(27) Ewing, R. C.; Lutze, W. High-Level Nuclear Waste Immobilization with Ceramics. *Ceram. Int.* **1991**, *17*, 287–293.

(28) Weber, W. J.; Navrotsky, A.; Stefanovsky, S.; Vance, E. R.; Vernaz, E. Materials Science of High-Level Nuclear Waste Immobilization. *MRS Bull.* **2009**, *34*, 46–53.

(29) Devanathan, R.; Weber, W. J. Radiation Effects in a Model Ceramic for Nuclear Waste Disposal. *J. Miner. Met. Mater. Soc.* **2007**, *59*, 32–35.

(30) Boccaccini, A. R.; Bernardo, E.; Blain, L.; Boccaccini, D. N. Borosilicate and Lead Silicate Glass Matrix Composites Containing Pyrochlore Phases for Nuclear Waste Encapsulation. *J. Nucl. Mater.* **2004**, *327*, 148–158.

(31) Boccaccini, A. R.; Berthier, T.; Seglem, S. Encapsulated Gadolinium Zirconate Pyrochlore Particles in Soda Borosilicate Glass as Novel Radioactive Waste Form. *Ceram. Int.* **2007**, *33*, 1231–1235.

(32) Paknahad, E.; Grosvenor, A. P. Investigation of the Stability of Glass-Ceramic Composites Containing $CeTi_2O_6$ and $CaZrTi_2O_7$ after Ion Implantation. *Solid State Sci.* **2017**, *74*, 109–117.

(33) Stefanovsky, S. V; Yudintsev, S. V; Livshits, T. S. New Cubic Structure Compounds as Actinide Host Phases. *IOP Conf. Ser. Mater. Sci. Eng.* **2010**, *9*, 1–12.

(34) Yudintsev, S. V.; Stefanovsky, S. V.; Nikonov, B. S.; Nikol'skii, M. S.; Livshits, T. S. Potential Matrices for Immobilization of the Rare Earth-Actinide Fraction of High-Level Waste in the $REE_2Zr_2O_7$-$REE_2Ti_2O_7$ System. *Radiochemistry* **2015**, *57*, 187–199.

(35) Kong, L.; Zhang, Y.; Karatchevtseva, I. Preparation of $Y_2Ti_2O_7$ Pyrochlore Glass-Ceramics as Potential Waste Forms for Actinides: The Effects of Processing Conditions. *J. Nucl. Mater.* **2017**, *494*, 29–36.

(36) Pace, S.; Cannillo, V.; Wu, J.; Boccaccini, D. N.; Seglem, S.; Boccaccini, A. R. Processing Glass-Pyrochlore Composites for Nuclear Waste Encapsulation. *J. Nucl. Mater.* **2005**, *341*, 12–18.

(37) Weber, W. J.; Ewing, R. C.; Catlow, C. R. A.; de la Rubia, T. D.; Hobbs, L. W.; Kinoshita, C.; Matzke, H.; Motta, A. T.; Nastasi, M.; Salje, E. K. H.; et al. Radiation Effects in Crystalline Ceramics for the Immobilization of High-Level Nuclear Waste and Plutonium. *J. Mater. Res.* **1998**, *13*, 1434–1484.

(38) Lumpkin, G. R. Alpha-Decay Damage and Aqueous Durability of Actinide Host Phases in Natural Systems. *J. Nucl. Mater.* **2001**, *289*, 136–166.

(39) Lumpkin, G. R. Ceramic Waste Forms for Actinides. *Elements* **2006**, *2*, 365–372.

(40) Matzke, H. -j; Ray, I. L. F.; Seatonberry, B. W.; Thiele, H.; Trisoglio, C.; Walker, C. T.; White, T. J. Incorporation of Transuranic Elements in Titanate Nuclear Waste Ceramics. *J. Am. Ceram. Soc.* **1990**, *73*, 370–378.

(41) Weber, W. J.; Wald, J. W.; Matzke, H. Effects of Self-Radiation Damage in Cm-Doped $Gd_2Ti_2O_7$ and $CaZrTi_2O_7$. *J. Nucl. Mater.* **1986**, *138*, 196–209.

(42) Crum, J. V; Turo, L.; Riley, B.; Tang, M.; Kossoy, A. Multi-Phase Glass-Ceramics as a Waste Form for Combined Fission Products: Alkalis, Alkaline Earths, Lanthanides, and Transition Metals. *J. Am. Ceram. Soc.* **2012**, *95*, 1297–1303.

(43) Farnan, I.; Cho, H.; Weber, W. J. Quantification of Actinide A-Radiation Damage in Minerals and Ceramics. *Nature* **2007**, *445*, 190–193.

(44) Ewing, C.; Headley, I. Alpha-Recoil Damage in Natural Zirconolite ($CaZrTi_2O_7$). *J. Nucl. Mater.* **1983**, *119*, 102–109.

(45) Potdar, H. S.; Vijayanand, S.; Mohaideen, K. K.; Patil, K. R.; Joy, P. A.; Madhavan, R. R.; Kutty, K. V. G.; Ambashta, R. D.; Wattal, P. K. A Simple Chemical Co-Precipitation/Calcination Route for the Synthesis of Simulated Synroc-B and Synroc-C Powders. *Mater. Chem. Phys.* **2010**, *123*, 695–699.

(46) Kong, L.; Karatchevtseva, I.; Gregg, D. J.; Blackford, M. G.; Holmes, R.; Triani, G. $Gd_2Zr_2O_7$ and $Nd_2Zr_2O_7$ Pyrochlore Prepared by Aqueous Chemical Synthesis. *J. Eur. Ceram. Soc.* **2013**, *33*, 3273–3285.

(47) Digeos, A. A.; Valdez, J. A.; Sickafus, K. E.; Atiq, S.; Grimes, W.; Boccaccini, A. R. Glass Matrix/Pyrochlore Phase Composites for Nuclear Wastes Encapsulation. *J. Mater. Sci.* **2003**, *38*, 1597–1604.

(48) Vance, E. R.; Ball, C. J.; Day, R. A.; Smith, K. L.; Blackford, M. G.; Begg, B. D.; Angel, P. J. Actinide and Rare Earth Incorporation into Zirconolite. *J. Alloys Compd.* **1994**, *213–214*, 406–409.

(49) Cheary, R. W.; Coelho, A. A. A Site Occupancy Analysis of Zirconolite $CaZr_xTi_{3-X}O_7$. *Phys Chem Miner.* **1997**, *24*, 447–454.

(50) Meng, C.; Ding, X.; Li, W.; Zhao, J.; Yang, H. Phase Structure Evolution and Chemical Durability Studies of Ce-Doped Zirconolite – Pyrochlore Synroc for Radioactive Waste Storage. *J. Mater. Sci.* **2016**, *51*, 5207–5215.

(51) Park, S.; Hwang, H. J.; Moon, J. Catalytic Combustion of Methane over Rare Earth Stannate Pyrochlore. *Catal. Letters* **2003**, *87*, 219–223.

(52) James, M.; Carter, M. L.; Zhang, Z.; Zhang, Y.; Wallwork, K. S.; Avdeev, M.; Vancez, E. R. Crystal Chemistry and Structures of (Ca,U) Titanate Pyrochlores. *J. Am. Ceram. Soc.* **2010**, *93*, 3464–3473.

(53) Gregg, D. J.; Zhang, Y.; Zhang, Z.; Karatchevtseva, I.; Blackford, M. G.; Triani, G.; Lumpkin, G. R.; Vance, E. R. Crystal Chemistry and Structures of Uranium-Doped Gadolinium Zirconates. *J. Nucl. Mater.* **2013**, *438*, 144–153.

(54) Kaspar, T. C.; Gigax, J. G.; Shao, L.; Bowden, M. E.; Varga, T.; Shutthanandan, V.; Spurgeon, S. R.; Yan, P.; Wang, C.; Ramuhalli, P.; et al. Damage Evolution of Ion Irradiated Defected-Fluorite $La_2Zr_2O_7$ Epitaxial Thin Films. *Acta Mater.* **2017**, *130*, 111–120.

(55) Shcherbakova, L. G.; Abrantes, J. C. C.; Belov, D. A.; Nesterova, E. A.; Karyagina, O. K.; Shlyakhtina, A. V. Effect of Nb Substitution for Ti on the Electrical Properties of $Yb_2Ti_2O_7$-Based Oxygen Ion Conductors. *Solid State Ionics* **2014**, *261*, 131–140.

(56) Yang, F.; Wang, Y.; Zhao, X.; Xiao, P. Enhanced Ionic Conductivity in Pyrochlore and Fluorite Mixed Phase Yttrium-Doped Lanthanum Zirconate. *J. Power Sources* **2015**, *273*, 290–297.

(57) Bongers, P. F.; Van Meurs, E. R. Ferromagnetism in Compounds with Pyrochlore Structure. *J. Appl. Phys.* **1967**, *38*, 944–945.

(58) Lumpkin, G. R.; Smith, K. L.; Blackford, M. G. Heavy Ion Irradiation Studies of Columbite, Brannerite, and Pyrochlore Structure Types. *J. Nucl. Mater.* **2001**, *289*, 177–187.

(59) Brykała, U.; Diduszko, R.; Jach, K.; Jagielski, J. Hot Pressing of Gadolinium Zirconate Pyrochlore. *Ceram. Int.* **2015**, *41*, 2015–2021.

(60) Aluri, E. R.; Hayes, J. R.; Walker, J. D. S.; Grosvenor, A. P. Investigation of the Structural Stability of Ion-Implanted $Gd_2Ti_{2-X}Sn_xO_7$ Pyrochlore-Type Oxides by Glancing Angle X-Ray Absorption Spectroscopy. *J. Phys. Chem. C* **2014**, *118*, 7910–7922.

(61) Mrázek, J.; Surýnek, M.; Bakardjieva, S.; Buršík, J.; Proboštová, J.; Kašík, I. Luminescence Properties of Nanocrystalline Europium Titanate $Eu_2Ti_2O_7$. *J. Alloys Compd.* **2015**, *645*, 57–63.

(62) Nachimuthu, P.; Thevuthasan, S.; Shutthanandan, V.; Adams, E. M.; Weber, W. J.; Begg, B. D.; Shuh, D. K.; Lindle, D. W.; Gullikson, E. M.; Perera, R. C. Near-Edge X-Ray Absorption Fine Structure Study of Ion-Beam-Induced Phase Transformation in $Gd_2(Ti_{1-Y}Zr_y)_2O_7$. *J. Appl. Phys.* **2005**, *97*, 1–5.

(63) Subramanian, M. A.; Aravamudan, G.; Subba Rao, G. V. Oxide Pyrochlores - A Review. *Prog. Solid State Chem.* **1983**, *15*, 55–143.

(64) Alemi, A.; Kalan, R. E. Preparation and Characterization of Neodymium Tin Oxide Pyrochlore Nanocrystals by the Hydrothermal Method. *Radiat. Eff. Defects Solids* **2008**, *163*, 229–236.

(65) Shu, X.; Fan, L.; Xie, Y.; Zhu, W.; Pan, S.; Ding, Y.; Chi, F.; Wu, Y.; Lu, X. Alpha-Particle Irradiation Effects on Uranium-Bearing $Gd_2Zr_2O_7$ Ceramics for Nuclear Waste Forms. *J. Eur. Ceram. Soc.* **2017**, *37*, 779–785.

(66) Aluri, E. R.; Grosvenor, A. P. An Investigation of the Electronic Structure and Structural Stability of $RE_2Ti_2O_7$ by Glancing Angle and Total Electron Yield XANES. *J. Alloys Compd.* **2014**, *616*, 516–526.

(67) Zhang, F. X.; Lang, M.; Ewing, R. C. Atomic Disorder in $Gd_2Zr_2O_7$ Pyrochlore. *Appl. Phys. Lett.* **2015**, *106*, 191902.

(68) Walker, J. D. S.; Hayes, J. R.; Gaultois, M. W.; Aluri, E. R.; Grosvenor, A. P. A Case for Oxygen Deficiency in $Gd_2Ti_{2-X}Zr_xO_7$ Pyrochlore-Type Oxides. *J. Alloys Compd.* **2013**, *565*, 44–49.

(69) Nästren, C.; Jardin, R.; Somers, J.; Walter, M.; Brendebach, B. Actinide Incorporation in a Zirconia Based Pyrochlore $(Nd_{1.8}An_{0.2})Zr_2O_{7+x}$ (An=Th, U, Np, Pu, Am). *J. Solid State Chem.* **2009**, *182*, 1–7.

(70) Gregg, D. J.; Zhang, Z.; Thorogood, G. J.; Kennedy, B. J.; Kimpton, J. A.; Griffiths, G. J.; Guagliardo, P. R.; Lumpkin, G. R.; Vance, E. R. Cation Antisite Disorder in Uranium-Doped Gadolinium Zirconate Pyrochlores. *J. Nucl. Mater.* **2014**, *452*, 474–478.

(71) Ewing, R. C.; Meldrum, A.; Wang, L. M.; Wang, S. Radiation-Induced Amorphization. In *Reviews in Mineralogy and Geochemistry*; 2000; Vol. 39, pp 319–361.

(72) Shu, X.; Lu, X.; Fan, L.; Yang, R.; Ding, Y.; Pan, S.; Zhou, P.; Wu, Y. Design and Fabrication of $Gd_2Zr_2O_7$-Based Waste Forms for U_3O_8 Immobilization in High Capacity. *J. Mater. Sci.* **2016**, *51*, 5281–5289.

(73) Fan, L.; Shu, X.; Ding, Y.; Duan, T.; Song, M.; Lu, X. Fabrication and Phase Transition of $Gd_2Zr_2O_7$ Ceramics Immobilized Various Simulated Radionuclides. *J. Nucl. Mater.* **2015**, *456*, 467–470.

(74) Kutty, K. V. G.; Asuvathraman, R.; Madhavan, R. R.; Jena, H. Actinide Immobilization in Crystalline Matrix: A Study of Uranium Incorporation in Gadolinium Zirconate. *J. Phys. Chem. Solids* **2005**, *66*, 596–601.

(75) Roberts, B. S. K.; Bourcier, W. L.; Shaw, H. F. Aqueous Dissolution Kinetics of Pyrochlore, Zirconolite and Brannerite at 25, 50, and 75 C. *Radiochim. Acta* **2000**, *88*, 539–543.

(76) Lumpkin, G. R.; Ewing, R. C.; Chakoumakos, B. C.; Greegor, R. B.; Lytle, F. W.; Foltyn, E. M.; Clinard, F. W.; Boatner, L. A.; Abraham, M. M. Alpha-Recoil Damage in Zirconolite ($CaZrTi_2O_7$). *J. Mater. Res. Technol.* **1986**, *1*, 564–576.

(77) Kong, L.; Karatchevtseva, I.; Zhang, Y. A New Method for Production of Glass-$Ln_2Ti_2O_7$ Pyrochlore (Ln = Gd, Tb, Er, Yb). *J. Eur. Ceram. Soc.* **2017**, *37*, 4963–4972.

(78) Hayward, P. J.; Vance, E. R.; Cann, C. D.; Doern, D. C. Crystallization of Titanosilicate Glasses for Nuclear Waste Immobilization. *J. Am. Ceram. Soc.* **1989**, *72*, 579–586.

(79) Niederberger, M.; Pinna, N. Aqueous and Nonaqueous Sol-Gel Chemistry. In *Metal Oxide Nanoparticles in Organic Solvents*; Springer, London, 2009; pp 7–19.

(80) Kong, L.; Karatchevtseva, I.; Blackford, M. G.; Scales, N.; Triani, G. Aqueous Chemical Synthesis of $Ln_2Sn_2O_7$ Pyrochlore-Structured Ceramics. *J. Am. Ceram. Soc.* **2013**, *96*, 2994–3000.

(81) Nair, J.; Nair, P.; Doesburg, E. B. M.; Van Ommen, J. G.; Ross, J. R. H.; Burggraaf, A. J.; Mizukami, F. Preparation and Characterization of Lanthanum Zirconate. *J. Mater. Sci.* **1998**, *33*, 4517–4523.

(82) West, A. R. *Solid State Chemistry and Its Applications*, 2nd ed.; Wiley, 2014.

(83) Kalinkin, A. M.; Usoltsev, A. V.; Kalinkina, E. V.; Zvereva, I. A.; Chislov, M. V.; Nevedomskii, V. N. Effect of Mechanical Activation of Coprecipitated Precursor on Synthesis of $La_2Zr_2O_7$. *Ceram. Int.* **2016**, *42*, 15843–15848.

(84) Li, K.; Wang, H.; Yan, H. Hydrothermal Preparation and Photocatalytic Properties of $Y_2Sn_2O_7$ nanocrystals. *J. Mol. Catal. A Chem.* **2006**, *249*, 65–70.

(85) Danks, A. E.; Hall, S. R.; Schnepp, Z. The Evolution of 'Sol–gel' Chemistry as a Technique for Materials Synthesis. *Mater. Horiz.* **2016**, *3*, 91–112.

(86) Chen, D.; Xu, R. Hydrothermal Synthesis and Characterization of $La_2M_2O_7$ (M = Ti, Zr) Powders. *Mater. Res. Bull.* **1998**, *33*, 409–417.

(87) Moghadam, M. B.; Zebarjad, S. M.; Emampour, J. S.; Youssefi, A. A Study on the Role of Ethylene Glycol/Alcohol Ratio on Synthesis of Nano-Size SnO_2. *Part. Sci. Technol.* **2013**, *31*, 66–70.

(88) Koteswara Rao, K.; Banu, T.; Vithal, M.; Swamy, G. Y. S. K.; Ravi Kumar, K. Preparation and Characterization of Bulk and Nano Particles of $La_2Zr_2O_7$ and $Nd_2Zr_2O_7$ by Sol-Gel Method. *Mater. Lett.* **2002**, *54*, 205–210.

(89) Livage, J.; Condensed, H.; As, H.; As, N. Sol-Gel Chemistry. *Non-crystalline solids* **1992**, *145*, 11–19.

(90) Pecharsky, V. K.; Zavalij, P. Y. *Fundamentals of Powder Diffraction and Structural Characterization of Materials*, 1st ed.; Kluwer Academic Publishers: Norwell, Massachusetts, 2003.

(91) Lavina, B.; Dera, P.; Downs, R. T. Modern X-Ray Diffraction Methods in Mineralogy and Geosciences. *Rev. Mineral. Geochemistry* **2014**, *78*, 1–31.

(92) Toby, B. H. R Factors in Rietveld Analysis: How Good Is Good Enough? *Powder Diffr.* **2006**, *21*, 67–70.

(93) Mccusker, L. B.; Dreele, R. B. Von; Cox, D. E.; Loue È R D, D.; Scardi, P. Rietveld Refnement Guidelines. *Int. Union Crystallogr. J. Appl. Crystallogr. J. Appl. Cryst* **1999**, *32*, 36–50.

(94) Patterson, A. L. The Scherrer Formula for X-Ray Particle Size Determination. *Phys. Rev.* **1939**, *56*, 978–982.

(95) Muniz, F. T. L.; Miranda, M. A. R.; Morilla Dos Santos, C.; Sasaki, J. M. The Scherrer Equation and the Dynamical Theory of X-Ray Diffraction. *Acta Crystallogr. Sect. A Found. Adv.* **2016**, *72*, 385–390.

(96) Miranda, M. A. R.; Sasaki, J. M. The Limit of Application of the Scherrer Equation. *Acta Crystallogr. Sect. A Found. Adv.* **2018**, *74*, 54–65.

(97) Newville, M. Fundamentals of XAFS. *Rev. Mineral. Geochemistry* **2014**, *78*, 33–74.

(98) Greaves, G. N.; Barrett, N. T.; Antonini, G. M.; Thornley, F. R.; Willis, B. T.; Steel, A. Glancing Angle X-Ray Absorption Spectroscopy of Corroded Borosilicate Glass Surfaces Containg Uranium. *J. Am. Chem. Soc.* **1989**, *111*, 4313–4324.

(99) Reid, D. P.; Stennett, M. C.; Ravel, B.; Woicik, J. C.; Peng, N.; Maddrell, E. R.; Hyatt, N. C. The Structure of Ion Beam Amorphised Zirconolite Studied by Grazing Angle X-Ray Absorption Spectroscopy. *Nucl. Instruments Methods Phys. Res. Sect. B Beam Interact. with Mater. Atoms* **2010**, *268*, 1847–1852.

(100) Henderson, G. S.; de Groot, F. M. F.; Moulton, B. J. A. X-Ray Absorption Near-Edge Structure (XANES) Spectroscopy. *Rev. Mineral. Geochemistry* **2014**, *78*, 75–138.

(101) Maginn, S. J. Analytical Applications of Synchrotron Radiation. *Analyst* **1998**, *123*, 19R–29R.

(102) Farges, F.; Brown, G. E.; Rehr, J. J. Coordination Chemistry of Ti(IV) in Silicate Glasses and Melts: I. XAFS Study of Titanium Coordination in Oxide Model Compounds. *Geochim. Cosmochim. Acta* **1996**, *60*, 3023–3038.

(103) Farges, F. Coordination of Ti in Crystalline and Glassy Fresnoites: A High-Resolution XANES Spectroscopy Study at the Ti K-Edge. *J. Non. Cryst. Solids* **1996**, *204*, 53–64.

(104) Cabaret, D.; Bordage, A.; Juhin, A.; Arfaoui, M.; Gaudry, E. First-Principles Calculations of X-Ray Absorption Spectra at the K-Edge of 3d Transition Metals: An Electronic Structure Analysis of the Pre-Edge. *Phys. Chem. Chem. Phys.* **2010**, *12*, 5619–5633.

(105) Farges, F. Fivefold-Coordinated Ti^{4+} in Metamict Zirconolite and Titanite: A New Occurrence Shown by Ti K-Edge XANES Spectroscopy. *Am. Mineral.* **1997**, *82*, 44–50.

(106) Jiang, N.; Su, D.; Spence, J. C. H. Determination of Ti Coordination from Pre-Edge Peaks in Ti K-Edge XANES. *Phys. Rev. B - Condens. Matter Mater. Phys.* **2007**, *76*, 1–9.

(107) De Groot, F. High-Resolution X-Ray Emission and X-Ray Absorption Spectroscopy. *Chem. Rev.* **2001**, *101*, 1779–1808.

(108) Yamamoto, T. Assignment of Pre-Edge Peaks in K-Edge X-Ray Absorption Spectra of 3d Transition Metal Compounds: Electric Dipole or Quadrupole? *X-Ray Spectrom.* **2008**, *37*, 572–584.

(109) Sham, T. K.; Rivers, M. L. A Brief Overview of Synchrotron Radiation. *Rev. Mineral. Geochemistry* **2002**, *49*, 117–147.

(110) de Groot, F. M. F. X-Ray Absorption and Dischroism of Transition Metals and Their Componuds. *J. Electron Spectros. Relat. Phenomena* **1994**, *67*, 529–622.

(111) Lian, J.; Wang, L. M.; Ewing, R. C.; Boatner, L. A. Ion Beam Implantation and Cross-Sectional TEM Studies of Lanthanide Titanate Pyrochlore Single Crystals. *Nucl. Instruments Methods Phys. Res. Sect. B Beam Interact. with Mater. Atoms* **2005**, *241*, 365–371.

(112) Weber, W. J. Radiation and Thermal Ageing of Nuclear Waste Glass. *Procedia Mater. Sci.* **2014**, *7*, 237–246.

(113) Lang, M.; Tracy, C. L.; Palomares, R. I.; Zhang, F.; Severin, D.; Bender, M.; Trautmann, C.; Park, C.; Prakapenka, V. B.; Skuratov, V. A.; et al. Characterization of Ion-Induced Radiation Effects in Nuclear Materials Using Synchrotron X-Ray Techniques. *J. Mater. Res.* **2015**, *30*, 1366–1379.

(114) Kurpaska, L.; Jagielski, J. Mechanical Properties of Irradiated $Gd_2Zr_2O_7$ Pyrochlores as Studied by Nanoindentation Technique - Effect of Grains and Grain Boundaries. *Nucl. Instruments Methods Phys. Res. Sect. B Beam Interact. with Mater. Atoms* **2016**, *379*, 107–111.

(115) Grover, V.; Shukla, R.; Kumari, R.; Mandal, B. P.; Kulriya, P. K.; Srivastava, S. K. Effect of Grain Size and Microstructure on Radiation Stability of CeO_2: An Extensive Study. *Phys. Chem. Chem. Phys.* **2014**, *16*, 27065–27073.

(116) Tandetron Accelerator Laboratory http://www.isw.physics.uwo.ca/facilities_techniques/index.html (accessed Jul 10, 2018).

(117) Ziegler, J. F.; Biersack, J. P.; Ziegler, M. D. SRIM (The Stopping and Rang of Ions in Solids). 2013.

(118) Waychunas, G. A. Grazing-Incidence X-Ray Absorption and Emission Spectroscopy. *Rev. Mineral. Geochemistry* **2002**, *49*, 267–315.

(119) Sellin, P.; Leupin, O. X. The Use of Clay as an Engineered Barrier in Radioactive-Waste Management - A Review. *Clays Clay Miner.* **2014**, *61*, 477–498.

(120) Kumar, R.; Singh, K.; Chakravarty, D.; Chowdhury, A. Attaining Near-Theoretical Densification in Nanograined Pyrochlore $La_2Zr_2O_7$ (LZ) Ceramic at 1150 °C by Spark Plasma Sintering. *Scr. Mater.* **2016**, *117*, 37–40.

(121) Bernard, D.; Pannetier, J.; Lucas, J. Ferroelectric and Antiferroelectric Materials with Pyrochlore Structure. *Ferroelectrics* **1978**, *21*, 429–431.

(122) Nguyen, S. T.; Nakayama, T.; Suematsu, H.; Suzuki, T.; Takeda, M.; Niihara, K. Low Thermal Conductivity $Y_2Ti_2O_7$ as a Candidate Material for Thermal/Environmental Barrier Coatings. *Ceram. Int.* **2016**, *42*, 11314–11323.

(123) Nachimuthu, P.; Thevuthasan, S.; Adams, E. M.; Weber, W. J.; Begg, B. D.; Mun, B. S.; Shuh, D. K.; Lindle, D. W.; Gullikson, E. M.; Perera, R. C. C. Near-Edge X-Ray Absorption Fine Structure Study of Disordering in $Gd_2(Ti_{1-Y}Zr_y)_2O_7$ Pyrochlores. *J. Phys. Chem. B* **2005**, *109*, 1337–1339.

(124) Tong, Y.; Xue, P.; Jian, F.; Lu, L.; Wang, X.; Yang, X. Preparation and Characterization of $Y_2Zr_2O_7$ Nanocrystals and Their Photocatalytic Properties. *Mater. Sci. Eng. B Solid-State Mater. Adv. Technol.* **2008**, *150*, 194–198.

(125) Gupta, S. K.; Reghukumar, C.; Keskar, M.; Kadam, R. M. Revealing the Oxidation Number and Local Coordination of Uranium in $Nd_2Zr_2O_7$pyrochlore: A Photoluminescence Study. *J. Lumin.* **2016**, *177*, 166–171.

(126) Zhang, F. X.; Lang, M.; Tracy, C.; Ewing, R. C.; Gregg, D. J.; Lumpkin, G. R. Incorporation of Uranium in Pyrochlore Oxides and Pressure-Induced Phase Transitions. *J. Solid State Chem.* **2014**, *219*, 49–54.

(127) Gregg, D. J.; Zhang, Y.; Middleburgh, S. C.; Conradson, S. D.; Triani, G.; Lumpkin, G. R.; Vance, E. R. The Incorporation of Plutonium in Lanthanum Zirconate Pyrochlore. *J. Nucl. Mater.* **2013**, *443*, 444–451.

(128) Cleave, A.; Grimes, R. W.; Sickafus, K. Plutonium and Uranium Accommodation in Pyrochlore Oxides. *Philos. Mag.* **2005**, *85*, 967–980.

(129) Fortner, J. A.; Kropf, A. J.; Finch, R. J.; Bakel, A. J.; Hash, M. C.; Chamberlain, D. B. Crystal Chemistry of Uranium (V) and Plutonium (IV) in a Titanate Ceramic for Disposition of Surplus Fissile Material. *J. Nucl. Mater.* **2002**, *304*, 56–62.

(130) Chen, H.; Gao, Y.; Liu, Y.; Luo, H. Coprecipitation Synthesis and Thermal Conductivity of $La_2Zr_2O_7$. *J. Alloys Compd.* **2009**, *480*, 843–848.

(131) Heald, S. M.; Brewe, D. L.; Stern, E. A.; Kim, K. H.; Brown, F. C.; Jiang, D. T.; Crozier, E. D.; Gordon, R. A. XAFS and Micro-XAFS at the PNC-CAT Beamlines. *J. Synchrotron Radiat.* **1999**, *6*, 347–349.

(132) Ravel, B.; Newville, M. Athena, Artemis, Hephaestus: Data Analysis for X-Ray Absorption Spectroscopy Using IFEFFIT. *J. Synchrotron Radiat.* **2005**, *12*, 537–541.

(133) Farges, F.; Brown, G.; Rehr, J. Ti K-Edge XANES Studies of Ti Coordination and Disorder in Oxide Compounds: Comparison between Theory and Experiment. *Phys. Rev. B* **1997**, *56*, 1809–1819.

(134) Rossell, H. J. Solid Solution of Metal Oxides in the Zirconolite Phase $CaZrTi_2O_7$. II. The Ternary Phase $CaZr_xTi_{3-X}O_7$. *J. Solid State Chem.* **1992**, *99*, 52–57.

(135) Greegor, R. B.; Blohowiak, K. Y.; Osborne, J. H.; Krienke, K. A.; Cherian, J. T.; Lytle, F. W. X-Ray Spectroscopic Investigation of the Zr-Site in Thin Film Sol-Gel Surface Preparations. *J. Sol-Gel Sci. Technol.* **2001**, *20*, 35–50.

(136) Anderson, H. H. The Depth Resolution of Sputter Profiling. *Appl. Phys.* **1979**, *18*, 131–140.

(137) X-ray Attenuation Length http://henke.lbl.gov/optical_constants/atten2.html (accessed Mar 26, 2018).

(138) Zhang, J.; Lian, J.; Fuentes, A. F.; Zhang, F.; Lang, M.; Lu, F.; Rodney, C. Enhanced Radiation Resistance of Nanocrystalline Pyrochlore $Gd_2(Ti_{0.65}Zr_{0.35})_2O_7$. *Appl. Phys. Lett.* **2009**, *94*, 243110.

(139) El-Atwani, O.; Hinks, J. A.; Greaves, G.; Allain, J. P.; Maloy, S. A. Grain Size Threshold for Enhanced Irradiation Resistance in Nanocrystalline and Ultrafine Tungsten. *Mater. Reseach Lett.* **2017**, *5*, 343–349.

(140) Lou, Y.; Dourdain, S.; Rey, C.; Serruys, Y.; Simeone, D.; Mollard, N.; Deschanels, X. Structure Evolution of Mesoporous Silica under Heavy Ion Irradiations of Intermediate Energies. *Microporous Mesoporous Mater.* **2017**, *251*, 146–154.

(141) Horng, R.; Wuu, D.; Kung, C.; Lin, C.; Leu, C.; Haung, T.; Sze, S. Ion-Implantation Treatment (Ba,Sr)TiO_3 Thin Films. *Jpn. J. Appl. Phys.* **2000**, *39*, 6614–6618.

(142) Lopatin, C. M.; Alford, T. L.; Pizziconi, V. B.; Kuan, M.; T, L. Ion-Beam Densification of Hydroxyapatite Thin Films. *Nucl. Instruments Methods Phys. Res.* **1998**, *145*, 522–531.

(143) Gregg, D. J.; Karatchevtseva, I.; Thorogood, G. J.; Davis, J.; Bell, B. D. C.; Jackson, M.; Dayal, P.; Ionescu, M.; Triani, G.; Short, K.; et al. Ion Beam Irradiation Effects in Strontium Zirconium Phosphate with NZP-Structure Type. *J. Nucl. Mater.* **2014**, *446*, 224–231.

Appendix

Supporting Tables and Figures for Chapter 2

Table A1 Rietveld refinement results for $Sm_2Ti_2O_7$ and $Yb_2Ti_2O_7$ materials prepared by the coprecipitation method and annealed at 1400 and 800 °C.

	$Sm_2Ti_2O_7$		$Yb_2Ti_2O_7$	
Annealing Temperature	**1400°C**	**800°C**	**1400°C**	**800°C**
Lattice constant, a (Å)	10.2158(1)	10.2229(2)	10.03024(8)	10.0305(2)
O 48f(x) positional parameter, x	0.427(1)	0.430(7)	0.430(1)	0.4236(6)
B_{OVL}	0.5	0.5	0.5	0.5
R_{exp}	5.07947	3.39600	3.3353	2.80318
R_p	9.12258	4.47303	5.46347	3.35093
R_{wp}	11.77853	6.19494	6.65488	4.26318
χ^2	5.37708	3.32765	3.98116	2.31294

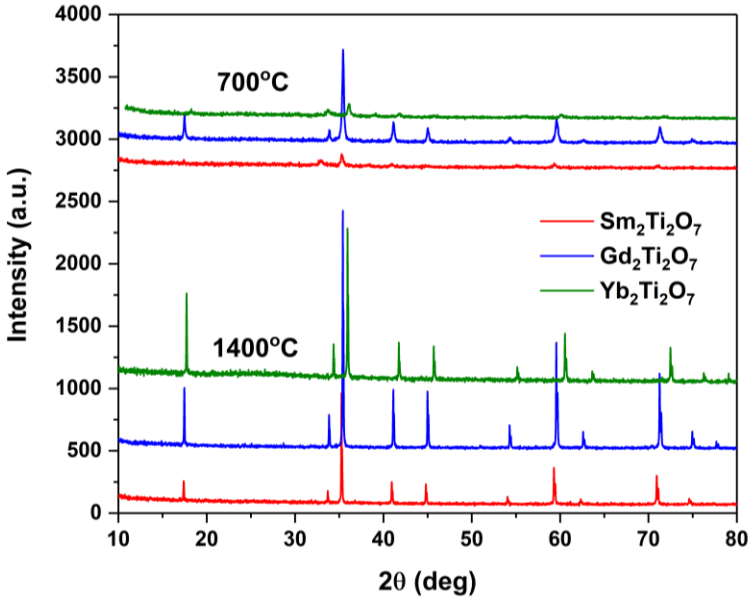

Figure A1 Unscaled diffraction patterns from $RE_2Ti_2O_7$ (RE = Sm, Gd, Yb) materials prepared by the coprecipitation method and annealed at 700 and 1400 °C.

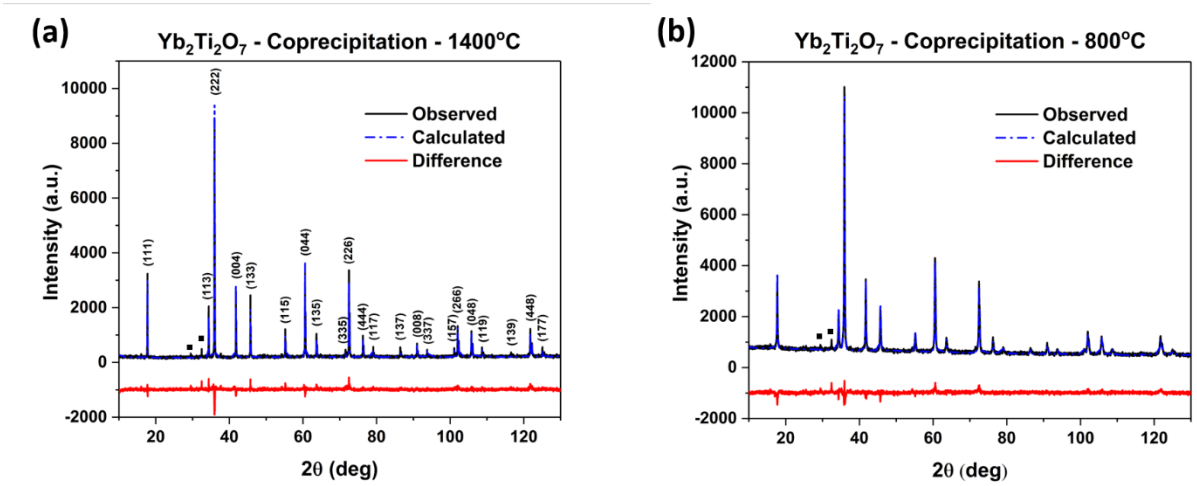

Figure A2 Rietveld refined powder XRD patterns from $Yb_2Ti_2O_7$ prepared by the coprecipitation method and annealed at **(a)** 1400 °C and **(b)** 800 °C. Squares mark impurity peaks which were not included in the refinements.

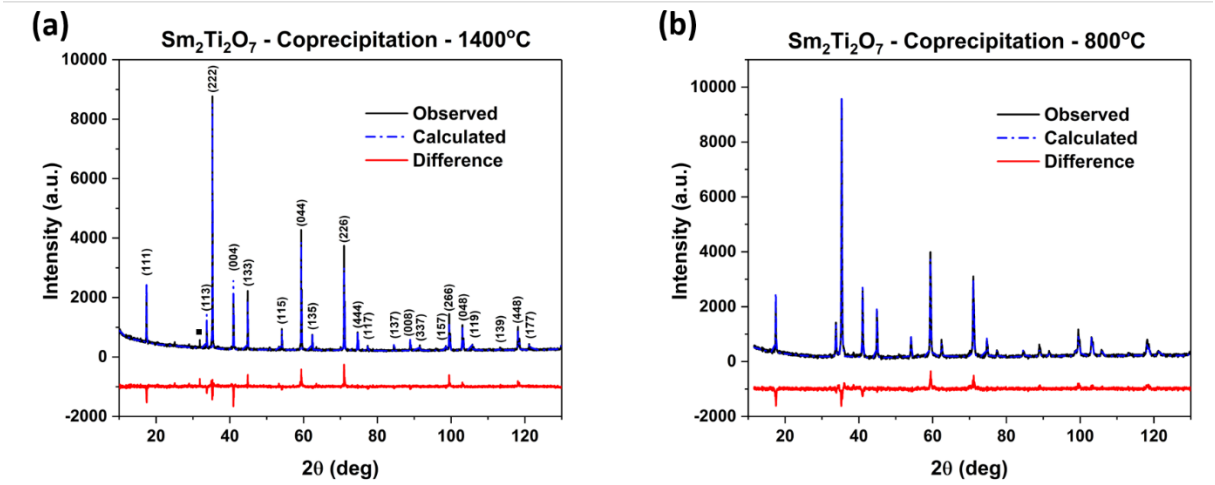

Figure A3 Rietveld refined powder XRD patterns from $Sm_2Ti_2O_7$ prepared by the coprecipitation method and annealed at **(a)** 1400 °C and **(b)** 800 °C. Squares mark impurity peaks which were not included in the refinements.